Saturation of Internal Tide Generation and Wake Vortex Energy Partitioning in Shallow Fjord-like Topography

by

Jia-Xuan Chang
B.Sc., National Taiwan University, 2014
M.Sc., Institute of Oceanography, National Taiwan University, 2017

A Dissertation Submitted in Partial Fulfillment of the
Requirements for the Degree of

DOCTOR OF PHILOSOPHY

in the School of Earth and Ocean Sciences

University of Victoria

We acknowledge and respect the Lək̓ʷəŋən (Songhees and Xʷsepsəm/Esquimalt) Peoples on whose territory the university stands, and the Lək̓ʷəŋən and W̱SÁNEĆ Peoples whose historical relationships with the land continue to this day.

Saturation of Internal Tide Generation and Wake Vortex Energy Partitioning in Shallow Fjord-like Topography

by

Jia-Xuan Chang
B.Sc., National Taiwan University, 2014
M.Sc., Institute of Oceanography, National Taiwan University, 2017

Supervisory Committee

Dr. Jody M. Klymak, Supervisor
(School of Earth and Ocean Sciences)

Dr. Guoqi Han, Adjunct Departmental Member
(School of Earth and Ocean Sciences)

Dr. Ann E. Gargett, Affiliate Departmental Member
(School of Earth and Ocean Sciences)

Dr. Peter Oshkai, Outside Member
(Department of Mechanical Engineering)

ABSTRACT

Internal tides and wake vortices are key processes driving energy dissipation and mixing in coastal environments. While internal tide generation over supercritical slopes has been extensively studied in deep ocean settings, much less is known about its behavior in shallow coastal systems, where barotropic tidal forcing is strong, and non-linear effects dominate. This dissertation investigates the tidal energy pathways and dissipation associated with internal tides and wake vortices in such environments, using numerical simulations to explore isolated and complex three-dimensional topographies.

A novel phenomenon of energy saturation in internal tide generation is identified, where the energy converted from barotropic tides ceases to scale quadratically with tidal velocity under highly non-linear conditions. This study characterizes the qualitative flow features associated with saturation, revealing that the flow resembles approach-controlled flow. Saturation is found to occur when the mean speed at the crest equals the mode-1 phase speed ($Fr_c = U_c/c_1 = 1$). Moreover, the results challenge the conventional understanding that internal tides are not generated when $Fr_c > 1$; instead, they are generated but reach a saturation state.

In complex topographies featuring headlands, the energy partitioning between internal tides and wake vortices is analyzed. We identify additional energy losses fed to vortices, providing a systematic framework to estimate these losses using the bluff body law. Our results highlight that ridge-constricted flow and the cross-sectional area between the ridge crest and the top of headland yield reliable estimates. While wake vortices consume most of the energy that was fed into locally, their presence does not influence the dissipation or outward propagation of internal tide energy. The dissipation and propagation pathways of both processes are quantified, offering insights into their independent roles in coastal energy budgets.

These findings challenge theoretical scaling law and highlight the distinct dynamics of tidal energy in shallow coastal systems. By improving our understanding of tidal energy distribution and dissipation, this research contributes to refining parameterizations in ocean models and advancing knowledge of coastal mixing processes.

Contents

List of Tables

List of Figures

ACKNOWLEDGEMENTS

I would like to thank my supervisor, Dr. Jody Klymak. When I first arrived in Victoria, struggling with English, we quickly established a project direction that allowed me to pursue the modeling work I was passionate about. Thank you for trusting me with such a challenging and rewarding project. Although you often reminded me how tough this field is, I truly enjoyed the growth it brought. Our weekly meetings, especially during my candidacy preparation, helped me understand internal tides and lee waves more deeply. I appreciated the flexibility to work from Taiwan during the pandemic, and later, our continued collaboration during your sabbatical in France. Your consistent feedback during manuscript writing taught me how to organize scientific thoughts and clearly convey ideas, which guided me through both papers.

I'm very grateful to Dr. Ann Gargett for serving on my committee and for your mentorship during group meetings. Your insightful questions, practical advice, prompt feedback, and constant encouragement played a vital role in my PhD.

Thank you to Dr. Peter Oshkai for your clear explanations of numerical modeling concepts, which helped me build a stronger foundation in this area.

To Dr. Guoqi Han, thank you for bringing your expertise in global models and satellite altimetry to support my work. And to Dr. David Farmer, who served on my committee in the early years—thank you for your early guidance and for helping me understand the background of Knight Inlet and hydraulic control.

To our group members—Johannes Gemmrich, Kurtis, Carmen, Leah, Becky, Jamie, and Lauryn—thank you for the conversations, support, and shared learning over the years.

Thanks also to the broader SEOS community—Liang, Siyu, Jo, Ameneh, Simin, Raj, Kevwe, Camille, Ruth, Grace, Patrick, Max, Joey, Liz, Laura, Brandon, Julia, and Rebecca—who made this journey more meaningful.

Special thanks to Ara and Anne—our peer mentoring group helped me through some of the hardest times. I truly don't know if I could have finished without you.

Finally, I thank my family. To my husband, Han—thank you for moving across the world and supporting me through the challenges of this PhD. Your presence made this journey possible. To my parents and sisters—thank you for your constant encouragement and love.

DEDICATION

To Han, and to my parents—
for your unwavering love and support throughout this journey.

And to the late Prof. T.-Y. David Tang,
who first inspired my pursuit of oceanography.

Chapter 1

Introduction

1.1 Ocean mixing in the open ocean and its importance

Ocean mixing is important for local marine ecosystems as it helps move heat, nutrients, and other materials vertically within the water column. This process supports biological productivity by bringing nutrients to surface waters and distributing energy throughout the ocean layers. One of the most significant contributors to ocean mixing is the mixing associated with internal waves. Internal waves are oscillatory motions that occur in stratified fluids, propagating within the interior of the water column. These waves often become unstable and eventually break, generating turbulence and mixing. This topic has received extensive attention in the field, with recent comprehensive reviews highlighting the diverse roles of internal-wave-driven mixing (MacKinnon et al., 2017; Whalen et al., 2020). Figure 1.1 provides a summary of the various processes and contributions of internal-wave-induced mixing in the ocean.

In addition to its local effects, ocean mixing has a major impact on the global scale. It plays a key role in maintaining global ocean circulation, which moves heat and salt around the planet and helps regulate climate (Munk and Wunsch, 1998; Talley, 2013; de Lavergne et al., 2016; Kunze, 2017a). Ocean mixing also helps balance the global ocean energy budget by dissipating tidal energy and redistributing it across the ocean (Wunsch and Ferrari., 2004; Kunze, 2017b). These processes are critical for keeping the ocean in balance and supporting its role in Earth's climate system.

A key driver of internal waves is tides. Internal waves with tidal frequencies, known as internal tides (Garrett and Kunze, 2007), are generated when tidal currents

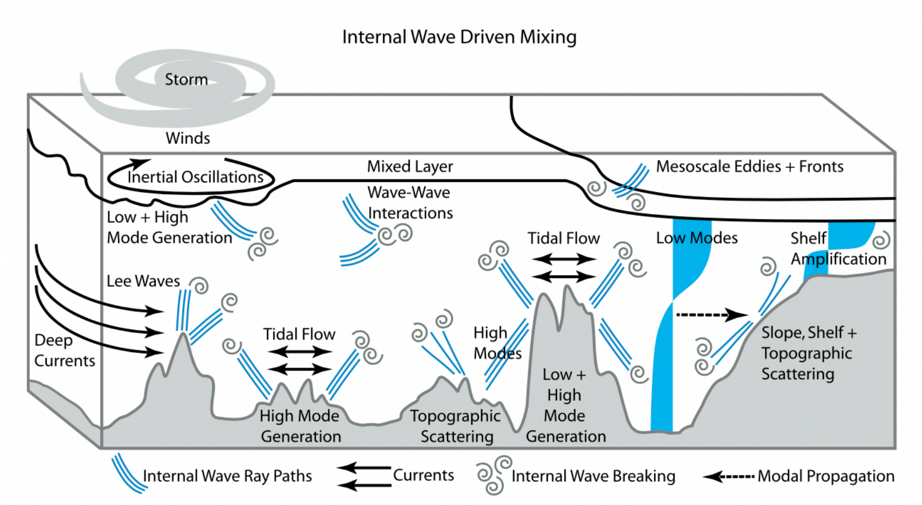

Figure 1.1: Schematic of internal wave mixing processes in the open ocean from MacKinnon et al. (2017)

flow over irregular seafloor features such as mid-ocean ridges and seamounts. These internal tides transport energy across the open ocean and drive mixing far from their generation sites.

1.2 The mixing in Coastal/Fjord environments

While ocean mixing is critical in the open ocean, coastal environments often exhibit greater variability compared to the relatively uniform open ocean. Coastal regions can range from highly stratified to well-mixed areas, influenced by factors such as wind, dynamic freshwater input, and large horizontal gradients in salinity, temperature, or flow. In this study, we focus on the influence of strong tides in shallow water depths and complex topographic features on fundamental dynamics of tide-topography interactions.

Fjords and narrow coastal inlets are typically deep and steep-sided, with tidal currents channeled through constrained passages. These strong flows interact with abrupt topographic changes, generating dynamic mixing phenomena. As tidal currents encounter the three-dimensional irregular topography, internal tides may form vertically, while wake vortices can develop horizontally behind topographic features (Geyer and Signell, 1990; Johnston et al., 2019; Klymak and Gregg, 2001; McCabe et al., 2006; MacCready and Pawlak, 2001; Perfect et al., 2020a,b; Warner et al., 2013). Wake vortices are swirling flows of fluid that form in the lee of topographic features such as headlands, capes, islands, or other bathymetric structures with abrupt lateral changes. In fjord-like environments, internal tides can reach larger amplitudes (Farmer and Armi, 1999b), while wake vortices add complexity by creating horizontal flows behind obstacles. Both motions redistribute energy and momentum horizontally and vertically, and creating localized zones of turbulence. In some cases, local dissipation rates caused by wake vortices have been observed to exceed those generated by internal tides (Inall et al., 2005; Klymak and Gregg, 2004). Together, these two processes play a critical role in balancing the tidal energy budget within fjords.

Understanding the individual roles of internal tides and wake vortices in fjords is therefore essential for deciphering energy pathways and dissipation mechanisms in these environments. The enhanced mixing and dissipation in fjords may have significant implications for nutrient availability, biological productivity, and energy balance.

1.3 Knight Inlet as a Natural Laboratory

Knight Inlet, located on the west coast of Canada, is a long deep fjord extending 125 km into the mainland from the Queen Charlotte Strait (Figure 1.2). It has a roughly uniform width of 2 to 3 km, with vertical sidewalls (Farmer and Smith, 1980b), and an average depth of 295 meters, with a maximum depth of 540 meters (Figure 1.3). The inlet is fed by the Klinaklini River and features two sills: the inner sill rises to a depth of 63 m, 74 km from the head, and the outer sill rises to a depth of 67 m, 110 km from the head. The outer basin, enclosed by the inner and outer sill, has a depth of up to 250 m, while the inner basin is deeper, reaching up to 540 m.

In summer, the density structure in Knight Inlet is typical of many fjords, with a sharp pycnocline (greatest density difference in vertical direction) at around 5 to 10 m in depth along much of its length, separating nearly fresh river water from the stratified and more saline fluid below (Pickard and Rodgers, 1959). In winter, there is no distinct surface layer, with seasonal changes in density influenced by shortwave radiation and seasonal runoff, which reaches a maximum in June due to snowmelt (Pickard and Rodgers, 1959). Additionally, there is a horizontal density gradient because the inner sill blocks salty ocean water from entering the inner basin (Pickard and Rodgers, 1959).

Extensive observational studies of the inner sill have been conducted due to its role in generating internal tides (e.g., Cummins et al. (2003, 2006); Farmer and Smith

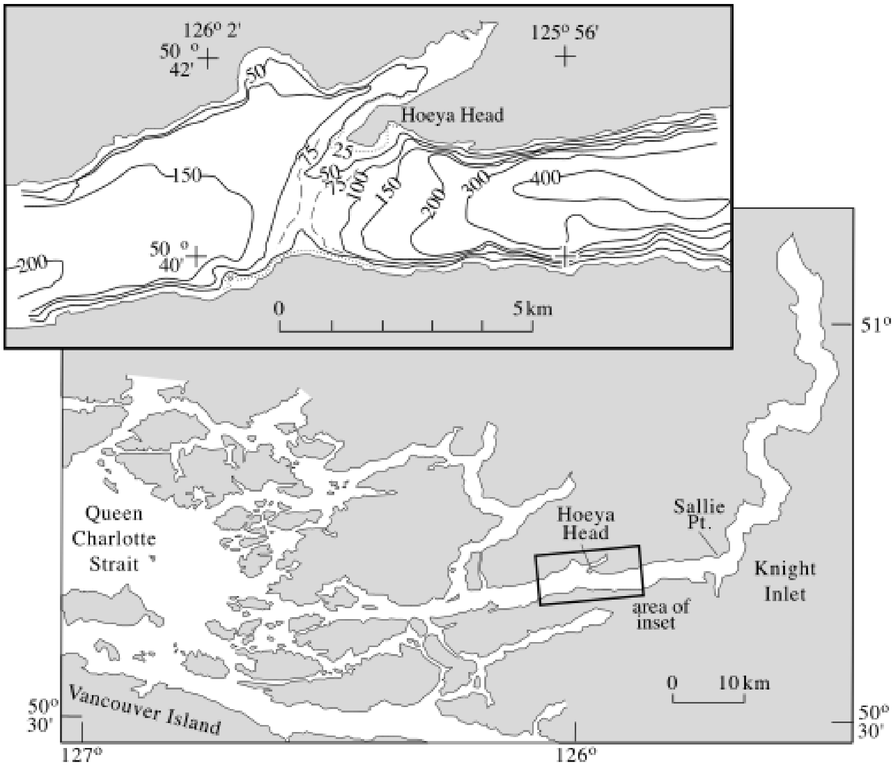

Figure 1.2: Geographic map of Knight Inlet from Farmer and Armi (1999b)

(1980b); Farmer and Armi (1999b,a); Klymak and Gregg (2001)). The mixing caused by internal tides results in high biological productivity and diversity in the area surrounding the sill (Rubidge et al., 2020). Tidal mixing in Knight Inlet maintains circulation, moving freshwater introduced by the Klinaklini River and tidally forced seawater from the ocean.

The inlet's topography includes relatively sharp headlands bracketing the sill. On the south side, Prominent Point narrows the channel by 750 meters, while on the north side, Hoeya Head extends almost as far, marking the boundary of Hoeya Sound. Three-dimensional recirculation resulting from boundary separation in the lee of these headlands creates dipole wake vortices (Figure 1.4, Klymak and Gregg (2001)). The estimated volume-integrated potential vorticity in each eddy is 3400 kg m^{-1} s^{-1}, forming in less than 0.75 hours (Klymak and Gregg, 2001).

Barotropic tides in Knight Inlet are dominated by the semidiurnal M2 tide (12.42 hr). Tidal currents over the inner sill can exceed 0.8 m s^{-1} due to the inlet's geometry and large tidal range (3 to 5 m) (Farmer and Smith, 1980a). Surface tidal energy is lost at the sill, as evidenced by a sharp drop in the tidal phase, while the rest of

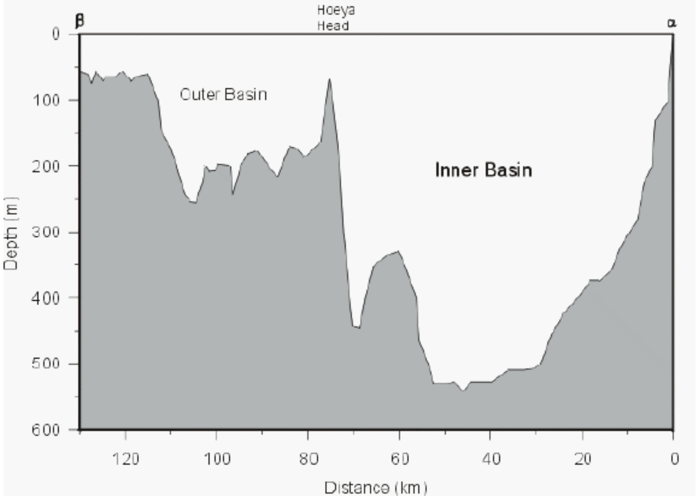

Figure 1.3: Depth profile of Knight Inlet. The shallowest sill serves as the focus of our study and distinctly separates the inner basin from the outer basin.

the inlet remains in phase (Farmer and Armi, 1999b,a; Freeland and Farmer, 1980). Barotropic energy loss has been estimated at $4 - 10$ MW, with larger losses in the summer due to increased stratification (Freeland and Farmer, 1980; Klymak and Gregg, 2004; Stacey, 1985).

The parameter $Nh/U \sim 10$ for Knight Inlet provides insight into the characteristics of the flow. Features observed in Knight Inlet include upstream blocking (Klymak and Gregg, 2003), a hydraulically controlled jet over the crest, and a hydraulic jump in the lee of the sill (Farmer and Armi, 1999b; Klymak and Gregg, 2001, 2003, 2004). Once the flow is hydraulically controlled or alternatively called crest-controlled (Lawrence, 1993), it meets a criticality condition, with the composite Froude number $G^2 = u_1^2/g'h_1 + u_2^2/g'h_2 = 1$ (Armi, 1986).

The hydraulic conditions within Knight Inlet change depending on the season. During winter, when tidal forcing intensifies and stratification weakens, the flow transitions from being crest-controlled to approach-controlled (Lawrence, 1993), resulting in a supercritical region extending from the upstream control section to downstream of the crest sill (Cummins et al., 2006; Cummins and Armi, 2010; Stashchuk and Vlasenko, 2007). The approach-controlled scenario response to strong tidal forcing also been seen in Strait of Gibraltar (Sánchez-Garrido et al., 2011).

In this context, the terms "critical" and "supercritical" refer to the hydraulic state of the flow, based on the composite Froude number condition ($G^2 = 1$). This usage is distinct from the topographic steepness-based definition of criticality, which

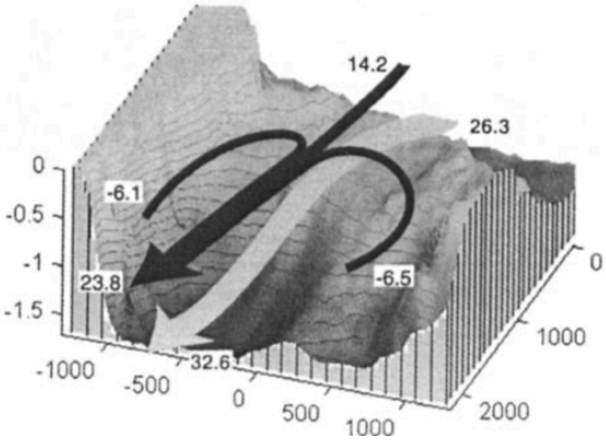

Figure 1.4: Three-dimensional recirculation schematic diagram around sill and headlands (Klymak and Gregg, 2001)

is introduced later in the context of internal tide generation.

Only one-third of the barotropic energy loss is estimated to be dissipated near the sill (Webb and Pond, 1986; Klymak and Gregg, 2004), with the remainder radiating away as internal waves. Estimating the dissipation rates for breaking lee waves and wake vortices is particularly challenging, as the analysis in Klymak and Gregg (2004) is based on two-dimensional transect measurements, which limit accuracy. The primary dissipative mechanism near the sill is breaking lee waves associated with hydraulic jumps, accounting for roughly 10% of the energy loss (Klymak and Gregg, 2004). Bottom friction contributes $3-8\%$, while the residual ($\sim 15-20\%$) is presumed to be lost to wake vortices. Despite the limitations of these measurements, the estimated contribution of wake vortices is consistent with parameterizations of flow separation around bluff bodies (Klymak and Gregg, 2004).

The remaining energy radiates away as low-mode internal tides, which can evolve into other forms of internal waves, such as nonlinear solitary waves (NLIWs), particularly upstream of the sill (Farmer and Armi, 1999a; Cummins et al., 2003). These NLIWs may form from the relaxation of the lee wave or the steepening of the internal tide, as observed in the South China Sea (Farmer et al., 2011; Li and Farmer, 2011). Radiating waves may propagate both seaward and landward, encountering bends that potentially cause reflection or breaking. Estimates of the reflection coefficient vary widely, ranging from 1% to $65-93\%$ depending on the data used (Webb and Pond, 1986; Farmer and Freeland, 1983; Freeland, 1984; Marsden and Greenwood, 1994). The limited data available make it challenging to establish a consistent understanding of the reflections.

Not all internal tide energy dissipates before reaching the head of the inlet (Stacey and Pond, 1992). This suggests partial reflection or breaking at the head, but the details of these processes remain unclear. Understanding how these waves interact, whether they reflect, break, or influence subsequent internal tide generation, is an ongoing challenge. While these processes are crucial for understanding the fate of internal tides, they are beyond the scope of this study and will be discussed as potential future research directions.

1.4 Internal Tide Generation, Dissipation, and Propagation

1.4.1 Internal Wave Theory

Internal tides are internal waves of tidal frequency generated by the interaction of stratified flow with bottom topography. Under linearization and hydrostatic approximations, the governing equation for internal waves, following Kundu (2008), is:

$$\frac{\partial^2}{\partial t^2}\nabla^2 w + (\vec{f} \cdot \nabla)^2 w + N^2 \nabla_h^2 w = 0, \tag{1.1}$$

where w is the vertical velocity, $f = 2\Omega \sin\phi$ is the Coriolis frequency, $\Omega = 7.292\times10^{-5}$ rad s^{-1}, ϕ is the latitude, $N = \left(-\frac{g}{\rho}\frac{d\rho}{dz}\right)^{1/2}$ is the buoyancy frequency, g is gravitational acceleration, and ρ is seawater density. This equation can be solved using plane waves or by separating the solution into horizontal and vertical components for confined conditions, where $w = \hat{w}(z)\exp(i(kx - \omega t))$. This leads to an ordinary differential equation (ODE) for $\hat{w}$:

$$\hat{w}_{zz} + m^2(z)\hat{w} = 0, \tag{1.2}$$

where $m^2(z) = k^2 \frac{N^2(z)-\omega^2}{\omega^2 - f^2}$.

With boundary conditions $\hat{w}(0) = 0$ and $\hat{w}(-H) = 0$, this forms a Sturm-Liouville problem with discrete solutions $\hat{w}_n$ and corresponding eigenvalues m_n. Using orthogonality, the solution w can be represented as:

$$w = \sum_n \hat{w}_n(z)\left[a_n \exp(i(kx - \omega t))\right] \tag{1.3}$$

For constant stratification, the vertical mode equation has a sinusoidal solution:

$$\hat{w}n = \sin\left(\frac{n\pi z}{H}\right), \quad n = 1, 2, 3, \ldots \tag{1.4}$$

where n is the mode number. The condition for $m^2 > 0$ is typically satisfied for $|f| \leq \omega \leq N$. Numerical solutions are needed for non-constant stratification, which can be solved by discretizing $\hat{w}_{zz}$ and representing Eq. 1.2 in matrix form. Klymak's Python library (`https://github.com/jklymak/pythonlib/blob/master/vertmodes.py`) has been used for these calculations.

Given $\hat{w}$, the horizontal velocity component $\hat{u}_n = \frac{i}{k}\hat{w}_n'$ can be derived from the continuity equation, indicating that when $\hat{u}$ is at its maximum, $\hat{w}$ is zero, and vice versa.

Plane wave solutions can also be represented as energy propagating along beams with an angle $k_x/k_z = \left(\frac{\omega^2-f^2}{N^2-f^2}\right)^{1/2}$. For constant N, these beams are straight, whereas for variable N, the beams are bent (Figure 1.5). This beam structure becomes sharper as more modes are superposed (Figure 1.6).

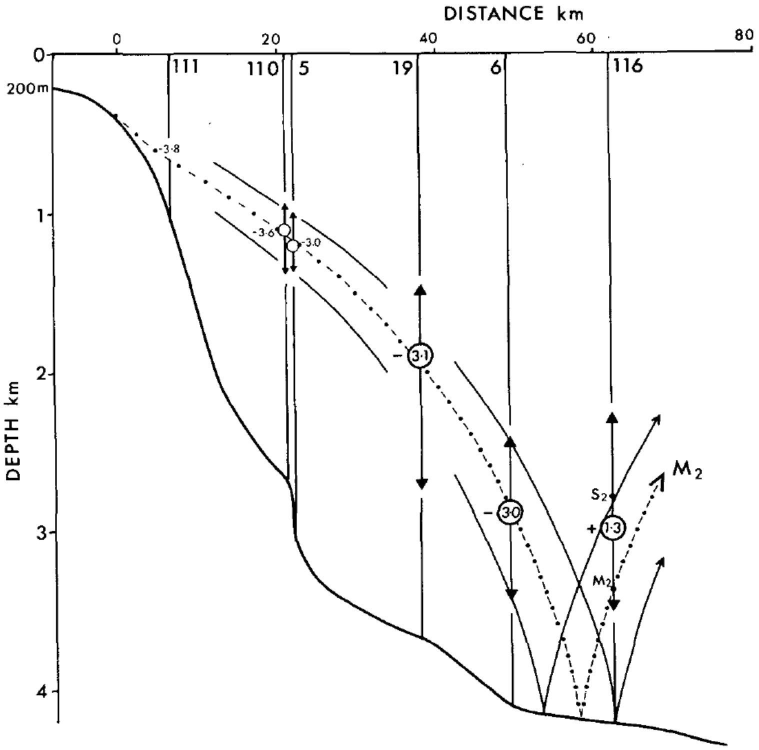

Figure 1.5: The path of an internal tidal beam generated over the continental shelf break in the Bay of Biscay. (Pingree and New, 1991)

Using the dispersion relation, we can calculate the phase speed for each mode. Returning to Eqs. (1.2) and (1.4), we find:

$$m^2 = k^2 \frac{N^2 - \omega^2}{\omega^2 - f^2} = \frac{n^2 \pi^2}{H^2}. \tag{1.5}$$

Assuming $N \gg \omega$ and $\omega \gg f$, we obtain:

$$m^2 = \frac{k^2 N^2}{\omega^2} = \frac{N^2}{c^2}, \tag{1.6}$$

where $c = \frac{\omega}{k}$ represents the horizontal phase speed. Thus, the phase speed is:

$$c = \frac{NH}{n\pi}. \tag{1.7}$$

This result shows that the horizontal phase speed is inversely proportional to the mode number n, meaning higher modes propagate more slowly. Note that this phase speed c is for the case of constant N. For non-constant N, c can be obtained using the numerical method mentioned earlier.

In summary, mode 1 has the longest wavelength and fastest propagation speed, with maximum velocities at the surface and bottom. Higher modes have shorter wavelengths, slower phase speeds, and more zero-crossings. Internal waves propagate along beams, which can also be represented by a superposition of vertical modes.

1.4.2 Internal Tide Generation and Dissipation Across Parameter Regimes

To examine the parameter space governing internal tide generation and dissipation, we consider a barotropic horizontal tidal current U varying with frequency ω, flowing over bottom topography with height h and width $\frac{2\pi}{k}$ in a stratified water column with buoyancy frequency N and depth H. Key non-dimensional parameters include the relative steepness $\epsilon = \frac{kh}{\alpha}$, Nh/U and relative height $\frac{h}{H}$. Here, kh represents the slope of the topography, and $\alpha = \sqrt{\frac{\omega^2 - f^2}{N^2 - \omega^2}}$ denotes the slope of the internal tide beams.

The relative steepness ϵ determines whether the topography is subcritical, critical, or supercritical relative to the internal tide beams. Here, “critical” and “supercritical” refer to the relative steepness of the topography compared to the internal wave characteristic slope, rather than the hydraulic control condition based on the Froude number. Internal tides are preferentially generated where the topographic slope matches the beam slope (critical slope). For subcritical topography, the generated waves propagate primarily upward, while for supercritical topography, waves can propagate both upward and downward. Internal tide generation in subcritical topography can be modeled using linear theory under small amplitude bathymetry (Bell, 1975; Balmforth et al., 2002; Llewellyn Smith and Young, 2002), whereas for supercritical topography the bathymetry is assumed to have an infinite slope (Llewellyn Smith and Young, 2003; St. Laurent et al., 2003).

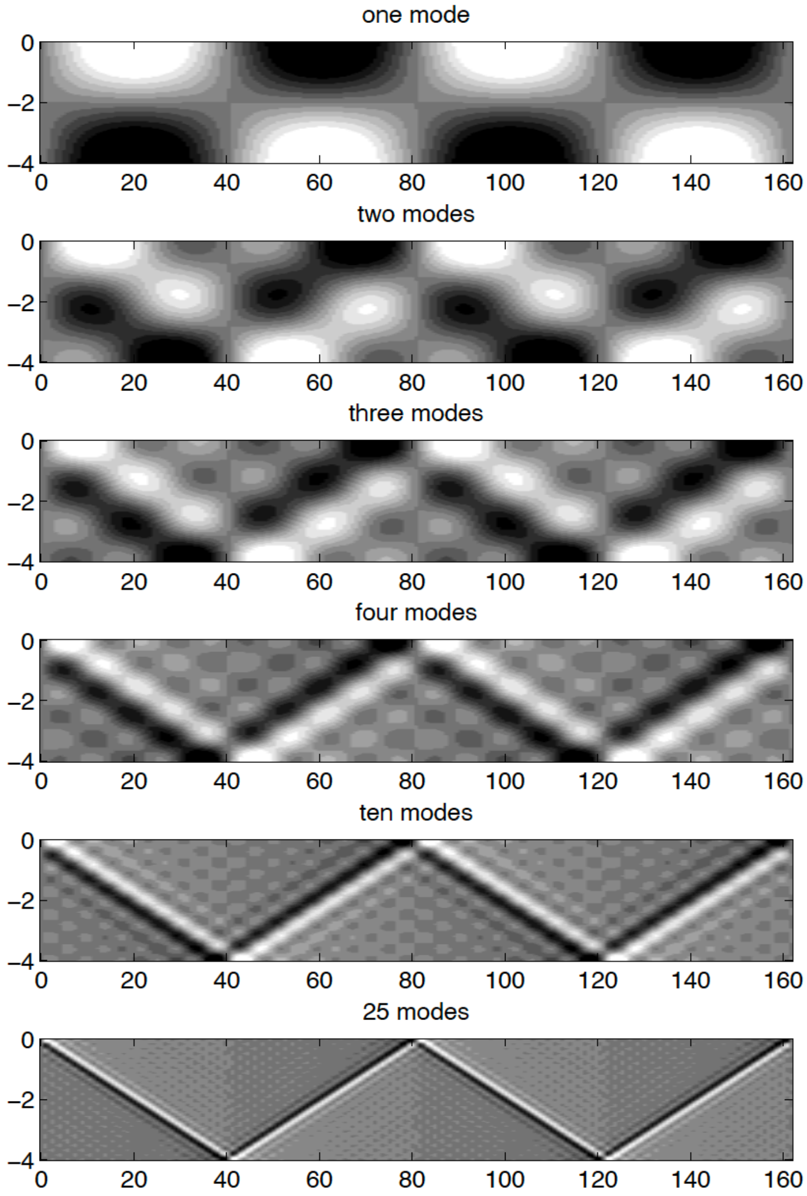

Figure 1.6: Snapshots of the horizontal current velocity (u), where white represents negative values and black indicates positive values, illustrating superpositions with an increasing number of modes. The vertical axis shows water depth, while the horizontal axis represents distance in kilometers. The selected parameters are detailed in Gerkema and Zimmerman (2008). The more modes are superimposed, the sharper the internal tidal beam becomes.

For subcritical topography, the steepness of the obstacle enhances the density gradient, increasing nonlinearity and potentially leading to density overturning (Balmforth et al., 2002). Despite modest topographic slopes in the Brazil Basin, enhanced turbulence at the ocean bottom accounts for approximately 30% of the dissipation, driven by nonlinear wave-wave interactions (Nikurashin and Legg, 2011).

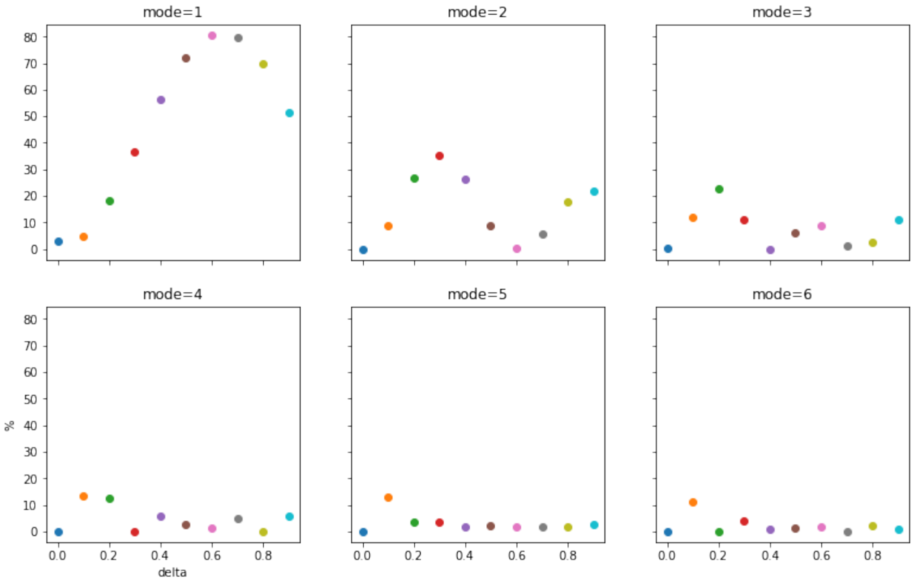

Figure 1.7: Scatter plots of the contribution (%) of each mode (y-axis) as a function of delta ($=\frac{h}{H}$) (x-axis). Each panel represents mode-1 through mode-6. For example, in the first subplot (Mode 1), the contribution increases steadily from 5% to 80% as delta ranges from 0.2 to 0.6, then decreases to 50%. The colors of the scatter points correspond to different h/H values.

Our work focuses on the supercritical slopes at Knight Inlet, analogous to the Hawaiian Ridge. Supercritical topography, with steep slopes acting as a knife-edge barrier (St. Laurent et al., 2003), efficiently converts barotropic tidal energy into baroclinic energy. The conversion rate is quantified as:

$$C = \frac{\rho_0}{2\pi} U^2 N^2 h^2 f_s \left(\frac{h}{H}, \epsilon \right), \tag{1.8}$$

where f_s is a scaling factor dependent on $\frac{h}{H}$ and ϵ. The parameter $\frac{h}{H}$ is important as it determines the modes that are strummed. Lower modes dominate when $\frac{h}{H}$ approaches 1 (Figure 1.7, also available on my GitHub).

The parameter Nh/U, sometimes referred to as the "inverse Froude number"

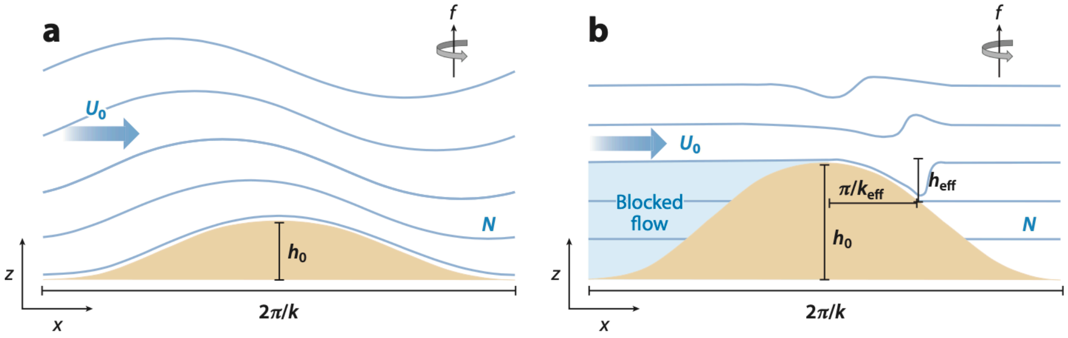

Figure 1.8: (a) Linear lee waves when $\frac{Nh_0}{U_0} < 1$ and (b) non-linear lee waves when $\frac{Nh_0}{U_0} > 1$ characterized with upstream blocking and non-linear hydraulic jumps (Legg, 2021)

(Durran, 1986; Legg and Klymak, 2008; Winters and Armi, 2012), is dynamical relevant in both steady and oscillatory stratified flows over topography. In oscillatory flows with $Nh/U > 1$, quasi-steady trapped lee waves form for sufficiently supercritical slopes. In this study, we use the Nh/U notation, consistent with Baines (1995), while adopting $Fr = U/(Nh)$ in Chapter 3 to align with conventions in wake dynamics literature. For flow with $Nh/U < 1$, linear lee waves form, while for $Nh/U > 1$ non-linear lee waves form with upstream blocking, wherein upstream water cannot cross the crest (Figure 1.8). It can be viewed as a hydraulic-controlled jet forming above the crest, with an internal hydraulic jump downstream (Figure 1.9) (Farmer and Armi, 1999b; Klymak et al., 2010b). The dynamics depend on the unblocked flow velocity $U_c = \frac{H}{H-h}U$ and effective topographic height $h_{\text{eff}} = U/N$ (Klymak et al., 2010a). For Knight Inlet, $Nh/U \approx 10$, is significantly larger than the linear regime ($Nh/U \ll 1$) but smaller than values observed at the Hawaiian Ridge ($Nh/U \sim 100$). Numerical models indicate that for $8 < Nh/U < 20$, lee waves scale with the obstacle height, whereas for $Nh/U > 20$, the waves are relatively smaller Figure 1.10).

The turbulent mixing driven by internal tides on supercritical slopes with $Nh/U > 1$ is influenced by the trapping of specific vertical modes of internal waves. This can be estimated by comparing the barotropic flow speed U_c to the phase speed c_n of the waves. High-mode waves, with slower phase speeds, are more likely to be trapped and dissipate locally, whereas low-mode waves dissipate farther from the generation site (Figure 1.11) (Klymak et al., 2012). The mode trapping threshold is given by:

$$n_c = \frac{NH}{\pi U_c}, \tag{1.9}$$

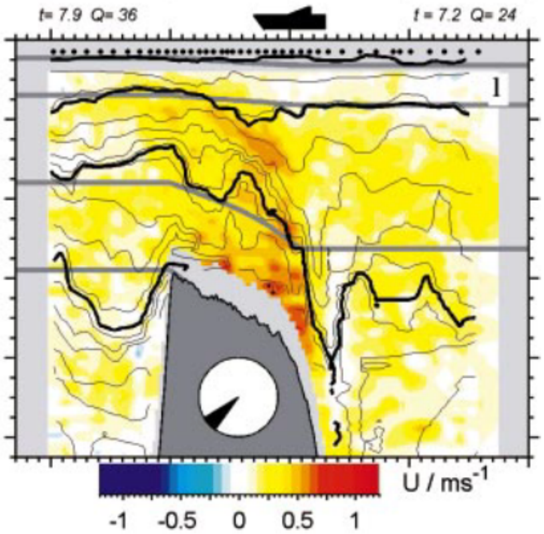

Figure 1.9: Velocity field over the seamount (Klymak and Gregg, 2003), measured using ADCP aboard R/V Miller during a transect from t=7.2 to t=7.9 hours (42 minutes) after high tide, with corresponding tidal fluxes (Q). Isopycnals were derived from CTD measurements. A clock diagram highlights the time span.

assuming constant N and $c_n = \frac{NH}{n_c \pi}$. Since high-mode waves are more likely to be trapped and break locally, the resulting dissipation can be estimated by integrating from n_c to infinity, leading to a cubic scaling with flow speed, as discussed in Chapter 2. Shallow water reduces wave phase speeds and thus increases the number of trapped modes. However, this has only been tested in experiments for $H > 1300\,\mathrm{m}$ (Legg and Klymak, 2008; Klymak et al., 2010b). While studies like those by Stigebrandt (1976) have explored internal tide generation in fjords, they have employed two-layer models that may not fully capture the dynamics of continuously stratified systems.

In this study, we present a novel finding: internal tide generation in settings like Knight Inlet reaches saturation under relatively strong tidal forcing. This behavior, observed in our numerical simulations, represents the first reported instance of such a phenomenon. Saturation occurs when the energy conversion from barotropic to baroclinic tides achieves a limit beyond which additional forcing no longer significantly increases internal tide generation.

To further investigate this behavior, we will examine the conditions under which saturation arises, identify the parameters that govern this process and its implications.

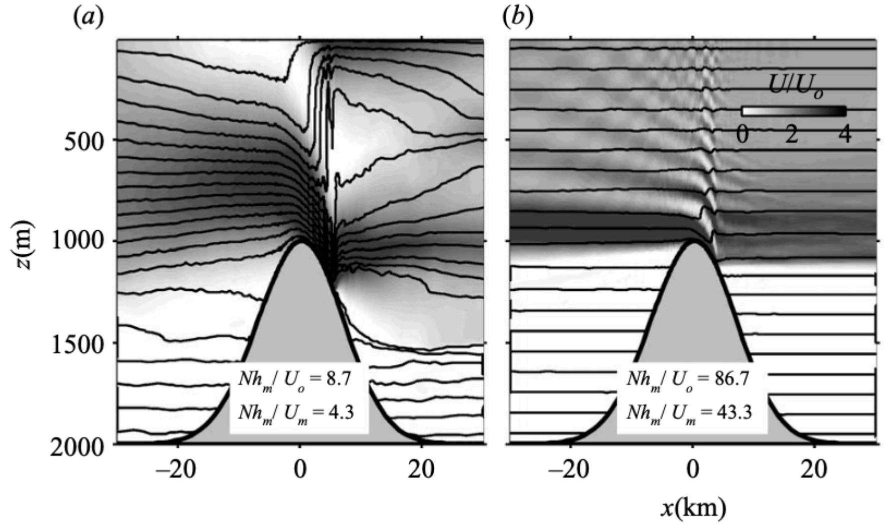

Figure 1.10: (a) $Nh/U = 8.7$ has larger lee wave vertical scale; (b) $Nh/U = 86.7$ has smaller lee waves (Klymak et al., 2010b)

1.4.3 Propagation and Far-field dissipation

The energy converted from the barotropic tide that is not dissipated locally is transported away by radiating internal tides (Ray and Mitchum, 1997). There are many possible sinks for this radiating energy, and indeed there are very few locations where a tidal energy budget has been satisfactorily closed, including Knight Inlet. As they radiate, internal tides may interact with other waves, evolve, and alter their dissipative behavior. Although a detailed discussion of radiation pathways or far-field dissipation is beyond the scope of this study, the generation around the 3D topography provides sufficient content. Below are some examples of possible dissipative processes.

Non-linear wave-wave interactions are a key dissipative process, redistributing energy across scales and forming the Garrett-Munk spectrum (Garrett and Munk, 1975). One significant mechanism is parametric subharmonic instability (PSI), which can drain $10\% - 20\%$ of tidal energy from the Hawaiian Ridge as it approaches 28.9° latitude, where the local Coriolis frequency is half of the M2 tide frequency (Alford et al., 2007; MacKinnon et al., 2013).

Scattering from bathymetry also transfers energy from low-mode to high-mode internal tides, which are more prone to dissipation (Müller and Xu, 1992; Müller and Liu, 2000; Johnston, 2003; Klymak et al., 2013). For example, the North Line Islands ridge scatters approximately 40% of an incoming mode-1 internal tide, while small,

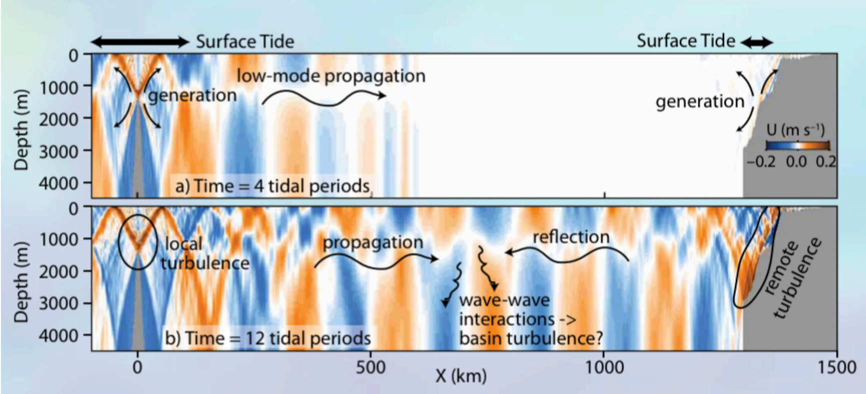

Figure 1.11: A numerical simulation of internal tide generation, local turbulence, low-mode propagation in Klymak et al. (2012)

rough topography south of the ridge scatters only $5\% - 10\%$ (Mathur et al., 2014).

When low-mode internal tides reach continental margins, they may reflect, dissipate, or shoal. For supercritical slopes, reflection dominates (Klymak et al., 2011; Johnston et al., 2015). For near-critical slopes, energy is transferred to high modes, which then dissipate along the slope (Nash et al., 2004; Legg and Adcroft, 2003). For subcritical slopes, internal tides can propagate into shallow waters, enhancing vertical motion and shear, often leading to dissipation (Legg, 2014). As they shoal, internal tides may steepen into non-linear internal waves (NLIWs) with greater amplitudes and shorter periods. On the Washington continental shelf, about 30% of internal tide energy flux transforms into NLIWs (Hamann et al., 2018). In Luzon Strait, semidiurnal internal tides evolve into NLIWs across the South China Sea, capturing approximately 30% of energy flux from deep to shallow waters (Figure 1.12). NLIWs can also form from lee wave relaxation in fjords (Cummins et al., 2003; Farmer and Armi, 1999a), and their high shear and strain result in intense mixing (Klymak and Moum, 2003; Lamb and Farmer, 2011; MacKinnon and Gregg, 2003).

A final potential fate of radiating internal tides is reflection off remote slopes, forming a lossy standing pattern. Despite their role in energy transport, few studies have definitively accounted for the radiated energy.

1.5 Wake vortices and their effect on tides

Underwater topography, which is often three-dimensional, results in cross-flow velocities that influence tidal dynamics. When a headland or underwater sill is sufficiently

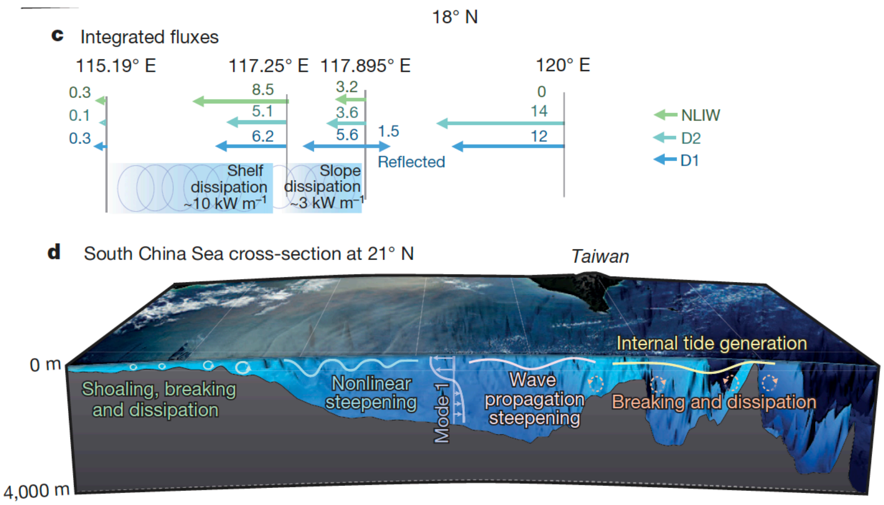

Figure 1.12: Internal wave energy fluxes in the South China Sea. (Alford et al., 2015)

sharp, flow separation can generate coherent vortices (Geyer and Signell, 1990; Klymak and Gregg, 2001; MacCready and Pawlak, 2001). These vortices can contribute significantly to local dissipation, sometimes exceeding the dissipation induced by internal motions like hydraulic jumps and breaking internal waves (Klymak and Gregg, 2004).

Wake vortices can undergo complex behaviors, such as stretching, twisting, and interacting with other vortices. If turbulence does not immediately dissipate them, these vortices can persist and propagate. Vortices in proximity can merge or advect each other, especially if they have opposite circulations. Near rigid boundaries, a single vortex can behave similarly to two counter-rotating vortices, moving along the boundary.

The evolution of vorticity $(\vec{\zeta} = \left(\frac{\partial v}{\partial x} - \frac{\partial u}{\partial y}\right)\hat{k})$ is governed by:

$$\frac{D\vec{\omega}}{Dt} = (\vec{\omega} \cdot \nabla)\vec{v} - \vec{\omega}(\nabla \cdot \vec{v}) + \frac{\nabla\rho \times \nabla p}{\rho^2} + \nabla \times \vec{F}_f, \tag{1.10}$$

where vorticity can change due to tilting, stretching, baroclinic effects, and friction. For example, Farmer et al. (2002) observed vortices downstream of Stuart Island gaining vorticity from baroclinic effects induced by horizontal density gradients in Haro Strait. Wake flows behind obstacles are often characterized by the Reynolds number, $Re = \frac{UD}{\nu}$, where U is the upstream velocity, D the obstacle scale, and ν the eddy viscosity. At low Re, flow remains symmetric without separation. As

Re increases, steady vortices form downstream, eventually creating a ”von Kármán vortex street” and transitioning to turbulence.

Wake vortices lose energy through instabilities. Centrifugal instabilities ($\zeta/f < -1$) enhance turbulence, particularly in anticyclonic shear layers, leading to asymmetric vortex structures (Dong et al., 2007; Gula et al., 2016; Srinivasan et al., 2019, 2021). Barotropic instabilities transfer mean kinetic energy to eddy kinetic energy, while baroclinic instabilities convert eddy potential energy into eddy kinetic energy when the Rossby number (Ro) is around 0.1 (Dong et al., 2007). At $Ro \sim 1$, dissipation becomes symmetric between cyclonic and anticyclonic regions due to vertical shear instabilities (Srinivasan et al., 2021). Observations in Palau and Taiwan’s Green Island also report high vertical shear in wake regions (Chang et al., 2013, 2019; MacKinnon et al., 2019).

In Knight Inlet, wake vortices often form dipoles in the lee of headlands due to boundary layer separation (Klymak and Gregg, 2001). However, the effects of baroclinicity, interactions, and dissipation mechanisms remain unclear. Side-wall friction may also contribute to vortex dissipation.

Form drag is crucial in quantifying energy extraction by tidally-driven vortices from barotropic tides. Vortices create form drag via flow separation, removing energy at a rate given by $P = UF_d$. Near the Knight Inlet sill, headland vortices coexist with internal tides (Klymak and Gregg, 2001). Studies of form drag induced by internal waves and wake vortices are limited due to challenges in distinguishing these contributions. However, research suggests wake-induced form drag can significantly reduce barotropic energy. For example, at Three Tree Point (TTP), form drag from vortices and internal waves was found to be 50 times greater than frictional drag over a flat bottom (Warner et al., 2013; Warner and MacCready, 2014). In Palau, wake vortices caused energy losses tenfold greater than lee wave drag or bottom drag acting on the North Equatorial Current (Johnston et al., 2019). More robust methods are needed to decompose these effects.

Our research aims to clarify the energy relationship between tides, wake vortices, and internal tides through three-dimensional simulations, to understand how to partition tidal energy between wake vortices and internal tides, and the contribution of wake vortices to overall tidal dissipation.

1.6 Existing Problems

Internal tide generation has been extensively studied in deep ocean environments, such as over the supercritical slopes of the Hawaiian ridges, where $Nh/U > 1$. However, much less is understood about these processes in shallow coastal regions, where tidal forcing is stronger, and the dynamics become highly nonlinear.

This study reveals that internal tide generation does not continue to scale with barotropic tidal velocity under extreme forcing conditions; instead, it reaches a saturation point. This challenges traditional scaling relationships from deep ocean studies and underscores the need for further investigation into highly nonlinear regimes in shallow coastal systems.

When barotropic tidal currents interact with three-dimensional topography, part of their energy is converted into internal tides, while another fraction forms wake vortices. The partitioning of this energy and its subsequent pathways—local dissipation, outward propagation, or interactions—are not yet well understood.

1.7 Research Objectives

The primary objective of this study is to advance our understanding of how tidal energy is distributed and dissipated in shallow coastal environments characterized by strong barotropic tidal forcing and complex topography. Specifically, this research aims to address the following questions:

1. Energy saturation in internal tide generation:
    - What are the qualitative flow features observed when energy loss from barotropic tides reaches saturation?
    - How universal is this saturation across different settings of stratification and topographic height?
    - What parameter is associated with the onset and behavior of this saturation?
2. The energetics partition between wake vortices and internal tides:
    - How is tidal energy distributed between internal tide generation and wake vortex formation in a three-dimensional coastal setting?

- What are the dissipation and propagation characteristics of energy in each process?
- Does the presence of wake vortices influence the local dissipation or outward propagation of internal tide energy?

1.8 Structure of Dissertation

This dissertation is organized as follows:

Chapter 2 investigates internal tide generation over isolated topography, focusing on the saturation phenomenon where energy transfer from barotropic tides ceases to scale quadratically with tidal velocity. The chapter characterizes this saturation, including its qualitative flow features associated to hydraulic control conditions and the parameter space where it occurs. This work is currently under revision for submission to the Journal of Physical Oceanography.

Chapter 3 explores the dynamics in complex three-dimensional topographies that feature headlands, analyzing how tidal energy is partitioned between wake vortices and internal tides. It further examines the dissipation and propagation for each process. This chapter is in the final stages of preparation for submission.

Chapter 4 synthesizes the findings, presenting an integrated view of tidal energy pathways and their implications for coastal mixing. The chapter discusses the broader significance of the results and offers suggestions for future research directions.

Chapter 2

Saturation of Internal Tide Generation over Shallow Supercritical Topography

Understanding the conversion of surface tides into internal tides and resulting turbulence is important for oceanic mixing. This study investigates internal tide generation over shallow supercritical obstacles in flows where $Nh/U_0 \sim O(1)$, with N is background stratification, h obstacle height, and U_0 far-field tidal velocity amplitude, particularly relevant in shallow, fjord-like environments where tidal currents become much faster. Previous work has focused on $Nh/U_0 \gg 1$, showing that internal tide generation roughly follows $U_0^2 h^2 N$, and local dissipation follows U_0^3. Here, a faster, linear stratified flow regime is investigated using idealized simulations. Tidal energy conversion follows the U_0^2 power law until crest-top Froude number $Fr_c = U_c/c_1 \approx 1$ (where $U_c = U_0 H/(H-h)$ is the barotropic flow speed at the crest, H is total water depth and $c_1 = \frac{NH}{\pi}$ is the mode-1 phase speed in the deep water), beyond which internal tide generation stops increasing (saturates). Radiation saturates and local dissipation no longer grows as quickly as U_0^3. Qualitatively, the fully stratified flow with $Fr_c > 1$ at the crest resembles approach-controlled flow in two layers (Lawrence, 1993). Radiation from the crest transitions from relatively linear response with well-defined internal tidal beams to strongly non-linear response with diffuse beam as $Fr_c > 1$. However, significant mode-1 internal tides are still radiated into the farfield, contradicting the traditional dichotomy that basins with $Fr_c > 1$ do not generate internal tides (Stigebrandt and Aure, 1989). Simulations with realistic or asymmetric stratification exhibit the same general characteristics as constant-stratification simulations. This saturation conversion when $Fr_c > 1$ should be considered when devising wave drag parameterization used in the models, especially in fjord regions where large Fr_c are likely to be found.

2.1 Introduction

Internal tides, known as baroclinic tides, are internal waves with tidal frequencies, generated by the interaction between tides and rugged topographic features. In global models, the mixing induced by internal tides has a significant impact on the ocean state and the Meridional Overturning Circulation in deep-sea regions (Melet et al., 2013b), as well as climate (Simmons et al., 2004). In fjord environments, internal tides can be a significant source of the mixing (Bourgault and Kelley, 2003; Farmer and Freeland, 1983; Klymak and Gregg, 2004; Wang, 2006; Staalstrøm et al., 2012; Stacey, 2005) that can affect estuarine circulation (New et al., 1987) and facilitate deep water renewal (Staalstrøm and Røed, 2016).

The dynamics of tidal flow over topography are governed by key parameters: tidal current speed in the deep water (U_0), obstacle height (h), total water depth (H), obstacle width (W), buoyancy frequency (N), Coriolis frequency (f), and tidal frequency (ω_0) (Garrett and Kunze, 2007; Legg, 2021). In this study, we neglect rotational effects (f) while we recognize the significance of rotation in subinertial internal tides (Hughes and Klymak, 2019). These parameters lead to key non-dimensional parameters, including the topographic slope ($s = h/W$), and the internal tide beam slope ($\alpha = \omega_0/N$) under the condition $f \ll \omega_0 \ll N$. The tidal excursion parameter ($U_0/\omega_0 W$) represents the ratio of the horizontal displacement of water parcels over a tidal cycle to the width of the obstacle, while Nh/U_0 assesses the linearity of internal tides (Klymak et al., 2010b; Nikurashin and Ferrari, 2010). For infinitesimal topography ($\delta = h/H \ll 1$), Garrett and Kunze (2007) describe flow regimes based on the tidal excursion parameter, but for finite amplitude topography (δ not small), as in our study, Klymak et al. (2010b) demonstrate that the effective excursion parameter becomes equivalent to the relative steepness (γ) due to upstream blocking of the deeper parts of the flow. Therefore, the flows considered here can be thought of as having large effective excursion parameters. We focus on the supercritical regime ($\gamma > 1$) and consider that δ , Nh/U_0 , and γ sufficiently describe the flow properties discussed below.

The generation of internal tides at supercritical slopes can be analytically calculated using the knife-edge model (Llewellyn Smith and Young, 2003; St. Laurent et al., 2003). Knife-edge theory is based on linear dynamics (i.e., neglects advection) and assumes an infinite slope for predicting internal tide generation at supercritical slopes in a finite deep ocean. Conversion is calculated by

$$F_{knife} = F_0 \sum_{n=1}^{\infty} n^{-1} a_n^2, \tag{2.1}$$

where

$$F_0 = \frac{1}{2\pi} \rho \frac{\left(\left(N^2 - \omega_0^2\right)\left(\omega_0^2 - f^2\right)\right)^{1/2}}{\omega_0} U_0^2 H^2, \tag{2.2}$$

n is the number of modes, a_n are the non-dimensional amplitudes of the modes, which depend on δ (St. Laurent et al., 2003), and ρ is seawater density. This prediction has shown general agreement for steep topography with direct observations and numerical models (Papoutsellis et al., 2023; Rainville and Pinkel, 2006; St. Laurent and Nash, 2004). The relationship between U_0 and the conversion rate being proportional to U_0^2 has also been demonstrated not only for the work done by high-mode non-linear lee wave drag (Klymak et al., 2010b), two-layer linear theory for fjords (Stigebrandt and Aure, 1989), and linear theory for subcritical slopes (Bell, 1975; Llewellyn Smith and Young, 2002), but also in recent studies of finite shelves of supercritical slopes (Zemskova et al., 2024).

Fully stratified internal tide generation at supercritical obstacles has been studied in the regime of $Nh/U_0 \gg 1$, with particular application to large mid-ocean ridges like Hawaii (Klymak et al., 2008) and Luzon Strait (Alford et al., 2011), and island chains like Palau (Voet et al., 2020). At this flow regime, there is blocked flow up and downstream of the sill (Baines and Hoinka, 1985), and at peak tidal flow, an arrested, breaking non-linear lee wave manifests on the downstream side of the obstacle with a vertical scale of approximately U/N (Klymak et al., 2010a,b; Winters and Armi, 2012). The asymmetric flow around the ridge crest can be analogous to the internal hydraulic-controlled flow (Farmer and Armi, 1999b; Winters and Armi, 2013; Zemskova and Grisouard, 2021) and the non-linear lee wave can be analogous to the internal hydraulic jump (Legg and Klymak, 2008).

In this flow regime, local dissipation can be associated with slow internal modes that cannot escape the ridge ($c_n < U_c$), where $U_c = UH/(H - h)$ is the barotropic flow at the ridge crest-top. The dissipation scaling can be understood by considering the energy flux of internal waves. According to the knife-edge approximation, the radiation flux into mode n scales as:

$$F_n \sim \frac{U^2}{n^2}. \tag{2.3}$$

Following Klymak et al. (2010a), the modes with phase speeds slower than the mean flow ($c_n < U_c$) are trapped and eventually dissipate locally. The total dissipation can be estimated by summing over the trapped modes, starting from the critical mode n_c, which is given by:

$$n_c = \frac{NH}{\pi U}. \tag{2.4}$$

Integrating the energy flux from n_c to infinity:

$$D \sim \sum_{n=n_c}^{\infty} \frac{U^2}{n^2} \approx \int_{n_c}^{\infty} \frac{U^2}{n^2} dn = U^2 \left[\frac{1}{n_c}\right]. \tag{2.5}$$

Substituting $n_c = NH/(\pi U)$, we obtain:

$$D \sim U^2 \frac{\pi U}{NH}. \tag{2.6}$$

This results in a dissipation scaling of:

$$D \sim U^3. \tag{2.7}$$

Our study reveals a novel aspect of stratified internal tide generation at supercritical topography for fjord-like environments, where the relationship between tidal current speed and energy conversion diverges from the quadratic increase as discussed above. The conversion stops growing as U_0^2 once the flow is fast enough so that a crest Froude number defined by $Fr_c = U_c/c_1 \approx 1$, where U_c is the flow velocity at the ridge crest and $c_1 = NH/\pi$ is the mode-1 phase speed in the deep water for constant stratification. The Froude number (Fr) is a key parameter in hydraulics, typically used to compare the flow speed to the wave speed and assess whether the flow is subcritical ($Fr < 1$) or supercritical ($Fr > 1$). Such $Fr_c \approx 1$ conditions are more likely to be met in fjords due to their typically stronger tidal currents and shallower depths, leading to a higher likelihood of internal tide generation saturation compared to the open ocean.

There is a substantial literature on two-layer flow over topography. An internal hydraulic-controlled flow occurs when internal Froude number is equal to one at the crest and greater than one downstream (Armi, 1986). The flow exhibits lee wave phenomena similar to the deep-ocean case discussed above (Baines and Hoinka, 1985; Farmer and Armi, 1999b) where the crest of the sill is deemed a “critical” hydraulic flow with asymmetric interface across the crest. The lee wave can be thought of as analogous to a downstream hydraulic jump to match the condition where internal Froude number further downstream returns to being less than one. At faster flow speeds the control point moves upstream in what has been termed “approach-controlled flow” (Lawrence, 1993). In the subsequent discussion, to avoid confusion, we will use the term “crest-controlled flow” (Lawrence, 1993) interchangeably with the commonly employed “hydraulic-controlled flow.” Approach-controlled flow has the internal Froude number greater than one from upstream and over the crest and is thus characterized by relatively flat isopycnals across the ridge crest followed by a sharp plunge downstream of the crest (see Fig. 7b,c of Lawrence, 1993). Approach-controlled flow has been observed over coastal sills (Farmer and Denton, 1985; Murray et al., 1984), and our simulations not only show the presence of a similar flow pattern when $Fr_c > 1$ but also associate it with the onset of saturation in tidal conversion.

Fjord sill dynamics in two-layer systems have been distinguished between “wave basins” and “jet basins” based on Fr_c (Stigebrandt, 1976; Stigebrandt and Aure, 1989; Stigebrandt, 2012). Wave basins with $Fr_c < 1$ are where internal tides are produced, and jet basins with $Fr_c > 1$ are where tidal jets are formed and internal tides were believed to not be possible. However, internal tides have been observed in basins that would be categorized as “jet” basins, such as Loch Etive (Inall et al., 2004; Stashchuk et al., 2007), and this study indicates that even for $Fr_c > 1$ internal tides are generated, although they can be very non-linear.

A two-layer analytical hydraulic model by Arneborg et al. (2017) has indications of internal tide generation saturating as Fr_c approaches or exceeds 1. This study focused on the energy budget at lower Fr_c, and did not discuss the specific details within higher Fr_c regime.

Our study examines the saturation of internal tide generation in stratified flows within fjord-like environments, focusing on the energetics of approach-controlled flow and wave/jet basin classification. Using non-hydrostatic numerical simulations over a two-dimensional Gaussian ridge in a rectangular channel, we maintain constant stratification and exclude rotational effects for simplicity. We will address varying stratification in subsequent sections. We present a qualitative analysis of flow characteristics (Section 3.3), a comprehensive evaluation of the baroclinic energy budget, and the criteria for tidal conversion saturation (Section 2.4). Additionally, we study realistic non-linear stratification simplified from Knight Inlet (Klymak and Gregg, 2003) and typical estuary asymmetric stratification, which lead to asymmetric lee waves on either side of the sill (Klymak and Gregg, 2003). Finally, Section 2.5 discusses hydraulic control conditions and internal tide generation in the regime of $Fr_c > 1$. We consider implications for the parameterization of topographic wave drag in barotropic tide models. These typically employ a linear drag approach, leading to quadratic energy conversion (Arbic et al., 2004; Arbic and Scott, 2008; Blakely et al., 2022; Egbert et al., 2004; Jayne and Laurent, 2001), which may be unsuitable in regions with strong tidal currents, such as coastal fjords. This is increasingly relevant as rising sea levels, attributed to climate change, are anticipated to induce significant tidal amplitude changes in coastal areas throughout the 21st century, as highlighted by the IPCC (Bindoff et al., 2019).

2.2 Methods

2.2.1 Model configuration

The MITgcm (Marshall et al., 1997) was used to simulate stratified tidal flow over a Gaussian obstacle to investigate internal tide generation and near-ridge dissipation across a range of flow regimes. For the diagnosis of energy budgets, an online barotropic–baroclinic energy decomposition (Kang and Fringer, 2012; Klymak et al., 2016; Hughes and Klymak, 2019) was used. MITgcm has been demonstrated to accurately capture internal waves, which are crucial in understanding the dynamics of tidal flows over obstacles (Khatiwala, 2003; Musgrave et al., 2017).

The simulations were conducted in a 120-km-long, 3-km-wide channel and aimed to loosely resemble the characteristics of Knight Inlet, including a sill height (h) of 140 m, water depth (H) of 200 m, and a sill width of approximately 2.5 km. Knight Inlet was selected for our study due to its reputation as a natural observatory for studying internal tides on supercritical slopes (Cummins et al., 2003, 2006; Farmer and Smith, 1980b; Farmer and Armi, 1999b; Klymak and Gregg, 2003).

The simulations employed a Cartesian coordinate system (x) centered at the middle of the two-dimensional Gaussian sill. At the scales considered here, the energetics of three-dimensional simulations were identical to those of two-dimensional simula-

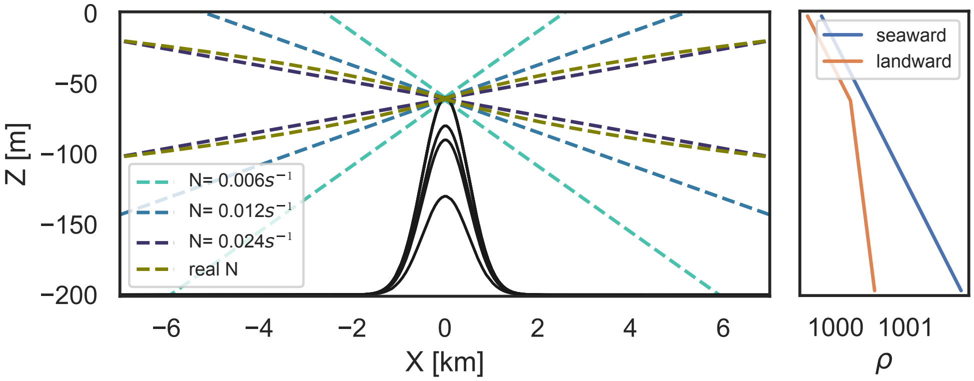

Figure 2.1: Model configuration near the ridge. The black curves represent Gaussian ridges with heights from 70 m to 140 m. The colored dashed curves show the internal tidal beam slopes for different stratifications, with stratification from light blue ($N = 0.006\,\mathrm{s}^{-1}$) to darker blue ($N = 0.024\,\mathrm{s}^{-1}$), and a green curve representing realistic stratification. The right panel displays the density profile used in the asymmetric stratification experiment, with the seaward side having $N = 0.01\,\mathrm{s}^{-1}$, and the landward side featuring an upper layer (65 m) with $N = 0.01\,\mathrm{s}^{-1}$ and a lower layer (135 m) with $N = 0.005\,\mathrm{s}^{-1}$.

tions (see Appendix A), so this paper uses two-dimensional simulations to efficiently cover a wide range of parameters.

The sill profile was defined by the Gaussian function $h = h_0 \exp \frac{-x^2}{a^2}$, with h_0 ranging from 70 to 140 m and $a = 700$, corresponding to a sill width of approximately 2.5 km (see Figure 2.1). The lateral resolution of the model was set to 25 m along the channel ($dx_{min} = 25$ m), with grid cells beyond the central region (-15 km $< x < 15$ km) expanding by 2.7% per cell until reaching a maximum size of $dx_{max} \approx 1225$ m. The vertical resolution was fixed at 5 m, resulting in a total of 40 vertical grid cells. Non-hydrostatic simulations were used because there are differences in the energetics for strong forcing states ($Fr_c = \frac{U_c}{c_1} > 2$) if the hydrostatic approximation is used.

The initial stratification of the model begins with constant N, selecting a value of 1.2×10^{-2} $\mathrm{rad\,s^{-1}}$ as base runs to compare to weaker (6×10^{-3} $\mathrm{rad\,s^{-1}}$) and stronger (2.4×10^{-2} $\mathrm{rad\,s^{-1}}$) stratifications (Figure 2.1 and Table 3.1). Realistic nonlinear N was also examined and the profile was derived from landward profile near the Knight Inlet sill in summer (Klymak and Gregg, 2003) with an average value of approximately 1.138×10^{-2} $\mathrm{rad\,s^{-1}}$. Additionally, we conducted experiments with asymmetric stratifications, mimicking the higher stratification in the seaward basin of Knight Inlet (Klymak and Gregg, 2003). On the landward side, two layers of constant

Runs	a	h [m]	H [m]	$N[\mathrm{rad\,s^{-1}}]$	U_0 [$\mathrm{cm\,s^{-1}}$]	U_c [$\mathrm{cm\,s^{-1}}$]
base run	700	140	200	0.012	4,8,12,16,24,32,48,64	$\sim 13-213$
h70		70			8,12,20,36,48,56,64,72,84	$\sim 12-129$
h110		110			8,12,16,24,32,48,64	$\sim 18-142$
h120		120			8,12,16,24,32,48,64	$20-160$
$N/2$		140		0.006	2,4,8,12,16,24,32	$\sim 7-107$
$2N$		140		0.024	8,16,24,32,48,64,72	$\sim 27-240$
real N		140		$N_{av} = 0.01138$	4,8,12,16,20,24,32,36	$\sim 13-120$
asymmetric N		140		$N_{1s} = 0.01$ (upper 65m) , $N_{2s} = 0.005$ (lower 135m) , $N_l = 0.01$	4,8,12,16,20,24,32	$\sim 13-107$

Table 2.1: Summary of parameters for simulations.

stratification were employed; on the seaward side, one constant stratification was used throughout the water column (Figure 2.1). The density was simulated using a linear equation of state: $\rho = \rho_0\,(1 - \alpha_\theta \theta')$, where $\rho_0 = 999.8\ \mathrm{kg\,m^{-3}}$ and $\alpha_\theta = 2 \times 10^{-4}\ \mathrm{K^{-1}}$.

To drive the tidal currents and density variations in our simulations, nudging boundary conditions were applied at the west and east boundaries. A sponge layer with relaxation timescales of 100 and 1000 s was implemented at the outer and inner edges, respectively, to minimize reflection of internal waves. The tidal forcing was introduced using a sinusoidal function with a period corresponding to the M2 tidal period ($T = 44{,}640$ s, so $\omega = \frac{2\pi}{T} \approx 1.4 \times 10^{-4}\ \mathrm{s^{-1}}$) and a magnitude ($U_0$) ranging from 4 to 80 $\mathrm{cm\,s^{-1}}$ (Table 3.1). The walls and bottom of the model domain were set to a free-slip condition. The additional bottom friction is incorporated as quadratic bottom drag (with $C_d = 1 \times 10^{-3}$). The time step (dt) of 1.24 s was chosen to satisfy the Courant-Friedrichs-Lewy (CFL) stability criterion, so that $C = u\frac{\Delta t}{\Delta x} < 1$. The simulations were run for a duration of 12 tidal cycles.

Viscosity ν_v and diffusivity κ_v were parameterized based on regions of density overturns (Klymak and Legg, 2010) and were assigned low background values ($\kappa_h = \nu_h = 2 \times 10^{-2}\ \mathrm{m^2\,s^{-1}}$, $\kappa_v = \nu_v = 10^{-5}\ \mathrm{m^2\,s^{-1}}$) to maintain numerical stability. We tested the sensitivity of the results to different background diffusivity and viscosity. We found that varying these parameters primarily affected the calculated horizontal dissipation term in the energy budget, while other components remained largely unchanged. Based on these tests, we selected $\kappa_h = \nu_h = 10^{-2}$, as this choice provided dissipation values that resulted in the most closed energy budget. The presence of second-order flux-limiting temperature advection scheme (tempAdvScheme = 77; see the MITgcm manual) introduced some numerical diffusivity and dissipation, as noted in Klymak and Legg (2010).

2.2.2 Barotropic-baroclinic energy decomposition

Decomposition of barotropic and baroclinic energy (Kang and Fringer, 2012) is used to determine the baroclinic energy budgets and dissipation in our simulations. This decomposition is carried out online in our simulations (i.e., not post-processing) to capture the energy in real-time. A depth-integrated, tidally-averaged energy equation is used in the analysis. In a steady, tidally forced system, the barotropic tidal energy is either dissipated in the bottom boundary layer or converted into baroclinic energy. Baroclinic energy can further leave the system as an internal wave energy flux, dissipate in the interior, or dissipate at the bottom boundary layer. The vertically integrated energy budgets becomes

$$\begin{aligned} \frac{1}{T}\Delta\overline{E_0} + \nabla_H \cdot \left\langle \overline{\mathbf{F}_0} \right\rangle &= -\langle \bar{C} \rangle - \langle \overline{\epsilon_0} + D_0 \rangle \,, \\ \frac{1}{T}\Delta\overline{E'} + \nabla_H \cdot \left\langle \overline{\mathbf{F}'} \right\rangle &= \langle \bar{C} \rangle - \left\langle \overline{\epsilon'} + D' \right\rangle \,, \end{aligned} \tag{2.8}$$

where E is tidal energy, F is tidal energy flux, C is conversion from barotropic (BT) to baroclinic (BC) energy, ϵ is turbulence dissipation and D is bottom boundary layer dissipation. Barotropic and baroclinic components are denoted by subscript 0 and prime, respectively. The overbars denote depth integrals, while the angle brackets implicate tidal averages.

We decompose barotropic and baroclinic motions by defining the depth-average properties as barotropic motion for ease of online calculation. This approach can lead to temporary misallocations between barotropic and baroclinic components, especially under conditions of large surface tides, particularly in the estimation of pressure fields because barotropic pressure includes a depth-dependent component due to surface heaving effects (Kelly et al., 2010). However, the misallocated energy is reallocated back after over a distance less than a mode-1 wavelength in our simulations.

In this paper, we focus on the conversion term C, which plays a central role in connecting the energy budgets of barotropic and baroclinic energies, as

$$\overline{C} = \overline{\rho' g W} - \overline{q_z W} + A_{h0} \tag{2.9}$$

(Kang, 2011, Eq. 5.102). The first term is the dominant component of conversion as the linear, hydrostatic part. Here, ρ' represents a density perturbation, and $W(z)$ is the vertical velocity arising from the convergence or divergence of horizontal barotropic flow between the seafloor and depth z. The second term represents the non-hydrostatic contribution to the conversion, q is the non-hydrostatic part of the pressure. The third component is the non-linear term as

$$A_{h0} = \rho_0 (U \nabla_H \cdot \overline{\mathbf{u}'_H u'} + V \nabla_H \cdot \overline{\mathbf{u}'_H v'}), \tag{2.10}$$

where uppercase, lowercase, and primed velocities refer to the barotropic, complete, and baroclinic components, respectively, and the subscript H pertains to the horizontal component.

Following conversion, baroclinic energy undergoes two processes: local dissipation, which we integrate over a 10-km wide control volume centered on the ridge, and propagation out of the system. The component that leaves the system is described by the depth-integrated baroclinic flux, denoted as $\overline{F'} = \overline{u'p'} + \overline{uE'}$, where p' is baroclinic pressure perturbation (Kang, 2011, Eq. 5.102). We neglect the diffusive components of F' as they are negligible.

The dissipation at the bottom boundary layer is divided into barotropic and baroclinic components, represented as

$$\begin{aligned} D_0 &= \rho_0 C_d \mathbf{u}_H (uU + vV), \\ D' &= \rho_0 C_d \mathbf{u}_H (uu' + vv' + w^2). \end{aligned} \tag{2.11}$$

This decomposition is non-unique, so we follow the convention used by Carter et al. (2008), Kang and Fringer (2012) and Hughes and Klymak (2019) for consistency.

Turbulent dissipation due to vertical shear ϵ_v is obtained from the modeled vertical viscosity as

$$\epsilon'_v = \rho_0 \nu_v \left(\left(\frac{\partial u}{\partial z} \right)^2 + \left(\frac{\partial v}{\partial z} \right)^2 \right), \tag{2.12}$$

and horizontal dissipation is calculated as

$$\epsilon'_h = \rho_0 \nu_H \left(\nabla_H \mathbf{u}'_H \cdot \nabla_H \mathbf{u}'_H \right). \tag{2.13}$$

2.3 Phenomenology: increasing tidal forcing

Before examining the response of the flow to different tidal forcings, we will first focus on how the flow behaves over a single tidal cycle under relatively strong forcing ($Nh/U_0 \sim 7$, Figure 2.2). While there are similarities to well-studied tidal-driven non-linear trapped internal lee waves (Klymak et al., 2010a; Winters and Armi, 2012;

Legg, 2021) – where lee waves form downstream of the ridge crest during both flood and ebb tides, deepen as tides strengthen (Figure 2.2b-c,f-g), and collapse before slack tide (Figure 2.2d,h), this experiment here appears even more non-linear. Isopycnals exhibit increased non-linear structures, such as bores and seesaw patterns. We still observe features characteristic of the lee wave regime ($Nh/U_0 > 1$), such as upstream blocking and breaking lee waves analogous to hydraulic jumps. These breaking waves occur more dramatically, accompanied by several undular bores trailing the breaking waves (Figure 2.2c,d,g,h).

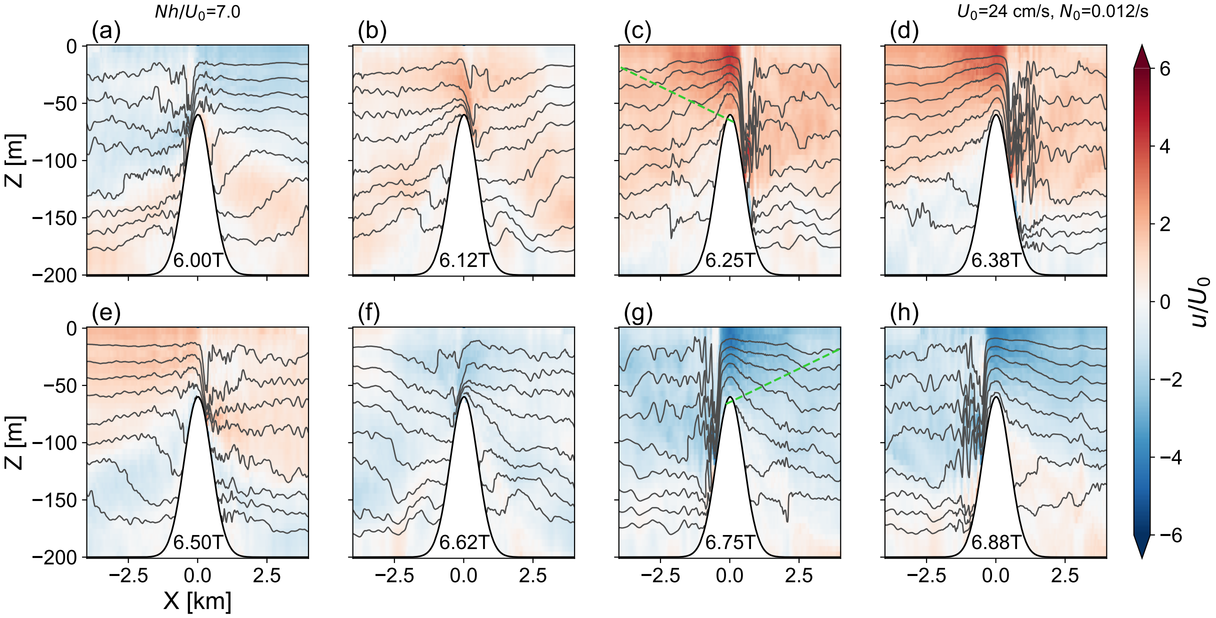

Figure 2.2: Snapshots of velocity and density over a tidal cycle when $Nh/U_0 = 7$, where $U_0 = 24\ \mathrm{cm\,s^{-1}}$, $N = 1.2 \times 10^{-2}\ \mathrm{rad\,s^{-1}}$, and $h = 140$ m. (a,e) is during slack tide and (c,g) is during peak tide. Density contours are uniformly spaced in depth (every 20 m), which, due to constant stratification, also results in uniform spacing in density. Green dash curves in (c,g) are the slope of internal tides beam.

The changes in flow due to varying tidal forcing are noteworthy because they reveal key differences in the flow dynamics and control conditions (Figure 2.3). First, under strong forcing, the flow is less blocked, allowing more water climb up the ridge crest (Figure 2.3d-f). Second, the nature of the control at the crest changes as forcing increases. The isopycnal plunges across the ridge crest (Figure 2.3a,b) – the feature of a crest-controlled flow – are pushed farther downstream, becoming sharper and sharper (Figure 2.3d-f). This isopycnals become relatively flat and symmetric across the ridge before plunging abruptly downstream, characteristics that resemble approach-controlled flow in two layer (Lawrence, 1993). As the isopycnal plunge becomes sharper and more pronounced, the following hydraulic jump becomes more dramatic, often accompanied by large-amplitude undular bores. It is important to note that here is 2D simulation, and the undular bores may not be as prominent in a three-dimensional flow. Third, the accelerated flow is no longer attached to the ridge as a strong downslope flow and a horizontal jet (Figure 2.3a,b); instead, it is concentrated above the crest near the surface and near the base of the isopycnal plunge (Figure 2.3d-f).

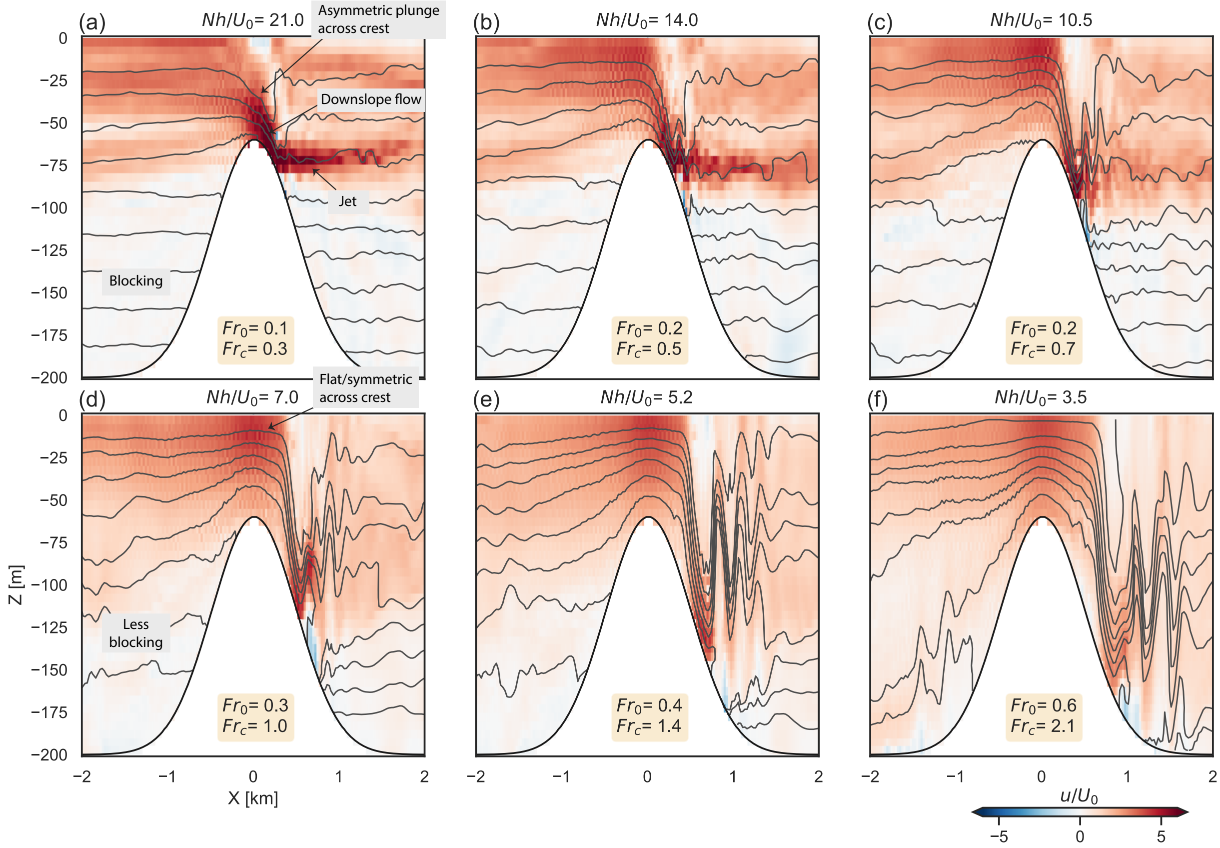

Figure 2.3: Snapshots of velocity and density at peak flood tide (t=6.25 cycle) as tidal forcing U_0 increases from 8 to 48 cm s^{-1} for $h = 140$ m, $N = 1.2 \times 10^{-2}$ rad s^{-1}. Density contours are uniformly spaced in depth (every 20 m), which, due to constant stratification, also results in uniform spacing in density. Nh/U_0, $Fr_0 = U_0/c_1$ and $Fr_c = U_c/c_1$ also are indicated. Flow resembles two stages, from (a-c) crest-controlled flow to (d-f) approach-controlled flow.

As tidal forcing is increased, the flow undergoes a transition from crest-controlled to approach-controlled flow (Figure 2.3). Weaker tidal forcing exhibits crest-controlled flow (Figure 2.3a-c), while stronger forcing has approach-controlled flow (Figure 2.3d-f), with a transition around $7 < Nh/U_0 < 10.5$. The transition from crest-controlled to approach-controlled occurs when the flow speed at the top of the crest ($U_c = U(H-h)/H$) is approximately equal to the mode-1 phase speed in the deep part of the channel ($c_1 = NH/\pi$), meaning $Fr_c \sim 1$. A more precise quantification of the transition can be found in later results, since here is qualitative.

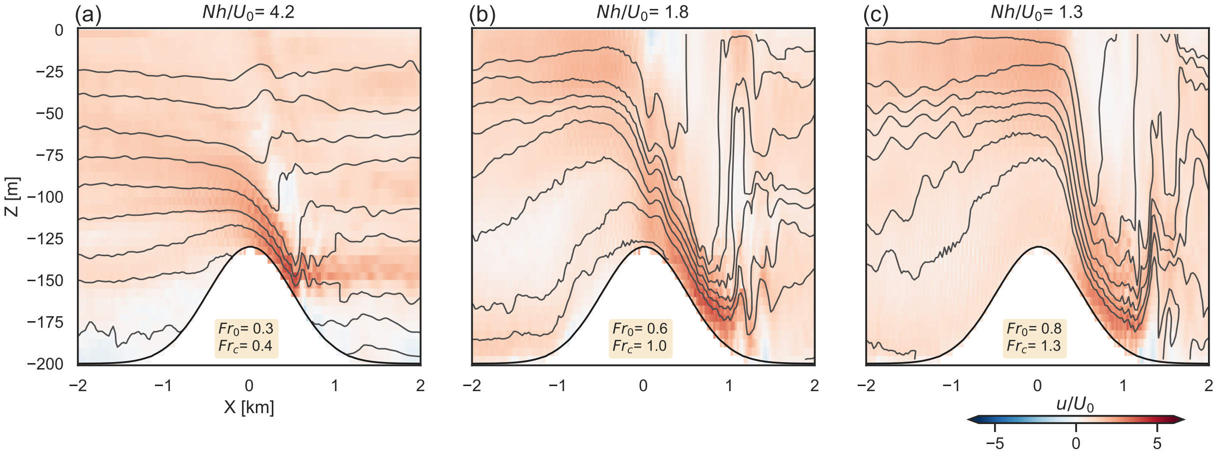

Figure 2.4: As in Figure 2.3, except $h = 70$ m. Tidal forcing U_0 increases from 12 to 84 $\mathrm{cm\,s^{-1}}$. Flow also resembles two stages in this lower ridge, (a) crest-controlled flow and (c) approach-controlled flow.

We test this with lower ridges ($\delta = 0.35$) and observe similar patterns of transition from crest-controlled to approach-controlled flow (Figure 2.4), indicating the change of control is not exclusive to high ridges. The transition for this lower ridge occurs around different forcing, and different Nh/U_0 (~ 1.8) (Figure 2.4b). The isopycnals plunge farther downstream (Figure 2.4c). Notably, the crest-top flow speed U_c also approximates mode-1 phase speed c_1 when the transition occurs. The crest-top Froude number $Fr_c = U_c/c_1 \sim 1$ criterion for detecting the control changes seems to be reinforced by testing different ridge heights.

Simulations with the stratification doubled and halved show the same change in response at crest-top Froude number (Fr_c) of approximately 1. While plots of these flow changes are not included in this subsection, the corresponding energy budgets are discussed below.

2.4 Baroclinic energy budgets

In this section, we examine the energetics of the flow as it transitions from crest-controlled to approach-controlled by increasing the tidal forcing as shown in the previous section. We do this by calculating the rate that energy is put into the baroclinic tide (or the conversion term), and assess the fraction that is locally dissipated due to turbulence versus the fraction that radiates away as baroclinic waves, where "locally" is a 10-km long control volume centered on the obstacle (Equation (2.8)). The results at weaker forcing follow previous literature, where conversion scale proportionally with U_0^2, but as forcing increases and $Fr_c > 1$ the conversion and radiation terms in the energy budget saturate.

2.4.1 Dependence on tidal amplitude

The saturation of barotropic to baroclinic conversion can be seen in a pair of simulation suites that have the same stratification ($N = 1.2 \times 10^{-2}$ rad s^{-1}), ridge heights of 140 or 70 m, and a variety of velocity forcing from 0.06 to 0.84 m s^{-1} (Figure 2.5). The knife edge prediction for the conversion rate scales as U_0^2 (black lines). The simulated conversion, $\langle \bar{C} \rangle$ (Figure 2.5, green curves), follows the knife-edge prediction at small velocities, but saturates as the velocities increase in both simulation suites. For the lower ridge, the conversion even experiences a decline.

Baroclinic radiation from the 10-km control volume, $\nabla \cdot \langle \bar{F'} \rangle$ (Figure 2.5, orange curves), follows a trend similar to the conversion, shifting from a nearly quadratic increase under weak tidal forcing and plateauing as tidal forcing strengthens. The radiation falls off somewhat more strongly because dissipation continues to increase for both topographic heights. The vertical dissipation rate, $\langle \bar{\epsilon_v} \rangle$ (Figure 2.5, red curves), dominates the dissipation terms, and increases slightly faster than cubically with tidal forcing and then less quickly when the baroclinic conversion saturates. For the lower ridge (Figure 2.5b, d) dissipation even drops as the saturation condition is reached.

The enhanced turbulent dissipation at strong tidal forcing reduces the stratification near the ridge, but only by 15% (Figure 2.6e,f). This is not sufficient to account for the reduced conversion, as indicated the modified knife-edge model (in the linear relationship with stratification, gray lines).

The fraction of energy dissipated is approximately 10% for the weaker flows, and increases to over 40% of the conversion for stronger flows, and exceeds the fraction that radiates (Figure 2.5c,d). These fractions resembles the energy distribution observed in various locations: Knight Inlet, where 67% of energy is radiated away, and 33% is dissipated near the sill (Klymak and Gregg, 2004); Hawaiian Ridge, 15% (Klymak et al., 2006); Mendocino Escarpment, 28% (Musgrave et al., 2016); Luzon Strait, 40% (Alford et al., 2015), but differs from Oslo Fjord, where it ranges from 60 to 90% (Staalstrøm et al., 2015). In mixing parameterization of global models, the fraction of energy dissipated locally is often chosen to be 30% (St. Laurent et al., 2002).

The horizontal dissipation $\langle \bar{\epsilon_h} \rangle$ and bottom friction dissipation $\langle D' \rangle$ have minimal contributions to the local dissipation (Figure 2.5a,b, purple and blue curves), with quadratic growth (i.e., similar slope with black lines) before saturation and the nearly parallel trend with vertical dissipation after saturation. Our energy budget has a residual of approximately 10 to 15% of the conversion term in all scenarios (Figure 2.5c,d, gray x), potentially arising from numerical dissipation (Klymak and Legg, 2010), consistent with other studies employing a similar methodology (Hughes and Klymak, 2019).

2.4.2 Saturation criteria

Given the parameters of the problem, h, H, N, and U_0, we seek a parameter that collapses the response of the conversion so we can predict when saturation will be reached for a given flow. Barotropic to baroclinic conversion is calculated with different ridge heights and background stratification (Figure 2.6). Conversion saturation occurs across all tested simulations, as each curve is initially straight (proportional to U_0^2), then progressively bends (Figure 2.6a). However, the specific point at when saturation occurs depends on N and h.

To compare different simulation scenarios, we normalized each simulation by the expected conversion from the knife edge model, which predicts internal tide generation on supercritical ridges as discussed in Section 3.1. After normalizing each simulation by the expected conversion from the knife edge model, the most non-dimensional similarity of the saturation was achieved by using Fr_c (Figure 2.6d). Other normalizations (Figure 2.6b,c) showed a wider spread, particularly for different obstacle heights, indicating that the barotropic speed over the obstacle was an important factor. The saturation curves are not perfect, even when normalizing by Fr_c, and the shortest obstacle, $h = 70$ m in particular has an apparent resonance near $Fr_c = 1$. However, most of the simulations start to saturate at about $Fr_c \approx 0.5 - 0.7$.

The onset of saturation corresponds with the qualitative occurrence of approach-controlled flow, as indicated by their Nh/U_0 and Fr_c values presented in our plots (Figure 2.3 and Figure 2.4). For instance, for the 140-m tall ridge, the simulation with $Fr_c > 0.7$ ($Nh/U_0 < 10.5$, Figure 2.3c) is approximately when the conversion starts to saturate (Figure 2.6b,d). In that simulation, and the ones with stronger barotropic forcing, the isopycnals over the top of the ridge can be seen to become flat, with a sharp drop on the downstream side. The same phenomena – shifting control condition (Figure 2.4) corresponding to conversion saturation – happens for the shorter ridge, but at a higher velocity (pink curve, Figure 2.6a), lower Nh/U_0 (< 2, pink curve in Figure 2.6b) and similar Fr_c (Figure 2.6d).

The full suite of simulations has relatively similar responses for the radiation and dissipation across the range of Fr_c (Figure 2.7), with the fraction of dissipation increasing as Fr_c increases (Figure 2.7d). The radiation (Figure 2.7a) response follows a growth pattern proportional to U_0^2 when tidal forcing is weak, reaching a saturation point as $Fr_c > 1$. Dissipation (Figure 2.7b) shows a power-law dependence on U_0. For higher ridges (blue curves), the dissipation transitions from a faster-than-expected cubic decay to a nearly square behavior when $Fr_c > 1$. For lower ridges (the pink to purple curves), the dissipation reaches nearly constant when $Fr_c > 1$. The curves with the same stratification (pink to purple curves and middle blue one) do not collapse as in radiation (Figure 2.7a), with the lowest ridge having proportionally larger dissipation, likely due to its larger absolute value of U_0^3.

2.4.3 Realistic stratification

Having shown the saturation phenomenon in the constant stratification simulations, we now demonstrate that the same phenomena occurs for realistic non-linear stratifications. First, we use the simplified summer landward density profile from the Knight Inlet observation (Klymak and Gregg, 2003). The density profile exhibits a sharp pycnocline and a weak ($\sim 2 \times 10^{-3}$ $\mathrm{rad\,s^{-1}}$) and uniform bottom stratification within about the bottom 50 m, with an average stratification of 1.138×10^{-2} $\mathrm{rad\,s^{-1}}$ and mode-1 speed of 0.8471 $\mathrm{m\,s^{-1}}$.

The changes in the control of the flow observed in realistic stratification experiments are the same as those observed in constant stratification experiments (Figure 2.8). Non-linear trapped internal lee waves are seen when the tidal forcing is weaker ($Fr_c < 1$,Figure 2.8a). When $Fr_c > 1$, the flow becomes symmetric over the sill, indicate of approach-controlled flow (Figure 2.8c). The sharp isopycnal drops of Figure 2.8c and Figure 2.3e, both exhibiting the same Fr_c, are similar. Isopycnals show more overturns on both the upstream and downstream sides than the one with constant N. The upstream blocking is easier to overcome than constant N due to the weaker stratification at the bottom.

These simulations exhibit the same saturation of energy conversion (green curve, Figure 2.9) as constant stratification simulations. The knife-edge model under the realistic stratification requires consideration of WKB-stretching for h_{wkb} and U_{0wkb}. Accordingly, $(H-h)_{wkb} = \int_{-H+h}^{0} N dz/N_{av} \approx 122.06$ m, so $\delta_{wkb} = h_{wkb}/H = 0.3897$. Next, $F_{knife}/F_0 = \sum_{n=1}^{\infty} n^{-1} a_n^2$, where a_n are non-dimensional coefficients of each mode determined by δ (St. Laurent et al., 2003). Consequently, $F_{knife}/F_0 = 0.802$. From $F_0 = \frac{\pi}{2}\rho U_{0wkb}^2 H^2 \frac{((N_{av}^2-\omega^2)(\omega^2-f^2))^{0.5}}{\omega} L_y$ and $U_{0wkb} = U_0(N_{av}/N)^{0.5}$, we can obtain F_{knife}. The conversion (green curve) closely aligns with the knife-edge model when $Fr_c < 1$; , saturation is observed for higher Fr_c in the realistic simulations. The results of baroclinic radiation (orange curve) and dissipation (red curve) are similar to those of constant stratification, with both showing saturation at $Fr_c > 1$, but the realistic stratification exhibits slower growth of radiation when $Fr_c < 1$, as the slope of the orange curve is less than quadratic (compared to the U_0^2 relationship seen in constant stratification (orange curve, Figure 2.5a)). This reduced growth is linked to greater dissipation, which is greater than the dissipation in constant stratification (red curve, Figure 2.5a). This increased dissipation can be seen as more zigzags in isopycnals (Figure 2.8) compared to Figure 2.3.

2.4.4 Asymmetrical stratification

A similar saturation of the energy terms occurs when the stratification is unequal in the basins on either side of the obstacle. This situation is typical of estuaries, where denser seawater flows into the estuary and less dense freshwater flows from the landward basin. The size of the lee waves formed either side of the sill is shown to be different under such asymmetric stratification (Klymak and Gregg, 2003). The stratification used here is shown in Figure 2.1. Seaward side density is always greater than landward side density at every depth level. We calculate the energy budget still in the 10-km long control volume centered on the obstacle, even acknowledging baroclinic energy behaves differently on either side of the sill. We use the density of the seaward side for potential energy calculations in MITgcm to avoid potential energy changes caused by intruding water on the landward side. The knife-edge model is also computed using the seaward side stratification.

Despite the asymmetric response of flow on either side of the sill during flood and ebb tides due to asymmetric stratification, the transition of flow control (Figure 2.10) and energy saturation (Figure 2.11) still occurs at $Fr_c \sim 1$. The asymmetry is consistent with Klymak and Gregg (2003), where lee waves reach deeper on the side with weaker stratification. Denser water intrudes landward (Figure 2.10b-f), indicated by the green curves. The conversion closely aligns with the knife-edge model when $Fr_c < 0.8$ but is slightly lower due to the choice of the seaward side for calculations (green curves, Figure 2.11). Afterwards, the conversion and baroclinic radiation start to saturate (orange curves), similar to the constant and realistic stratification experiments. Vertical dissipation (red curve) shows an overall nearly quadratic trend.

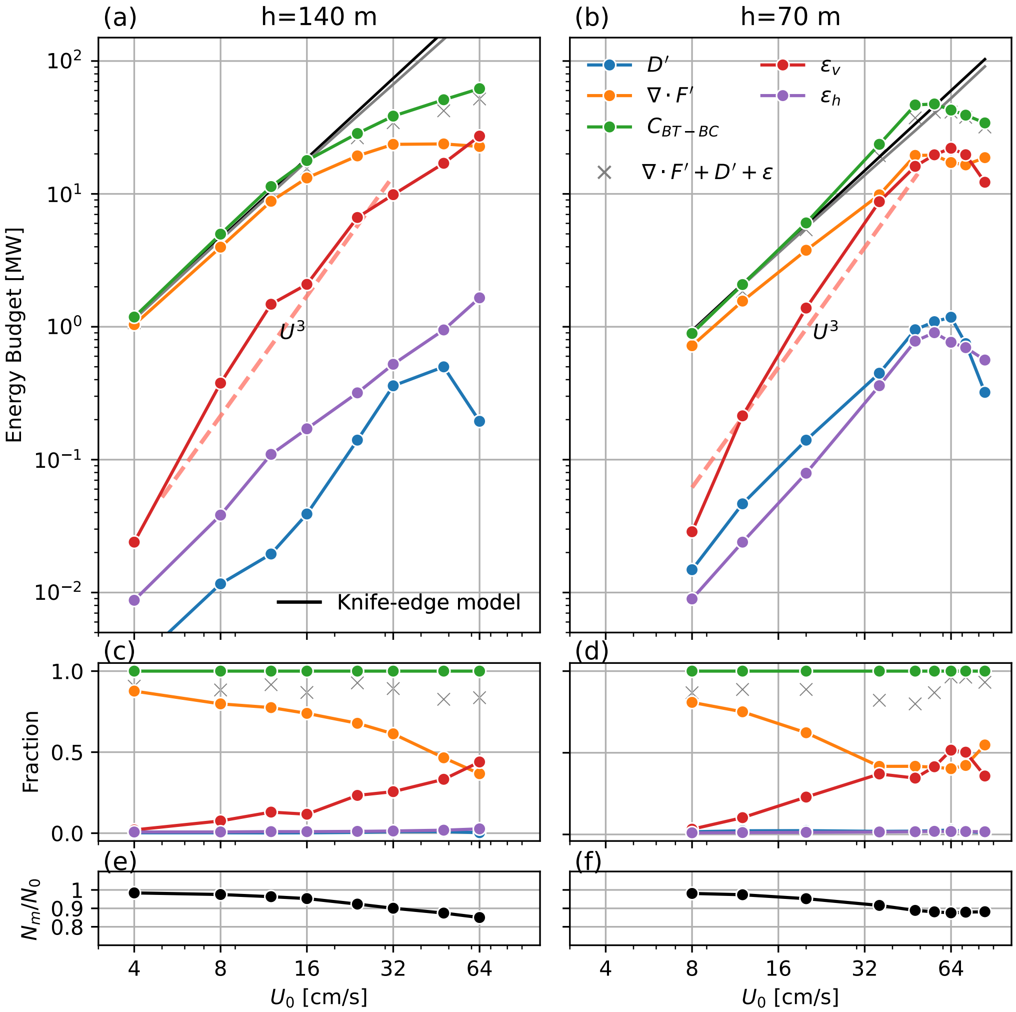

Figure 2.5: Left panel is $h = 140$ m and right panal is $h = 70$ m. (a,b) Baroclinic energy budgets within ±5 km for $N = 1.2 \times 10^{-3}$ rad s^{-1} and (c,d) the fraction of the baroclinic energy budgets to conversion versus the tidal forcing U_0. Green curves are barotropic-baroclinic energy conversion $\langle \bar{C} \rangle$, orange ones are the divergence of baroclinic energy flux $\nabla \cdot \langle \bar{F}' \rangle$ (or baroclinic radiation), red ones are vertical dissipation $\langle \bar{\epsilon_v} \rangle$, purple ones are horizontal dissipation $\langle \bar{\epsilon_h} \rangle$, blue ones are bottom friction $\langle D' \rangle$. Black lines are knife-edge prediction in a square relationship to U_0 (St. Laurent et al., 2003). (e,f) are the scaled mean stratification near the ridge (away from sill 2 to 5 km). Modified knife-edge solution by the mean stratification in (a,b) as gray lines. A plateau is shown in both conversion and radiation when strong tidal forcing, what we called conversion saturation.

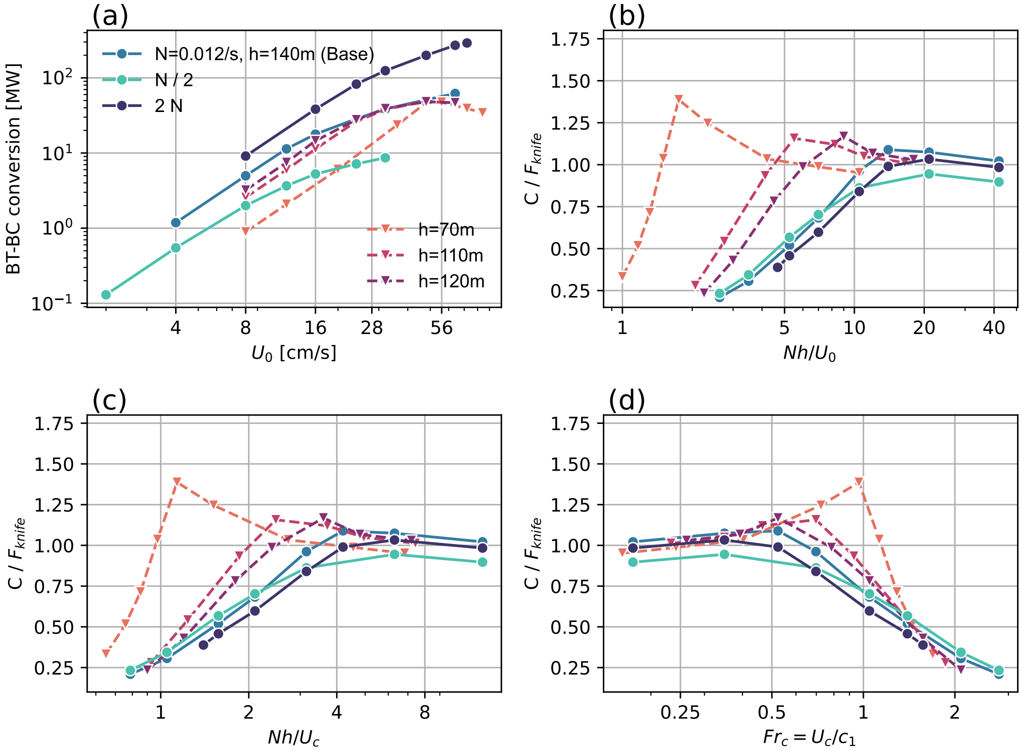

Figure 2.6: (a) Barotropic-baroclinic conversion versus the tidal forcing U_0 and normalized conversion by knife-edge prediction versus (b) Nh/U_0, (c) Nh/U_c, and (d) $Fr_c = \frac{U_c}{c_1}$, where U_c is the barotropic flow speed at crest and c_1 is the internal tide mode-1 speed, in different experiments. The blue series represents experiments with differing stratification intensities, with darker shades of blue indicating increased stratification. Conversely, the pink to purple spectrum represents experiments with varying ridge heights, where deeper hues correspond to higher ridges. The best collapse of the saturation was achieved using Fr_c while most of the simulations start to saturate at about $Fr_c \approx 0.5 - 0.7$.

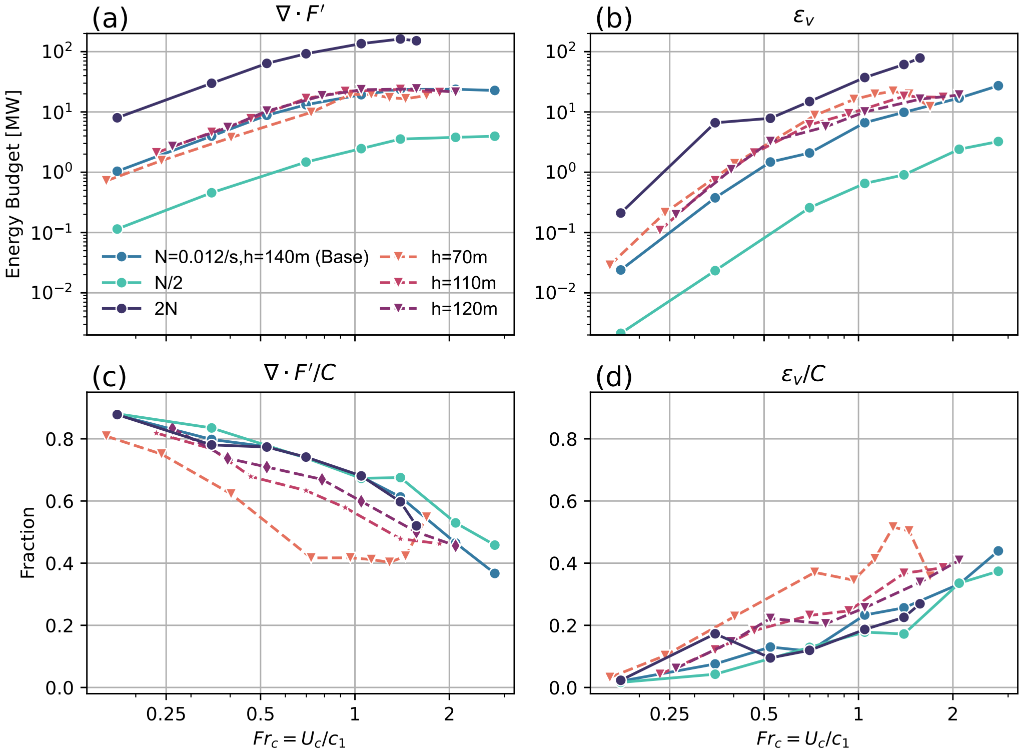

Figure 2.7: (a) Baroclinic radiation and (c) its fraction to conversion, and (b) vertical dissipation and (d) its fraction to conversion versus $Fr_c = \frac{U_c}{c_1}$, where U_c is the barotropic flow speed at crest and c_1 is the internal tide mode-1 speed, in different experiments. The blue series represents experiments with differing stratification intensities, with darker shades of blue indicating increased stratification. Conversely, the pink to purple spectrum represents experiments with varying ridge heights, where deeper hues correspond to higher ridges.

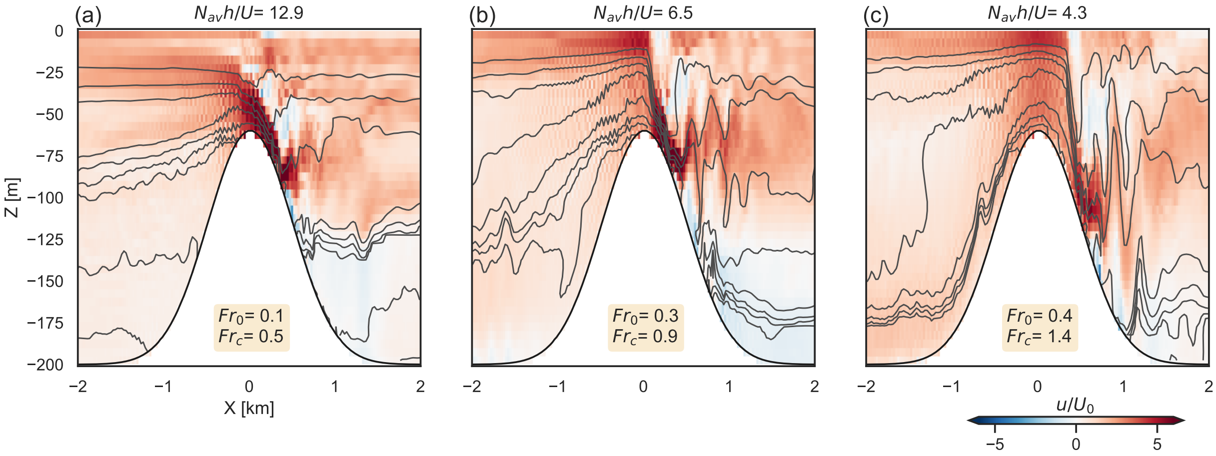

Figure 2.8: Snapshots of velocity and density at peak flood tide with a realistic, non-constant stratification at flood tide as tidal forcing U_0 increases from 8 to 36 $\mathrm{cm\,s^{-1}}$ for $h = 140$ m. Initial stratification N is the simplified N profile from Knight Inlet (Klymak and Gregg, 2003). Contours are uniformly spaced in depths (20 m per layer) on initial density but appear non-uniformly spaced in density due to non-constant stratification. Nh/U_0, $Fr_0 = U_0/c_1$ and $Fr_c = U_c/c_1$ also are indicated. The control of the flow also changes in this realistic N experiments, resembling (a) crest-controlled and (c) approach-controlled flow.

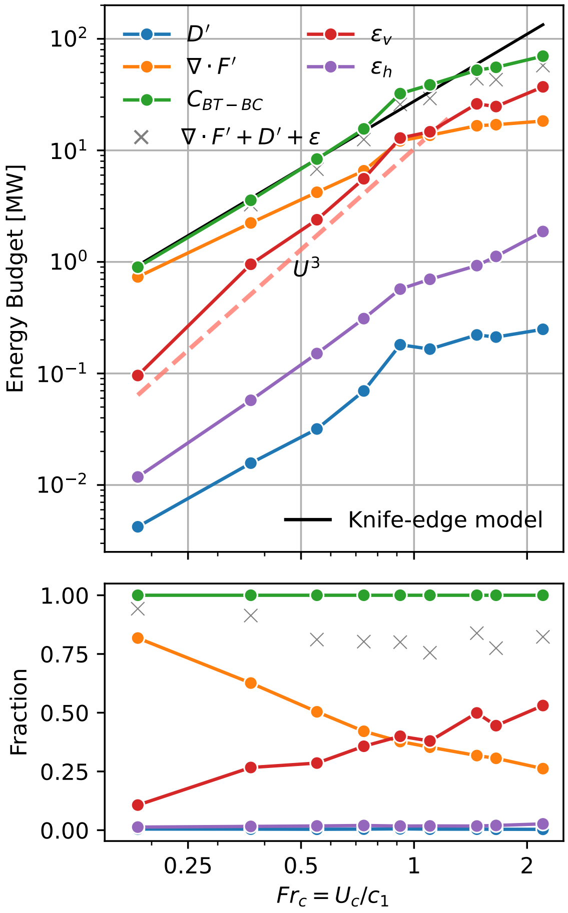

Figure 2.9: Baroclinic energy budgets within ±5 km and the fraction of the baroclinic energy budgets to conversion for $h = 140$ m with a realistic, non-constant stratification versus $Fr_c = U_c/c_1$. The colors indicating different energy components are the same as those used in Figure 2.5. Black lines are knife-edge prediction in a square relationship to U_0 (St. Laurent et al., 2003). Conversion saturation also occurs at $Fr_c \sim 1$ in realistic stratification.

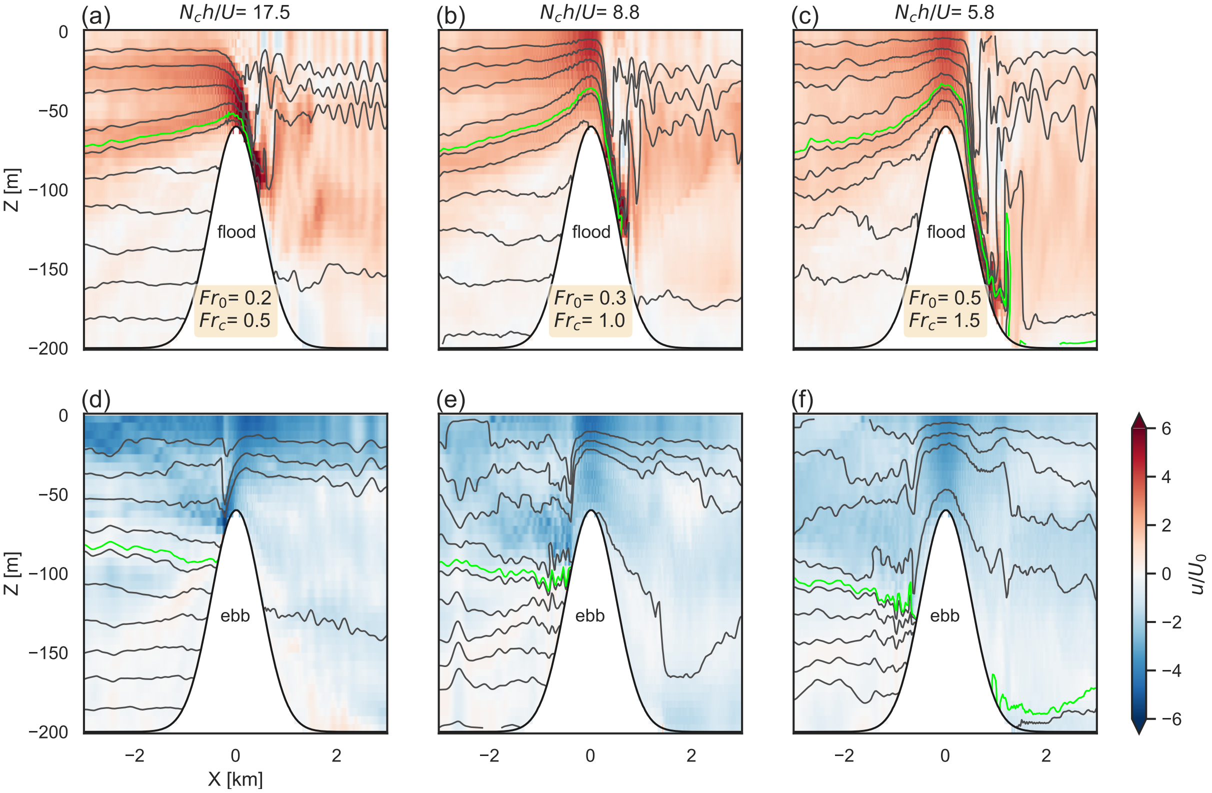

Figure 2.10: Snapshots of velocity and density from the simulation with the unequal stratifications on either side of the obstacle at flood (upper) and ebb (lower) tide as tidal forcing increases from 8 to 24 $\mathrm{cm\,s^{-1}}$ for h = 140 m. Asymmetric stratification is typical of estuaries: seaward with denser water (left side), and landward with less dense freshwater (right side). Contours are non-uniformly spaced in density but uniformly spaced in depths (20 m per layer) on initial seaward density. Green curves are the densest isopycnals for the landward side. Nh/U_0, U_0/c_1 and U_c/c_1 also are indicated. The control of the flow also can be seen with this specific stratification; resembling (a,d) crest-controlled and (c,f) approach-controlled flow.

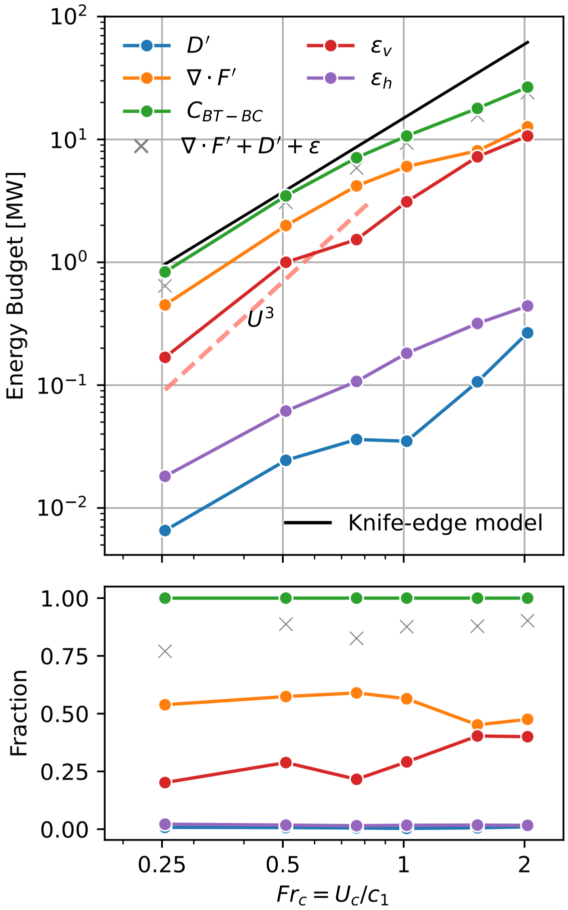

Figure 2.11: Baroclinic energy budgets within ± 5km for $h = 140$ m with the unequal stratifications on either side of the obstacle versus $Fr_c = U_c/c_1$. The colors indicating different energy components are the same as those used in Figure 2.5. Black lines are knife-edge prediction in a square relationship to U_0 (St. Laurent et al., 2003). Conversion saturation also occurs at $Fr_c \sim 1$ in asymmetric stratification.

2.5 Summary and discussion

As flow velocity increases, in a strongly non-linear parameter space explored in this study, the corresponding range of Nh/U_0 declines from $O(10)$ to $O(1)$, altering the flow dynamics near ridges from typical lee waves to a distinctive pattern with symmetric flow near the ridge crest, followed by sharply rapid isopycnal plunging downstream and dramatic hydraulic jumps further downstream. This pattern resembles "approach-controlled flow." Upstream blocking may be entirely overcome at higher flow velocities. From an energy perspective, the conversion from tidal to internal tide energy no longer adheres to knife-edge theory, rather saturating with flow velocity instead of quadratic scaling when $Fr_c = U_c/c_1 > 1$. This affects the subsequent baroclinic energy radiation and local dissipation, with radiation saturating and local dissipation growing at a slower rate than cubic to flow velocity, still leading to an increasing dissipation ratio of up to 40%. All of these features can be seen in the simulations with constant, realistic, asymmetric stratification.

2.5.1 Evaluating hydraulic controls

In our investigation of tidal dynamics, we identified a correlation between the crest Froude number (Fr_c) nearing or exceeding 1 and the emergence of flow characteristics resembling approach-controlled flow, which coincides with the saturation of tidal energy conversion. This subsection further examines the hydraulic conditions using the two-layer composite Froude number (G) and the undisturbed composite Froude number (G_0).

The two-layer composite Froude number G is given by:

$$G^2 = F_1^2 + F_2^2 - eF_1^2F_2^2, \tag{2.14}$$

where $e = (\rho_2 - \rho_1)/\rho_2$, $F_1 = u_1/g'h_1$, $F_2 = u_2/g'h_2$, ρ_1 and ρ_2 are the seawater densities of the upper and lower layers, respectively, and u_1 and u_2 are the depth-averaged flow velocities of the upper and lower layers, respectively. The undisturbed composite Froude number G_0 is defined as:

$$G_0 = \frac{q}{(g'r(1-r)H^3)^{0.5}}, \tag{2.15}$$

where q is the flow rate and $r = q_2/q$ and q_2 is the flow rate of lower layer (Lawrence, 1993). Note G_0 is meaningful far away from the ridge, representing the undisturbed state. To classify the flow, we use Lawrence (1993)'s method, which compares G_0 with critical values. The lower critical G_0 (Figure 2.12e-h, lower gray dashed line) represents the threshold for approach-controlled flow, while the higher one (Figure 2.12e-h, higher gray dashed line) corresponds to supercritical flow. The threshold for approach-controlled flow mainly varies with the obstacle height (Figure 8 in Lawrence, 1993), being approximately 0.45 for $\delta = 0.35$ (Figure 2.12g,h, lower gray dashed line) and 0.15 for $\delta = 0.7$ (Figure 2.12e,f, lower gray dashed line), whereas the threshold for supercritical flow remains constant at 1 (Figure 2.12e-h, higher gray dashed line). This indicates that the approach-controlled flow regime is more likely for higher obstacles (with a G_0 range of 0.15–1) compared to lower obstacles (0.45–1). Additionally, while transforming a continuously stratified flow into a two-layer system, we find that G is sensitive to the choice of layer interface. However, G_0 is not affected much by this choice.

The trend of G along x-axis illustrates the difference in hydraulic control conditions between flow resembling approach-controlled and crest-controlled flow (Figure 2.12). In the case of crest-controlled flow (Figure 2.12a,c), G exhibits a sharp peak (G_{max}) with the value approaching or exceeding 1 at the crest (orange curves in Figure 2.12e,g). Conversely, for approach-controlled flow (Figure 2.12b,d), G presents a wider spatial extent near the ridge crest, with G values surpassing the value away from ridge (orange curves in Figure 2.12f,h). While the choice of isopycnal affects the absolute value of G, our focus is on identifying threshold behavior. We found that selecting the isopycnal near the middle of the water column—just above the ridge and close to the jet—produced the highest G_{max} , making it the most suitable for assessing the threshold. In contrast, choosing an isopycnal closer to the bottom or surface resulted in lower G_{max}.

Lawrence (1993) classification method, which compares G_0 with critical G_0 values (as shown by the blue curves and gray dashed lines in Figure 2.12 e-h, respectively), is generally consistent with the flow behaviors and our Fr_c-based analysis. In scenarios where Fr_c was significantly less than 1 (Figure 2.12a,c), G_0 (blue curves, Figure 2.12e,g) remained below the lower critical threshold (lower gray dash line) indicative of crest-controlled flow. For cases around $Fr_c \sim 1$ (Figure 2.12b,d), G_0 (blue curves, Figure 2.12f,h) exceeded the lower critical value (lower gray dash line), suggesting approach-controlled flow conditions. The higher critical threshold (higher gray dash line), associated with supercritical flow, will only be exceeded in cases with

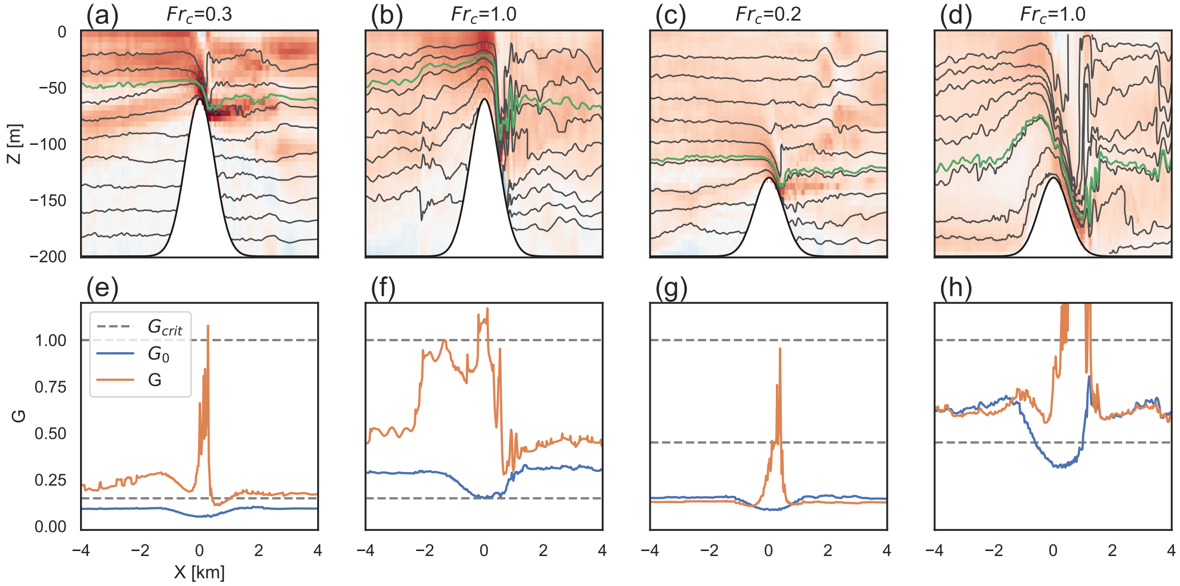

Figure 2.12: Snapshots of velocity and density at flood tide (a-d) and corresponding composite Froude numbers (e-h) for different cases: (a,e) $Fr_c = 0.3$, $Nh/U_0 = 21$, (b,f) $Fr_c = 1.0$, $Nh/U_0 = 7$, (c,g) $Fr_c = 0.2$, $Nh/U_0 = 7$, (d,h) $Fr_c = 1.0$, $Nh/U_0 = 1.8$. The green curves in (a-d) are the selected two-layer interface in order to calculate their corresponding composite internal Froude number G (orange curves in e-h), and the undisturbed composite Froude number G_0 (blue curves in e-h calculated by Equation (2.15)). The lower critical threshold for approach-controlled flow is shown by lower gray dash lines, and higher threshold for supercritical flow is shown by upper gray dash lines. The threshold for approach-controlled flow varies with obstacle height, being approximately 0.45 for $h/H = 0.35$ (g,h) and 0.15 for $h/H = 0.7$ (e,f) (values obtained from Figure 8 in Lawrence, 1993), while the supercritical flow threshold remains constant at 1.

even stronger forcing or weaker stratification (see Equation (2.15)).

For our case of the lower ridge with $Fr_c \sim 1$ (Figure 2.12 d), the flow does not yet display the perfect alignment with the typical patterns of approach-controlled flow. At $Fr_c = 1$, the characteristics still qualitatively lean toward crest-controlled flow (Figure 2.4b), whereas at $Fr_c \sim 1.1$, the flow appears to be in a transitional state (not shown). By $Fr_c \sim 1.3$, the approach-controlled flow features qualitatively become much more pronounced (Figure 2.4c). Despite this, at $Fr_c \sim 1$, the G_0 method already shows values exceeding the critical G_0, suggesting a consistency with the onset of tidal energy conversion saturation. Therefore, while Fr_c is a quite robust criteria for identifying saturation, G_0 computation could provide an additional means, even though the question of why changes in hydraulic control conditions lead to tidal energy saturation remains. This is particularly relevant when observation of internal tides near lower ridges might not clearly indicate approach-controlled characteristics; in such cases, both Fr_c and G_0 could be helpful in discerning whether conversion saturation has occurred.

2.5.2 Internal tide generation in the regime of $Fr_c > 1$

In the fjord-related literature, it has been believed that basins with $Fr_c > 1$, often referred to as tidal jet basins, do not generate internal tides (Stigebrandt, 1976; Stigebrandt and Aure, 1989). This subsection revisits this regime, proposing that internal tides can indeed form under these conditions. Our findings, showing near-field flow pattern that align with those observed in other studies, where internal tides were detected despite $Fr_c > 1$, support this, along with evidence of far-field wave propagation in our simulations.

Our analysis of near-field flow patterns, although not directly indicative of internal tides, shows similarities to those observed in studies where internal tides were detected in the far-field (Inall et al., 2004, 2005; Stashchuk et al., 2007). These characteristics include a jet attached along the slope that flattens downstream, similar to the typical lee waves generated when the flow is crest-controlled (Fig. 8 of Stashchuk et al. (2007) v.s. Figure 2.8a at 50 m $< z <$ 80 m and $0 < x <\sim 2$ km). As the flow strengthens (Fig. 9 of Stashchuk et al. (2007)), the isopycnals above the ridge crest become flatter, with surface flow intensifying, and then abruptly plunging downstream until reaching the ridge surface. The hydraulic jump further downstream is also evident. After the jump, the jet continues horizontally. These similarities align with the characteristics of approach-controlled flow, which are very analogous to our simulation results (Figure 2.8c at 0 m $< z <$ 80 m and $0 < x < 0.5$ km).

In the far-field, our simulations directly indicate that internal tides radiate, though their character becomes more and more non-linear (Figure 2.13). The presence of mode-1 waves extending away from the ridge at high Fr_c values, aligning with the concept that internal tides can indeed be generated in such flow as $Fr_c > 1$. Inall et al. (2004) and Stashchuk et al. (2007) reported mode-1 internal tides downstream, ranging from 2 km to 15 km when $Fr_c > 1$ in Loch Etive. In our case, the perturbation with tidal frequency are shown across all the temporal snapshots in Figure 2.13 even to a downstream distance of 38 km with $Fr_c \sim 2$ (Figure 2.13i). As Fr_c increased, there is a transition in the wave train from a more linear and sinusoidal form to a non-linear pattern. Comparing our results to Loch Etive observations at 2 km downstream (Fig 10 in Stashchuk et al., 2007), both the observations and our simulations identified short steep troughs and longer flatter crests at subsurface depths, as depicted in Figure 2.13b,c.

	Energy [MW]	C	$\nabla \cdot F'$	ϵ	D'	$\nabla \cdot F' + \epsilon + D'$
$Fr = 0.5$	5km	11.63	9.07 (78 %)	1.32 (11 %)	0.02 (0.1 %)	10.41 (89.5 %)
	38km	11.53	7.82 (68 %)	1.49 (13 %)	0.97(8 %)	10.28 (89.1 %)
	$\Delta_{(38km-5km)}$	-0.09	-1.25	+0.16	+0.95	-0.13
$Fr = 1.0$	5km	29.27	20.09 (69 %)	6.58 (22 %)	0.11 (0.4 %)	26.78 (91.5 %)
	38km	28.77	16.06 (56 %)	7.60 (26 %)	2.52 (9 %)	26.18 (91.0 %)
	$\Delta_{(38km-5km)}$	-0.51	-4.03	+1.02	+2.41	-0.60
$Fr = 2.1$	5km	54.64	26.18 (48 %)	21.32 (39 %)	0.54 (1 %)	48.05 (87.9 %)
	38km	54.35	19.98 (37 %)	24.18 (44 %)	3.74 (7 %)	47.90 (88.1 %)
	$\Delta_{(38km-5km)}$	-0.29	-6.21	+2.86	+3.20	-0.15

Table 2.2: Baroclinic energy budgets at $x = 5$ km and $x = 38$ km for $Fr_c = 0.5$, $Fr_c = 1.0$, and $Fr_c = 2.1$.

Our simulation results challenge the traditional dichotomy of tidal jet and wave basins based on Fr_c. Contrary to previous classifications, our findings suggest that supercritical flow conditions ($Fr_c > 1$) do not inhibit the generation of internal tides.

Further into the far-field, we observe different patterns for both when $Fr_c < 1$ and $Fr_c > 1$ (Figure 2.14 and Figure 2.15). For $Fr_c < 1$, the far-field flow exhibits typical internal tide propagation, with internal waves radiating outward at a constant phase speed. This is evident from the Hovmöller diagrams, where the phase propagation appears as a straight diagonal line (Figure 2.14a), indicating that the waves travel at a steady speed over time. Additionally, there is a consistent phase relationship between the off-ridge (i.e., where background tides move away from the ridge) and on-ridge (i.e., where background tides move toward the ridge) components of the flow (also can see from $x - z$ snapshot Figure 2.15a,d,g).

As Fr_c exceeds 1 (Figure 2.14b and Figure 2.15b,e,h), we begin to observe variations in the phase propagation speed, and the phase relationship between the off-ridge and on-ridge components becomes more distinct. By $Fr_c \sim 2$ (Figure 2.14c), these differences become very pronounced. On the right-hand side of the ridge, the phase with westward velocity in the upper water column tends to exhibit a shorter wavelength compared to the one with eastward velocity (Figure 2.14c and Figure 2.15c,f,i). Additionally, the phase propagation speed varies significantly between flood and ebb tides (Figure 2.14c). These patterns indicate a distinctive and noteworthy hydrodynamic mechanism in regimes where $Fr_c > 1$, in contrast to linear propagation seen in $Fr_c < 1$. A full exploration of these mechanisms, however, lies beyond the scope of our study.

Nonlinearity significantly increases as $Fr_c > 1$, characterised by a more diffuse tidal beam and pronounced undulations in the isopycnals (Figure 2.15b,c,e,f,h,i), when comparing the less non-linear flow ($Fr_c < 1$) in Figure 2.15a,d,g. The dissipation also grows with increasing Fr_c (red curves, Figure 2.15j-l). Despite this, the tidally-averaged baroclinic energy flux still shows approximately 37% radiating away at 38 km (orange curves in Figure 2.15l and Table 2.2), indicating that a notable amount of waves propagating even at this distance when $Fr_c \sim 2$. These flux are mostly mode-1 waves by observing one zero-crossing in Figure 2.13 and Figure 2.15 and modal energy flux distribution (not shown). As mentioned in Section 3.2, the energy flux along the channel (orange curves in Figure 2.15l) is showing temporary misallocations between 5 km and 40 km due to the way we decomposed the barotropic and baroclinic components (Kelly et al., 2010), it returns back to neutral position around 38km, over the span of one mode-1 wavelength. The outstanding question of where these mode-1 waves dissipate remains in this strong non-linear scenario.

The evidence presented strongly suggests that the regime where $Fr_c > 1$ not only supports the generation of internal tides but also introduces complexities in their formation and propagation that needs further investigation.

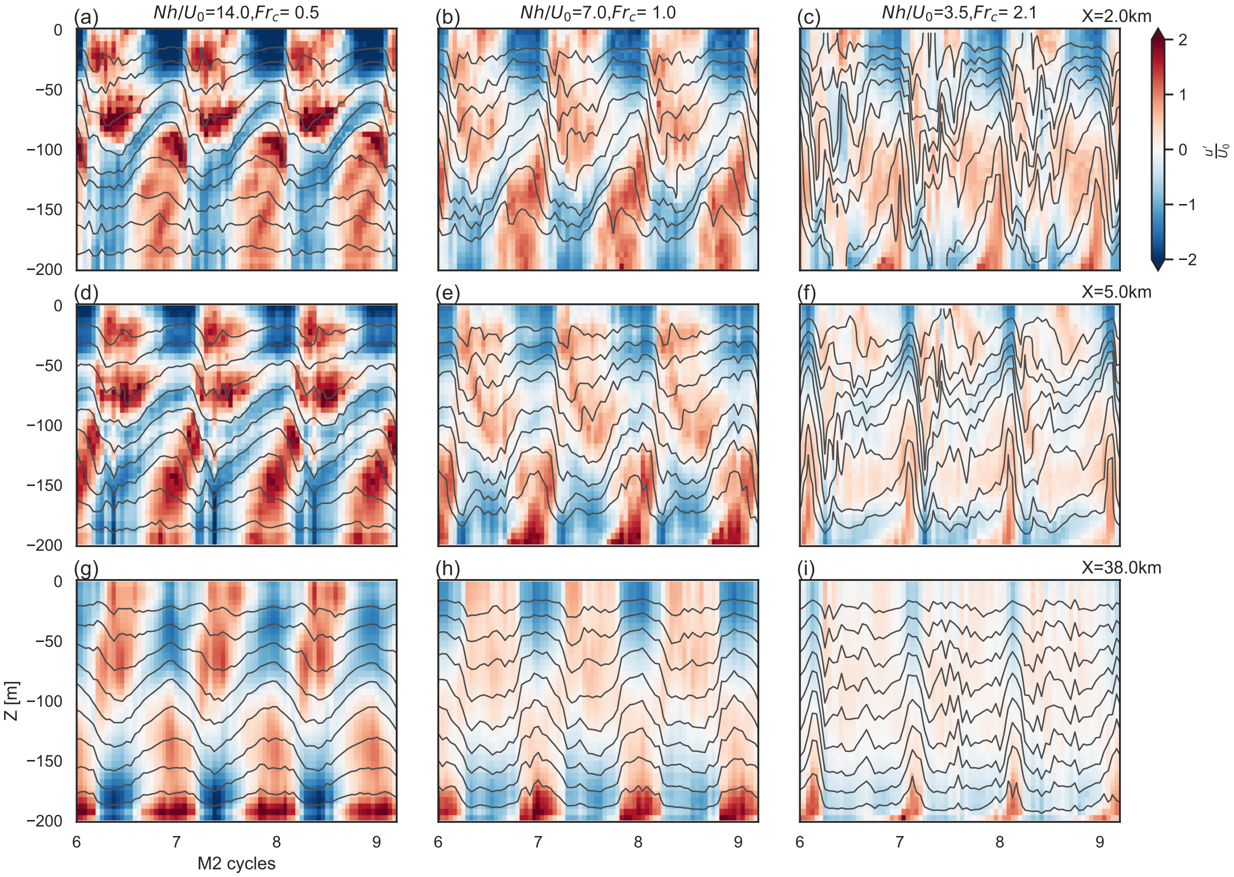

Figure 2.13: Temporal snapshots of the baroclinic flow (a,d,g) $Fr_c = 0.5$, (b,e,h) $Fr_c = 1.0$ and (c,f,i) $Fr_c = 2.1$ at (a,b,c) $X = 2$ km, (d,e,f) $X = 5$ km, (g,h,i) $X = 38$ km. The simulations are based on the same setup as the previous base runs, with modifications to achieve higher spatial resolution in the far-field region. The resolution increases from $dx_{min} = 25$ m at -35 km $< X <$ 35 km, expanding by 2.37% per cell until reaching a maximum size of approximately 600 m. The perturbation with tidal frequency is shown in all cases even when $Fr_c > 1$ and far away from the sill, suggesting internal tides are still generated when $Fr_c > 1$.

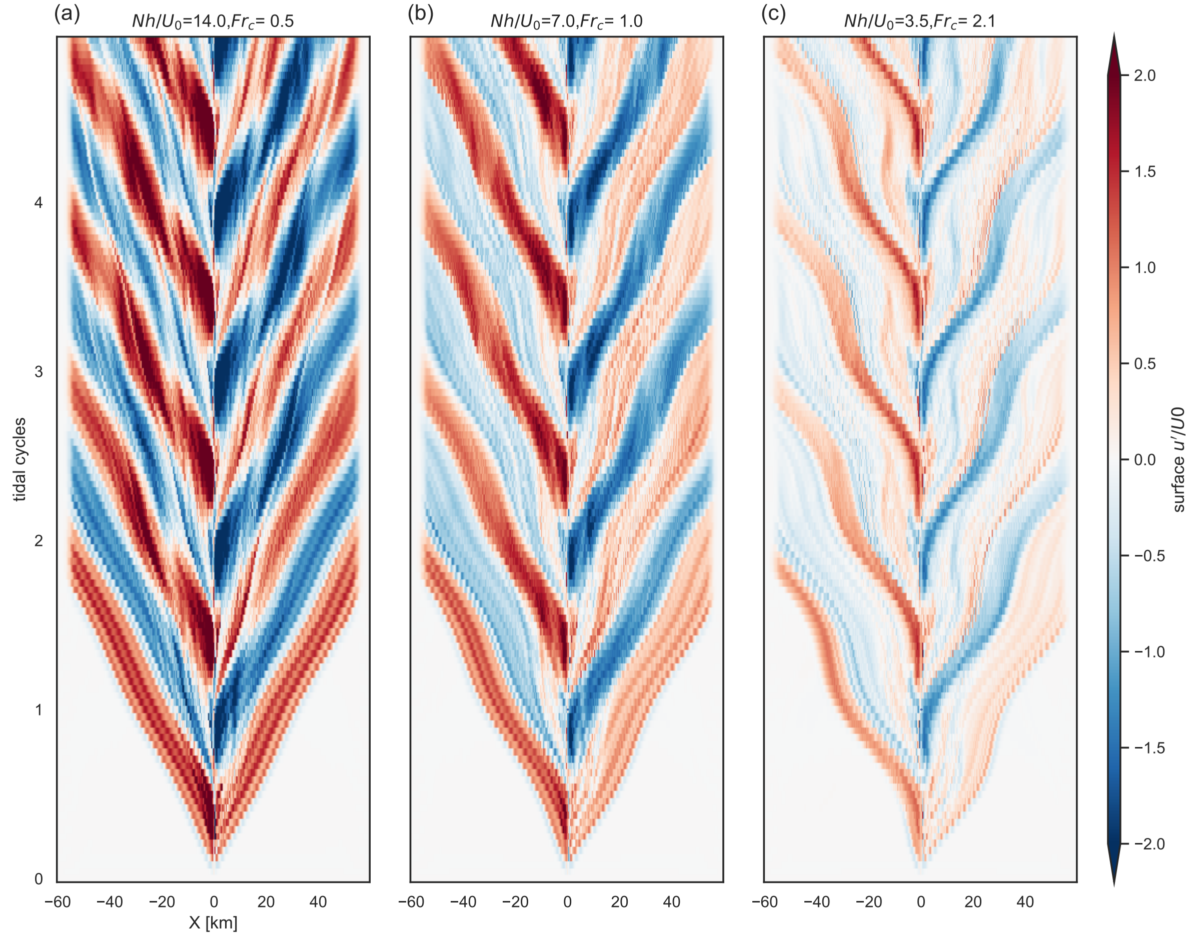

Figure 2.14: Hovmuller diagram of the surface baroclinic flow (a) $Fr_c = 0.5$, (b) $Fr_c = 1.0$ and (c) $Fr_c = 2.1$. The simulations are based on the same setup as the previous base runs, with modifications to achieve higher spatial resolution in the far-field region. The resolution increases from $dx_{min} = 25$ m at -35 km $< X <$ 35 km, expanding by 2.37% per cell until reaching a maximum size of approximately 600 m. Phase speeds become more non-constant and phase differences between off-ridge and on-ridge become more obvious as Fr increases from panels a-c.

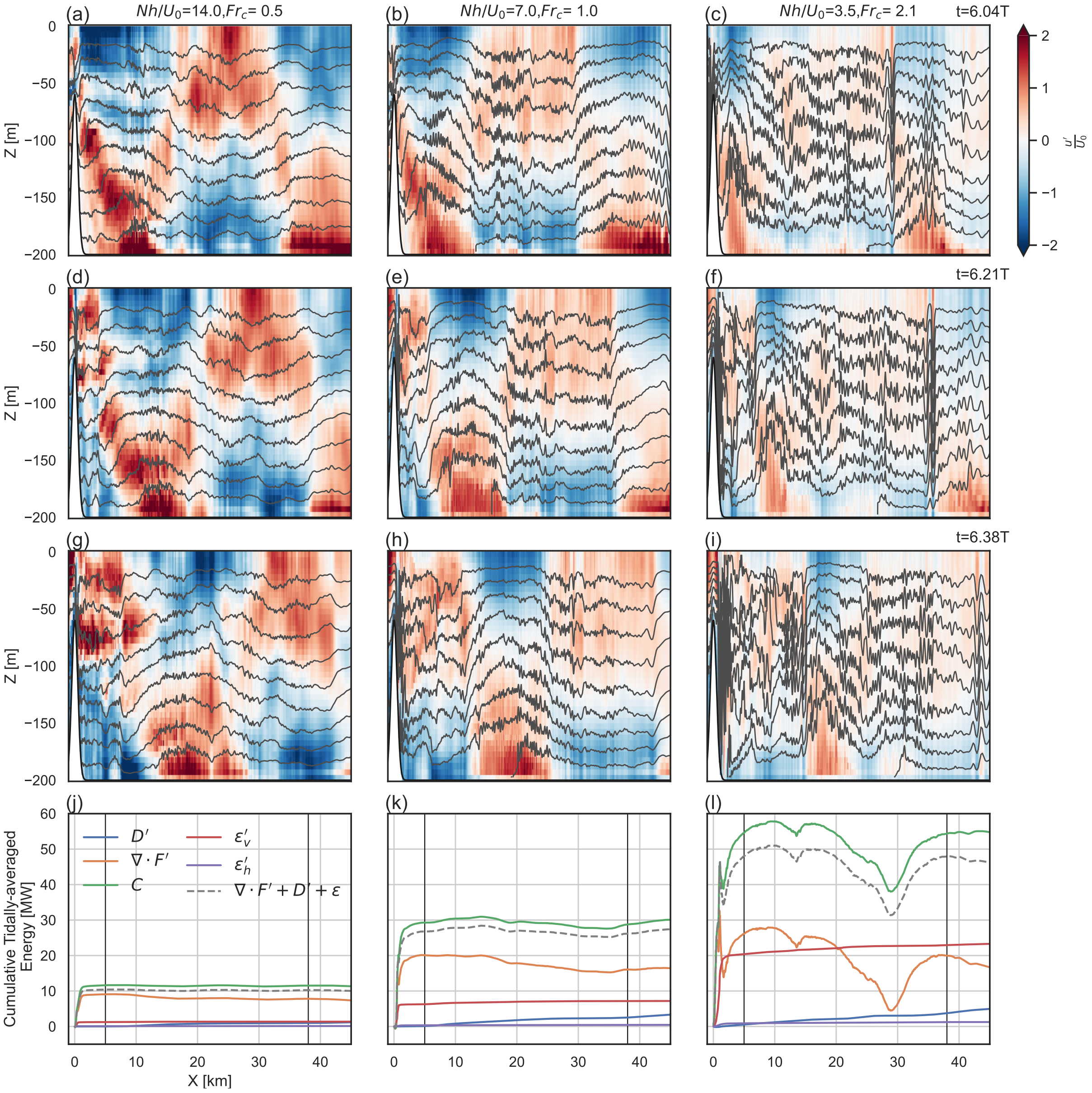

Figure 2.15: Snapshots of the baroclinic flow (a,d,g) $Fr_c = 0.5$, (b,e,h) $Fr_c = 1.0$ and (c,f,i) $Fr_c = 2.1$ at (a,b,c) t=6.04T, (d,e,f) t=6.21T, (g,h,i) t=6.38 T. Tidally-averaged cumulative energy budgets for (j) $Fr_c = 0.5$, (k) $Fr_c = 1.0$ and (l) $Fr_c = 2.1$ with colors representing different energy components as in Figure 2.5. Vertical lines are the reference position for calculate energy budgets in Table 2.2. Nonlinearity significantly increases as $Fr_c > 1$, characterised by more diffusive tidal beam and pronounced undulations in the isopycnals. The tidally-averaged baroclinic energy flux (orange curves in (l)) still shows approximately 37% radiating away at 38 km (Table 2.2), indicative of a notable waves propagating even at this distance when $Fr_c \sim 2$.

2.5.3 Concluding remarks

Knife-edge theory provides predictions for tidal conversion on supercritical slopes that are consistent with our simulations at small flow velocities. The validity of the knife-edge solution has been discussed under the condition $Nh/U \gg \pi$ when $f \ll \omega$ (Llewellyn Smith and Young, 2003). These predictions follows a power law that exhibits a quadratic relationship with U_0 and a linear relationship with h and N. However, as flow velocities increase beyond $Fr_c = U_c/c_1 > 1$, a deviation from this quadratic scaling is observed — a saturation of energy conversion. In our simulations, this deviation begins at different Nh/U_0 values depending on the ridge height (Figure 2.7b): for h=140 m, the deviation occurs when Nh/U_0 drops below 10, while for h=70 m, it starts when Nh/U_0 is below 2. This suggests that Fr_c is a more consistent indicator of when the knife-edge model starts to break down.

Our findings are in line with two-layer model of Arneborg et al. (2017), which shows a reduction in normalized conversion as Fr_c approaches 1 (their Figure 9 and 10), similar to the curves in our Figure 2.6d. Both studies use barotropic tidal amplitude as the control variable, and both indicate that tidal conversion growth slows as Fr_c approaches 1. This bending trend, noted but not deeply analyzed by Arneborg et al. (2017), is what we interpret as conversion saturation. The fact that the two-layer flow computations also suggest such saturation indicates this saturation may be intrinsic to flows with $Fr_c > 1$.

We present evidence that there exists a regime between crest-controlled flow ($Fr_c = 1$ at the crest) and fully supercritical flow ($Fr = U_0/c_1 > 1$ everywhere) where energy continues to be transferred from barotropic to baroclinic motion, albeit at a diminishing rate. This transfer may persist until the flow becomes fully supercritical, at which point a reversion to predominantly barotropic motion is expected. However, the behavior of the system under fully supercritical conditions lies beyond the scope of our study.

As tidal forcing increases in the tidal non-linear lee wave regime ($Nh/U_0 \gg 1$), the scaling relationships between energy conversion and turbulent dissipation must reconcile; otherwise, dissipation, scaling with U_0^3 , would exceed conversion, scaling with U_0^2, which is physically unreasonable. This indicates that a new scaling relationship or regime must emerge to maintain physical consistency at higher forcing before the system returns to the linear regime ($Nh/U_0 < 1$). This study delineates the limit of that regime, providing a framework that can guide future research in tidal energy dynamics.

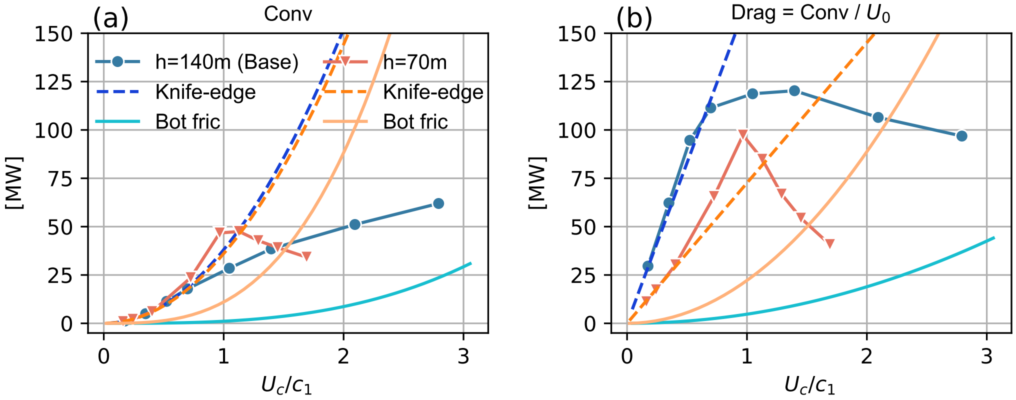

Figure 2.16: (a) Conversion and (b) drag are the function of U_c/c_1. Blues curves are the energy and drag of $h = 140$ m and oranges are $h = 70$ m. Solid curves with markers are the our simulation results, dash curves are knife-edge model and solid curves are the quadratic drag $C_d u^2$ and dissipation $C_d u^3$ due to bottom friction.

Due to the requirement for wave drag parameterization in forward, global, barotropic tide models, current models primarily utilize a linear topographic wave drag parameterization of U, and h and N within a tensor C for representing dissipative forces arising from tidal conversion (Buijsman et al., 2015; Griffiths and Peltier, 2009; Green and Nycander, 2013). Accordingly, the relationship between energy conversion and U is quadratic. There is a need for improvement, especially in cases involving supercritical slopes, shelf and coastal regions (Buijsman et al., 2015; Stammer et al., 2014; Sulzbach et al., 2021), where the relative errors may reach 16% (Stammer et al., 2014). Prior research has concentrated on tuning the C tensor, often leaving the linear U component unadjusted. As an example, Green and Nycander (2013) introduced a threshold for the C tensor as a means of mitigating errors. Our study reveals that when $Fr_c > 1$, the conversion reaches saturation. For higher ridges, it approaches nearly linearity (blue circle marker curves, Figure 2.16a), while for lower ridges, it approximates a constant value (orange triangle marker curves, Figure 2.16a). Drag (conversion divided by U_0) for higher ridges remains about constant (blue circle marker curves, Figure 2.16b), whereas for lower ridges, it follows nearly power-law decay with an exponent of -1 (orange triangle marker curves, Figure 2.16b). If tidal forcing continues to increase, bottom friction quadratic drag (solid curves, Figure 2.16)) can take over at $Fr_c = 1.5$ for $h = 70$ m, and at $Fr_c \sim 4$ for $h = 140$ m. In summary, from $Fr_c < 1$, linear wave drag is effective; from $Fr_c > 1$ up to a certain threshold dependent on ridge heights, wave drag should transition to a power-law decay to U_0 or no dependence to U_0; and when $Fr_c \gg 1$, bottom friction quadratic drag becomes dominant. This suggests a method for improving wave drag parameterization, at least in shallow water, by introducing a threshold for U where $Fr_c > 1$, deviating from a linear wave drag.

While our study offers important insights into tidal conversion and saturation for $Fr_c > 1$ flow, it is essential to acknowledge the limitations due to the idealized setup of our model. First, our simulations are two-dimensional, and previous studies have shown that three-dimensional variations in topography can reduce internal wave generation in the open ocean (Nikurashin et al., 2014). Second, we do not include rotation or atmospheric forcing, both of which can be important for generating near-inertial waves (Alford et al., 2016), whose non-linear interaction with internal tides can be significant in coastal regions (Xing and Davies, 2002). However, we note that while inertial waves can be resonantly generated in idealized two-dimensional simulations with rotation (Nikurashin and Ferrari, 2010; Zemskova and Grisouard, 2021), the fjord-like geometry in our study would not permit the amplification of such waves. Finally, by using only a single tidal constituent, we may have limited the potential interactions between different tidal components that could lead to energy transfer near the topographic features (Robertson, 2011). These factors could be addressed in future studies.

2.6 Appendix

2.6.1 Validation of Two-dimensional Simulations

In the three-dimensional simulations, all settings mirror those of the two-dimensional experiments, with the exception of the y-direction resolution ($dy = 25$ m, $ny = 120$), the Coriolis parameter $f = 10^{-4}$ s $^{-1}$ corresponds to a latitude of approximately 50^o, and hydrostatic mode. There is a significant degree of similarity between the two-dimensional and three-dimensional models, particularly with regard to tidal conversion and radiation. Although the two-dimensional simulations exhibit more vertical dissipation since there is no extensive horizontal dissipation, the combined vertical and horizontal dissipations in both dimensions are comparable. In spite of the visual differences on plots, the alignment in bottom friction is supported by its negligible magnitude.

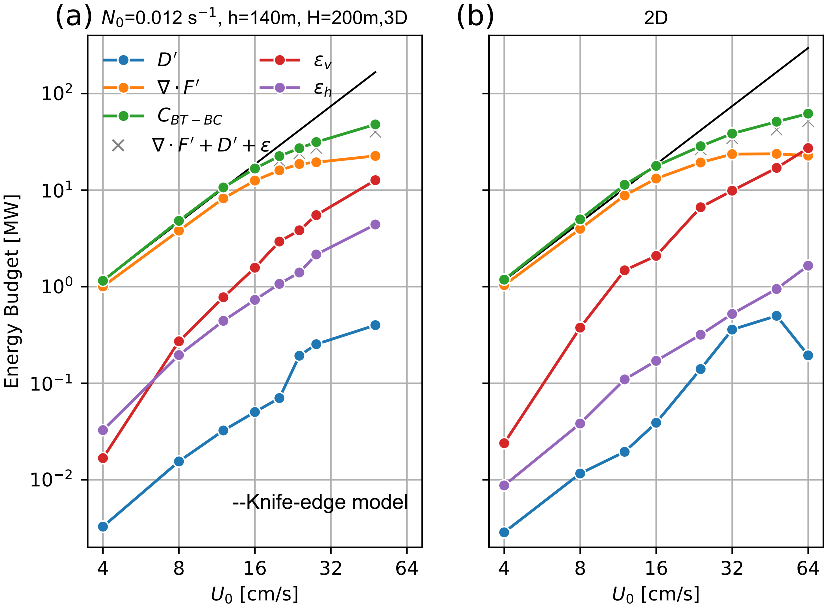

Figure 2.17: Baroclinic energy budgets of the base run with $N_0 = 0.012\,\mathrm{s}^{-1}$, $h = 140$ m and $H = 200$ m, with colors representing different energy components as in Figure 2.5, from (a) 3D simulations and (b) 2D simulations, which is the same with Figure 2.5a.

2.6.2 Baroclinic Energy Budgets over all 2D simulations

This appendix provides an overview of the baroclinic energy budget from our suite of experiments. The upper panels display a series of experiments with varying ridge heights compared to the base run, while the lower panels depict variations in stratification relative to the base run. Each subplot encapsulates the detailed energetics corresponding to varying tidal forcing U_0 in each experiment. Notably, a saturation of energy conversion is observed consistently throughout all experiments.

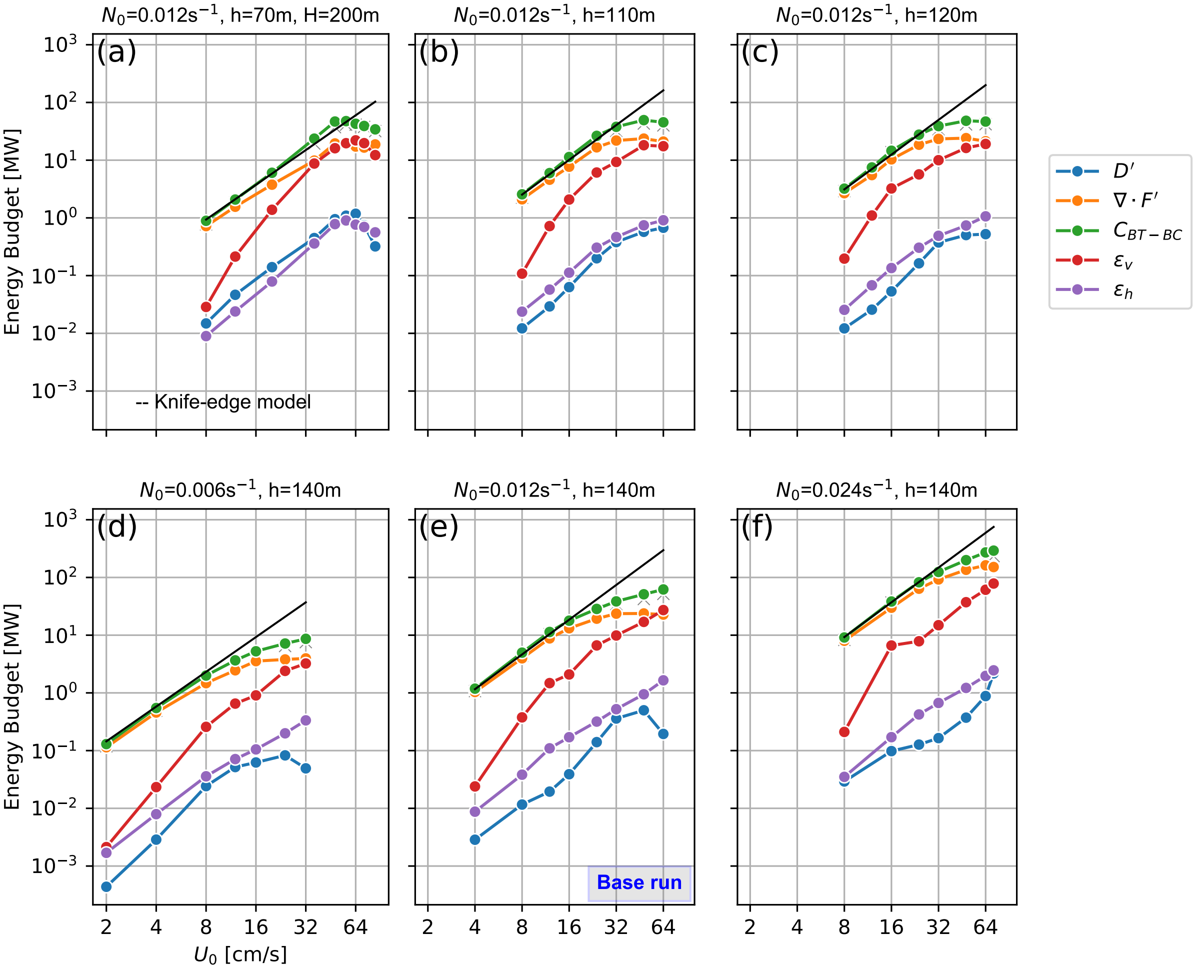

Figure 2.18: Baroclinic energy budgets for the base run with (e) $N_0 = 0.012$ s^{-1} and $h = 140$ m and a series of experiments changing h, where (a) $h = 70$ m, (b) $h = 110$ m, (c) $h = 120$ m; and a series of experiments changing N_0, where (d) $N_0 = 0.006$ s^{-1}, and (f) $N_0 = 0.024$ s^{-1}. The colors indicating different energy components are the same as those used in Figure 2.5. Knife-edge model for each experiment are shown in black lines.

Chapter 3

The Role of Wake Vortices in Modulating Tidal Energy Balance in Stratified Flows over Headlands and Adjacent Sills

Wake-induced mixing behind three-dimensional obstacles, involving both wake vortices and internal waves, is a critical sub-grid process in ocean models due to its significant contribution to form drag and local dissipation. This study examines the role of headland-generated wake vortices in internal tide dynamics over a supercritical sill (with the slope steeper than internal tidal beam) in a 3D stratified tidal channel (depth $H = 200$ m, width $L = 3$ km) driven by an M2 tide. In this setup, $O(0.1) < Ro = U_0/fD < O(1)$ and $Fr = U/Nh \ll 1$, with U_0 as the current magnitude, f as the Coriolis frequency, N as the buoyancy frequency, D as the headland width, and h as the sill height. Previous research has mainly examined internal tides and wake vortices independently. Our study isolates the vortex component by comparing the dynamics of a setup with both ridges and headlands (*R+H*) to one with only ridges (*only R*). We show that wake vortices modifies lee wave structures and disrupts approach-controlled flow. Dipole vortices form during both flood and ebb tides behind the headlands, each persisting only until the next vortex of the same phase forms and advects, giving them a life cycle of less than or approximately one tidal cycle. These vortices cause additional tidal energy loss, beyond that used for internal tide generation. This extra energy dissipates largely within the vortices' advection distance over their life cycle, likely due to shear instabilities, as the vortices are situated in vertical shear zones. Meanwhile, the radiation of internal tides remained unaffected by the generation and dissipation of wake vortices, likely due to the dominance of mode-1 internal tides, which have longer wavelengths and are less prone to breaking. This result held true across different tidal forcings and headland shapes, where the additional energy loss due to the headland could be estimated using a simple bluff body law, with the velocity enhanced by ridge-constricted flow $U_r = U_0 \frac{H}{H-h}$. This finding has important implications for sub-grid mixing parameterization of wake-induced turbulence in ocean models.

3.1 Introduction

Real underwater topography is typically three-dimensional, leading to cross-flow velocities that significantly influence the overall dynamics of ocean flows, transport, and mixing (Chang et al., 2019; Farmer et al., 2002; Geyer, 1993; Inoue et al., 2024; Klymak and Gregg, 2004; MacKinnon et al., 2019; Pawlak et al., 2003b). Cross-flow velocities can involve both horizontal and vertical directions, when the topography involves both direction of variations. Specifically, sharp horizontal variations often lead to the formation of lateral lee vortices due to flow separation, while vertical variations can generate internal gravity waves (Geyer and Signell, 1990; Johnston et al., 2019; Klymak and Gregg, 2001; McCabe et al., 2006; MacCready and Pawlak, 2001; Perfect et al., 2020a,b; Warner et al., 2013). In this study, we will focus on the dynamics and tidal energy balance when both wake vortices driven by headlands and internal tides generated by underwater sills coexist.

Before considering the effects of wake-induced mixing, it is essential to first understand internal tides, particularly regarding their generation, local dissipation, and energy radiation patterns. Internal tides are generated as tidal flows interact with underwater topographic features, forming internal waves that draw energy from the tides. The energy conversion process can be predicted by established theories (Bell, 1975; Llewellyn Smith and Young, 2002, 2003; St. Laurent et al., 2003), which show that the converted energy is proportional to the square of the tidal current speed (U_0^2). However, our previous study revealed that this conversion reaches saturation—failing to grow further with U_0^2—when the flow speed relative to mode-1 internal wave phase speed (U_r/c_1) exceeds unity. This saturation phenomenon, associated with the onset of approach-controlled flow when $U_r/c_1 > 1$, is particularly relevant in shallow coastal and fjord regions, where tidal currents are strong. Note that $U_r = U_0 \frac{H}{H-h}$ represents the flow accelerated due to the ridge. In Chapter 2, this was denoted as U_c; however, here it is referred to as U_r because this chapter incorporates the presence of both a headland and a ridge, where the flow at the crest is simultaneously constricted by both features.

Once the energy is converted, a portion of conversion energy dissipates near the generation site, contributing to local dissipation, while the remaining energy radiates outward. The proportion of energy dissipated locally varies depending on the characteristics of the topography. For sharp and steep features, such as the Hawaiian Ridge, the majority of tidal energy is converted to low-mode waves, with only about 15% lost to local dissipation (Klymak et al., 2006). Conversely, in areas with flatter but widespread roughness, such as the Brazil Basin, approximately 30% of the tidal energy contributes to local dissipation (St. Laurent and Garrett, 2002), likely resulting from nonlinear wave-wave interactions (Nikurashin and Legg, 2011).

While internal waves have been the primary focus in ocean mixing studies (Melet et al., 2013a, 2014) especially confined to two-dimensional ridges (St. Laurent and Garrett, 2002; Llewellyn Smith and Young, 2003; Klymak et al., 2010a), wake-induced mixing behind three-dimensional obstacles, which may involve both wake vortices and internal waves, is an important sub-grid process due to its significant contribution to form drag and local dissipation and thus needs accurate parameterization in models. For instance, at Three Tree Point (TTP) in Puget Sound, both tilted headland vortices and internal waves have been observed, with form drag caused by these phenomena being 50 times greater than frictional drag over a flat bottom (Edwards et al., 2004; Warner et al., 2013; Warner and MacCready, 2014). In Palau, wake vortices on the North Equatorial Current result in 10 times more energy loss compared to lee wave drag or bottom drag (Johnston et al., 2019). In Knight Inlet, local dissipation due to wake vorices exceeds that caused by internal motions such as hydraulic jumps and breaking internal waves (Klymak and Gregg, 2004).

An important question is whether the presence of vortices not only increases local dissipation but also affects the amount of energy radiating away with internal waves from the generation site. In Knight Inlet, although the local energy dissipation due to vortices is significant, the total energy dissipated locally is still less than that radiated away by internal tides, approximately one-third compared to two-thirds (Klymak and Gregg, 2004). However, recent studies on seamounts suggest that wake-related dissipation can surpass the energy carried away by radiating internal waves (Perfect et al., 2020a; Puthan et al., 2022a). If significant energy radiation still occurs, identifying where this energy dissipates remains an outstanding question.

Stratified oceanic wake dynamics under varying flow conditions with different wake behaviors are quantified by parameters, Froude number ($Fr = U_0/Nh$) and Rossby number ($Ro = U_0/fD$), where f is the Coriolis parameter, U_0 is the undisturbed current magnitude, N is the stratification, and D is the horizontal scale of the obstacle (Perfect et al., 2018, 2020a,b; Srinivasan et al., 2019). The Froude number is the ratio of inertial to buoyancy forces while the Rossby number is the ratio of inertial to Coriolis forces. For $Fr < 1$ and $Ro < 1$, fluid below a critical depth can pass a topographic feature, allowing vortex shedding (Perfect et al., 2018, 2020a,b). For $Fr > 1$ and $Ro < 1$, a Taylor cap or steady wake forms under geostrophic balance (Srinivasan et al., 2019). For $Fr < 1$ and $Ro > 1$, a lee wake, vortex shedding, lee waves, and hydraulic control can coexist (Puthan et al., 2020). We will explore regimes similar to those studied by Puthan et al. (2020); however, while their focus was on wake dynamics under varying tidal frequencies and mean flow (tidal modulated flow), our research examines wake dynamics under single pure tides, specifically investigating the impact of wake vortices on tidal energy balance.

Pure tide studies on oceanic wakes (Black and Gay, 1987; Pingree and Maddock, 1979; Signell and Geyer, 1991; Wolanski et al., 1984, 1996) mainly focused on the formation of transient vortices, often in very shallow and homogeneous waters, where bottom friction plays a significant role in vortex development. The Keulegan–Carpenter number ($Kc = U_0/\omega D$) is the ratio of advection to the local acceleration term, where ω is angle frequency of tides. As Kc increases, advection becomes more dominant, eventually leading to flow separation. Alternatively, Kc can be viewed as the ratio of tidal excursion to the headland length.

The life cycle of vortices potentially impacts mixing processes (Pawlak et al., 2003a,b). Vortices may act as barriers to particle transport within their cores (Provenzale, 1999), or multiple vortices may interact and change the residual flow direction (Pawlak and MacCready, 2002). For dipole vortices, they can self-advect and have been studied in the context of "tidal flushing" between straits or into inlets. Strouhal number ($St = f_s D/U_0$) is traditionally used to describe the natural shedding frequency (f_s) of vortices in steady flows, such as Kármán vortex streets. In the context of tidal flushing, St is defined as $St = D/U_0 T$, where T is the tidal period, representing the ratio of the headland length to tidal excursion, which is the inverse of the Kc as defined eariler. When $St < 0.13$, the tidal jet detaches before the tides change direction, allowing successive vortices to interact and potentially extend their life cycle beyond one tidal period (Vouriot et al., 2018; Wells and van Heijst, 2003). At TTP, the drift-tracked vorticity decay times indicated a vortex life cycle shorter than one tidal period (Pawlak et al., 2003a,b). This suggests that the conditions for vortex detachment were likely not met, although no explicit St was estimated.

The dissipation mechanisms that lead to vortex decay include several key processes. Centrifugal instabilities occur at high Re and Ro numbers, relaxing high vorticity values to near-inertial levels (Dong et al., 2007; Srinivasan et al., 2019). Baroclinic instabilities can arise as the Burger number ($Bu = (\frac{Ro}{Fr})^2$) decreases, where Bu quantifies the ratio of rotational effects to stratification effects. A low Bu indicates the vortex size approaches the baroclinic deformation radius, leading to vortex decay (Dong et al., 2007). Shear instabilities, such as those observed in tilted vortices at Palau, also contribute to vortex decay (Wynne-Cattanach et al., 2022). Elliptic instabilities, driven by a strong strain field, can distort and weaken vortices (Canals and Pawlak, 2011), while zigzag instabilities affect vortex pairs or arrays, particularly when the Froude number is much less than 1 (Billant and Chomaz, 2000). Additionally, tilted vortices maintained by baroclinic effects may decay when the alignment of density and pressure fields diminishes as tidal forces weaken (Canals et al., 2009; Pawlak et al., 2003b).

Our research is motivated by observations in Knight Inlet, where a narrow channel with contractions in the north and south walls coincides with an underwater sill with a width of 2 km and a height of 140 m. Knight Inlet is a stratified tidal estuary with an average depth of 295 m and a width of 3 km (Farmer and Freeland, 1983). Observations have shown three-dimensional recirculating dipole vortices in the lee of the contraction (Klymak and Gregg, 2001) and nonlinear lee waves behind the sill (Farmer and Armi, 1999b). Local dissipation due to wake vortices was estimated at 2 TW, surpassing the 1 TW dissipation from breaking internal tides and 1 TW from bottom friction (Klymak and Gregg, 2004). However, the estimated local dissipation was found to be lower than the calculated Bernoulli drop, suggesting a potential underestimation of total dissipation. These estimates were derived from limited measurements (one along-channel transect and two cross-channel transects), highlighting the need for more comprehensive three-dimensional modeling to better estimate the individual contributions of internal tides and wake vortices to the total energy dissipation.

Therefore, to isolate the effects of wake vortices, we will include a control experiment with only the ridge (to generate only internal tides) and compare it to experiments with both the ridge and headland present, allowing us to address the aforementioned questions (Section 3.2). We will examine the spatial and temporal fields where internal tides and wake vortices are co-generated, identifying the distinct contributions of vortices to the overall flow dynamics (Section 3.3). This includes analyzing their life cycle and dissipation mechanisms. Our broader goal is to understand the individual roles of internal tides and wake vortices in the tidal energy balance and to develop a power law parameterization for these contributions (Section 3.4). Additionally, we will test the effects of varying tidal forcing magnitudes and different aspect ratios of headlands on these dynamics. The regime we consider here is characterized by weak rotation and strong stratification, with Fr ranging from 0.024 to 0.286, Ro from 0.22 to 2.68, Kc from 0.01 to 1.92, St from 0.08 to 20 and Bu from 0.22 to 88.

3.2 Method

3.2.1 Model configuration

To investigate the concurrent generation of internal tides and wake vortices, the three-dimensional MITgcm with an online barotropic–baroclinic energy decomposition (Kang and Fringer, 2012; Klymak et al., 2016) is employed to simulate the stratified tidal flows interacting with idealized topography, including both Gaussian-shaped sills and parabolic headlands (Figure 3.1). The chosen dimensions and oceanographic parameters are loosely based on the sill in the Knight Inlet, with the headlands inspired by the features of Hoeya Sound and Prominent Point. We use a Cartesian coordinate system with both the x and y axes centered at the middle of the sills in an 120-km-long, 3-km-wide channel. Gaussian-shaped sills are defined by $h = h_0 \exp \frac{-x^2}{L^2}$, where h_0 is the maximum height of the sill, and L represents the length scale of the sill. The parabolic headlands have the cross-channel extent given by $\chi(x) = b - \left(\frac{x}{a}\right)^2$. where b is the maximum extent at the centerline ($x = 0$), and a determines the width of the headland across the channel. The headland extends laterally from the centerline up to the points where the extent drops to zero $\chi(x) = 0$, providing the boundaries of the headland: $x = \pm a\sqrt{b}$, thus total cross-channel width of each headland is $D = 2a\sqrt{b}$. Different values of the parameters b and a are used to define the headland geometries, resulting in various along-channel widths ranging from approximately 1.78 km to 35 km (See Table Table 3.1). The aspect ratio $\lambda = \frac{b}{D}$ ranges from 0.014 to 0.28. The sharpest headland ($b' = 1.6b$), accelerates the flow the most, with the narrowest constricted width of 3-1.6=1.4 km, compared to the base headland, which has a constricted width of 3-1=2 km, while the total channel width remains constant at 3 km.

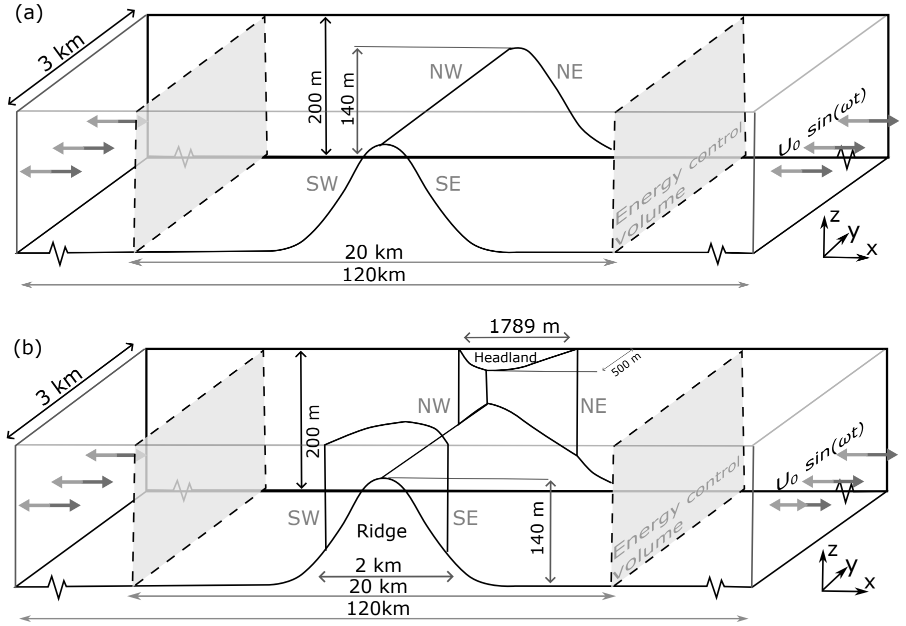

Figure 3.1: Model configurations for (a) *only R* and (b) *R+H* scenario. (a) shows the 2D Gaussian ridge topography used in the *only R* scenario, while (b) depicts the *R+H* scenario, which includes additional headlands on the north and south sides of the ridge. Both setups are within a 120 km long, 3 km wide channel. The integrated volume range of energy budget and the forcings are also indicated. While the experiments include the different widths and extents of the headlands (see Table 3.1), this figure only illustrates the scales in base experiment.

The simulations are conducted on an f-plane with a Coriolis parameter $f = 10^{-4}s^{-1}$, representative of mid-latitude oceanic conditions. The stratification is defined by a buoyancy frequency $N = 1.2 \times 10^{-2}$ rad s^{-1}. The model uses a horizontal grid resolution of 25 m in the central portion of the domain, with grid cells expanding by 2.7% per cell beyond the central region to a maximum size of 1225 m. The vertical resolution is fixed at 5 m, resulting in a total of 40 vertical grid cells.

To simulate tidal currents and density variations, we applied nudging boundary conditions at the western and eastern boundaries of the model domain. A sponge layer with varying relaxation timescales was implemented to minimize the reflection

Runs	a [m]	b [m]	D [km]	$\lambda(=\frac{b}{D})$	H [m]	h [m]	N [rad s^{-1}]	U_0 [cm s^{-1}]	$Ro(=U_0/fD)$	$Fr(=U_0/Nh)$	$Kc(=U_0/\omega D)$	$St(=D/U_0T)$	$Bu(=(\frac{Ro}{Fr}^2)$
R+H (base run)	40	500	1.789	0.280	200	140	0.012	4-48	0.22-2.68	0.024-0.286	0.16-1.92	1-0.083	88.20
R+H 1.28b	35.35	640	1.789	0.320	200	140	0.012	4-32	0.22-1.79	0.024-0.190	0.16-1.28	1-0.125	88.23
R+H 1.6b	31.62	800	1.789	0.354	200	140	0.012	4-24	0.22-1.34	0.024-0.143	0.16-0.96	1-0.167	88.22
R+H 1.4a	56	500	2.503	0.200	200	140	0.012	4-32	0.16-1.28	0.024-0.190	0.11-0.91	1.40-0.175	45.00
R+H 4a	160	500	7.155	0.070	200	140	0.012	4-36	0.06-0.50	0.024-0.214	0.04-0.36	4.01-0.445	5.51
R+H 8a	320	500	14.311	0.035	200	140	0.012	4-32	0.03-0.22	0.024-0.190	0.02-0.16	8.01-1.002	1.38
R+H 20a	800	500	35.777	0.014	200	140	0.012	4-32	0.01-0.09	0.024-0.19	0.01-0.06	20.04-2.505	0.22
R+H h070	40	500	1.789	0.280	200	70	0.012	24-64	1.34-3.58	0.286-0.762	0.96-2.56	0.17-0.063	22.05
only R h140	-	-	-	-	200	140	0.012	4-64	-	0.024-0.286	-	-	-
only R h070	-	-	-	-	200	70	0.012	24-64	-	0.095-0.667	-	-	-

Table 3.1: Summary of parameters for simulations including both *Ridges+Headlands* (*R+H*) and *Only Ridges* (*only R*) for comparison. The nondimensional numbers Ro (Rossby number), Fr (Froude number), Kc (Keulegan–Carpenter number), St (Strouhal number), and Bu (Burger number) are also provided for *R+H* runs.

of internal waves: 100 seconds at the outer edge and 1000 seconds at the inner edge. The tidal forcing was introduced using a sinusoidal function corresponding to the M2 tidal period (T = 44,640 s, so $\omega = \frac{2\pi}{T} \approx 1.4 \times 10^{-4}$ s^{-1}) with magnitudes (U_0) ranging from 4 to 80 cm s^{-1} (Table 3.1). The tidal velocity follows $U = U_0 \sin(\omega t)$, where $t = jT$ (integer j) represents slack tide. Flood tide occurs between $t = jT$ and $t = (j + 0.5)T$, with flood peak tide at $t = (j + 0.25)T$. Similarly, ebb tide occurs between $t = (j + 0.5)T$ and $t = (j + 1)T$, with ebb peak tide at $t = (j + 0.75)T$. The walls and bottom in the model domain were set with free-slip conditions. Additional bottom friction was incorporated as quadratic bottom drag (with $C_d = 1 \times 10^{-3}$). The simulations generally employed a time step (Δt) of 1.24 seconds to ensure compliance with the Courant-Friedrichs-Lewy (CFL) criterion ($C = u\frac{\Delta t}{\Delta x} < 1$). However, for cases with sharper headlands (1.6b and U_0 = 24cm s^{-1}), the time step had to be reduced to 0.62 seconds to maintain numerical stability and satisfy the CFL condition. The simulations were run for a duration of 12 tidal cycles.

To maintain numerical stability, viscosity ν_v and diffusivity κ_v were parameterized based on regions of density overturns (Klymak and Legg, 2010). Following the results of sensitivity tests in Chapter 2, we adopted the background horizontal viscosity and diffusivity $\kappa_h = \nu_h = 10^{-2}$, which provides a well-closed energy budget without significantly altering other terms, while vertical values were set to $\kappa_v = \nu_v = 10^{-5}$ m^2 s^{-1}. A second-order flux-limiting temperature advection scheme (tempAdvScheme = 77; see the MITgcm manual) was utilized, which introduced some numerical diffusivity and dissipation (Klymak and Legg, 2010).

The ranges of those relevant nondimensional parameters (Ro, Fr, Kc, and Bu), as summarized in Table 3.1, were selected to span a broad spectrum of realistic oceanic conditions by varying tidal forcing U_0 and spatial length of headlands.

3.2.2 Decomposition into two-dimension versus three-dimensional and barotropic versus baroclinic Components

Considering the two-dimensional nature of the ridge in our experiments (i.e., no variation in the y-direction), the internal tide generated by the tides over the ridge is expected to be two-dimensional (2D). However, with the inclusion of the Coriolis force, the internal tidal flow acquires three-dimensional (3D) components. The main contribution to the 3D flow, though, comes from the vortices generated by the headlands. Additionally, while the internal tide motion is definitively baroclinic (BC, i.e., varying in the vertical direction), our analysis later in this paper will show that the vortex motion is not purely barotropic (BT). To examine the contribution of vortices and assess the role of headlands in generating 3D flow structures, we decomposed the flow field into two categories: 2D versus 3D, and BT versus BC components.

The total velocity (u) is first separated into BT (u_{bt}) and BC (u_{bc}) components:

$$u_{bt} = \frac{\int_{-H}^{0} u\,dz}{\int_{-H}^{0} dz} \tag{3.1}$$

$$u_{bc} = u - u_{bt} \tag{3.2}$$

Here, u_{bt} represents the depth-averaged velocity, and u_{bc} represents the deviation from this average, corresponding to the baroclinic component.

The kinetic energy (KE) associated with the flow can be decomposed similarly. For the BT and BC components, the kinetic energies are:

$$\mathrm{KE}_{u_{bt}} = \frac{1}{2}u_{bt}^2 \tag{3.3}$$

$$\mathrm{KE}_{u_{bc}} = \frac{1}{2}u_{bc}^2 \tag{3.4}$$

Next, the velocity field is further decomposed into 2D (u_{2d}) and 3D (u_{3d}) components:

$$u = u_{2d} + u_{3d} \tag{3.5}$$

The 2D component u_{2d} is obtained by averaging the velocity across the channel width L:

$$u_{2d} = \frac{\int_{-\frac{L}{2}}^{\frac{L}{2}} u\,dy}{\int_{-\frac{L}{2}}^{\frac{L}{2}} dy} \tag{3.6}$$

The 3D component u_{3d} is then defined as the residual:

$$u_{3d} = u - u_{2d} \tag{3.7}$$

The kinetic energy associated with the 2D component is:

$$\mathrm{KE}_{u_{2d}} = \frac{1}{2}u_{2d}^2 \tag{3.8}$$

And for the 3D component:

$$\mathrm{KE}_{u_{3d}} = \frac{1}{2}u_{3d}^2 \tag{3.9}$$

Note that $\mathrm{KE}_{u_{2d}}$ is distinct from the $\mathrm{KE}_{2d} = \frac{\int \frac{1}{2}u^2 dy}{\int dy}$, as the former is specifically related to the 2D velocity component, whereas the latter represented a mean kinetic energy across the channel width.

Finally, the overall kinetic energy (KE) is expressed as:

$$\mathrm{KE} = \mathrm{KE}_{u_{2d}} + \mathrm{KE}_{u_{3d}} + u_{2d}u_{3d} \tag{3.10}$$

Further decomposition of the 2D component yields:

$$\mathrm{KE} = \mathrm{KE}_{u_{bc}} + \mathrm{KE}_{u_{bt}} + u_{bc}u_{bt} \tag{3.11}$$

This decomposition allows us to isolate the contributions from 2D motions and the 3D components, which are particularly relevant in the presence of headlands. By cross-comparing the results from the *R+H* experiments with those from the *only R* experiments, we can identify the role of vortex generation in modifying the overall flow and energy distribution in the system.

3.2.3 Barotropic-Baroclinic Energy Decomposition

In this study, we employ the BT and BC energy decomposition method (Kang, 2011; Klymak, 2018; Hughes and Klymak, 2019), to analyze the energy budgets and dissipation processes in our simulations. This decomposition is performed online during the simulations, allowing for real-time energy capture and analysis.

The decomposition is based on a depth-integrated, tidally-averaged energy equation. In a steady, tidally forced system, the barotropic tidal energy is either dissipated in the bottom boundary layer or converted into baroclinic energy. The vertically integrated energy budgets are described by the following equations:

$$\begin{aligned} \frac{1}{T}\Delta\overline{E_{bt}} + \nabla_H \cdot \left\langle \overline{\mathbf{F}_{bt}} \right\rangle &= -\langle\bar{C}\rangle - \langle\overline{\epsilon_{bt}} + D_{bt}\rangle \,, \\ \frac{1}{T}\Delta\overline{E_{bc}} + \nabla_H \cdot \left\langle \overline{\mathbf{F}_{bc}} \right\rangle &= \langle\bar{C}\rangle - \langle\overline{\epsilon_{bc}} + D_{bc}\rangle \,, \end{aligned} \tag{3.12}$$

where E is the tidal energy, F is the tidal energy flux, C is the conversion from BT to BC energy, ϵ is the turbulence dissipation, and D is the bottom boundary layer dissipation. BT and BC components are denoted by subscripts bt and bc, respectively. The overbars denote depth integrals $\overline{\ } = \int dz$, while the angle brackets indicate tidal averages $\langle\rangle = \frac{1}{T}\int dt$.

The conversion term C plays a central role in connecting the energy budgets of BT and BC energies:

$$\overline{C} = \overline{\rho' g W} - \overline{q_z W} + A_{h0}, \tag{3.13}$$

where ρ' represents a density perturbation, $W(z)$ is the vertical velocity, q_z is the nonhydrostatic part of the pressure, and A_{h0} is the non-linear term, expressed as:

$$A_{h0} = \rho_0 \left(u_{bt}\nabla_H \cdot \overline{\mathbf{u}_{bc,H} u_{bc}} + v_{bt}\nabla_H \cdot \overline{\mathbf{u}_{bc,H} v_{bc}} \right), \tag{3.14}$$

where the subscript H refers to the horizontal component.

Baroclinic energy, after conversion, undergoes dissipation or leaves the system as an internal wave energy flux, described by:

$$\overline{F_{bc}} = \overline{u_{bc} p_{bc}} + \overline{u E_{bc}}, \tag{3.15}$$

where the contribution is from pressure work $\overline{u_{bc} p_{bc}}$ and energy advection $\overline{u E_{bc}}$. Details can be seen in Kang (2011) Eq. (6.16).

Turbulent dissipation in vertical direction ϵ_v is obtained from the modeled vertical viscosity as

$$\epsilon_v = \rho_0 \nu_v \left(\left(\frac{\partial u}{\partial z} \right)^2 + \left(\frac{\partial v}{\partial z} \right)^2 \right), \tag{3.16}$$

and horizontal dissipation is calculated as

$$\epsilon_{bc,h} = \rho_0 \nu_H \left(\nabla_H \mathbf{u}_{bc,H} \cdot \nabla_H \mathbf{u}_{bc,H} \right). \tag{3.17}$$

3.3 Phenomenology

3.3.1 Velocity and Density Field

The flow along the current direction exhibits nonlinear trapped lee waves that are similar to those usually observed in flows over supercritical ridges (Figure 3.2 e-h). As the tide strengthens, the lee waves grow until they reach a peak (Figure 3.2 e-g), after which they collapse when the flood tide subsides. As the tides reverse (Figure 3.2 h), the remaining bore is released to the opposite side of the ridge. This evolution is akin to the typical behavior of nonlinear lee waves as oscillating flow over supercritical ridges (Klymak et al., 2012; Legg and Klymak, 2008; Winters and Armi, 2013), with the additional presence of a vertical confined strong flow trailing the lee wave (Figure 3.2 g). Near the headland, smaller lee waves are also observed, though they are less pronounced (Figure 3.2 a-d). As we will see in the vorticity plots later, these less pronounced lee waves coincide with the locations where vortices are generated.

In the cross-channel transect, the presence of the headland introduces a distinct flow structure characterized by a central jet flanked by regions of negative flow near the north and south walls of the channel (Figure 3.2 i-p). This jet forms as the tides strengthen, but it does not extend to the bottom, reaching a maximum depth of about 120 m (Figure 3.2 j,k,o). As the tidal flow weakens during the transition to flow reversal, the jet migrates towards the right-hand side wall, due to the effects of rotation (Figure 3.2 s to q and t). This shift is also accompanied by a reduced depth of jet, with tilting occurring below 100 m (Figure 3.2 p).

The last jet formed under the previous tidal direction persists and gradually dissipates after the flood tide (top view of the flow, Figure 3.2 q,r). Subsequently, the overall flow pattern becomes more symmetric around the central axis ($Y = 0$, Figure 3.2 s).

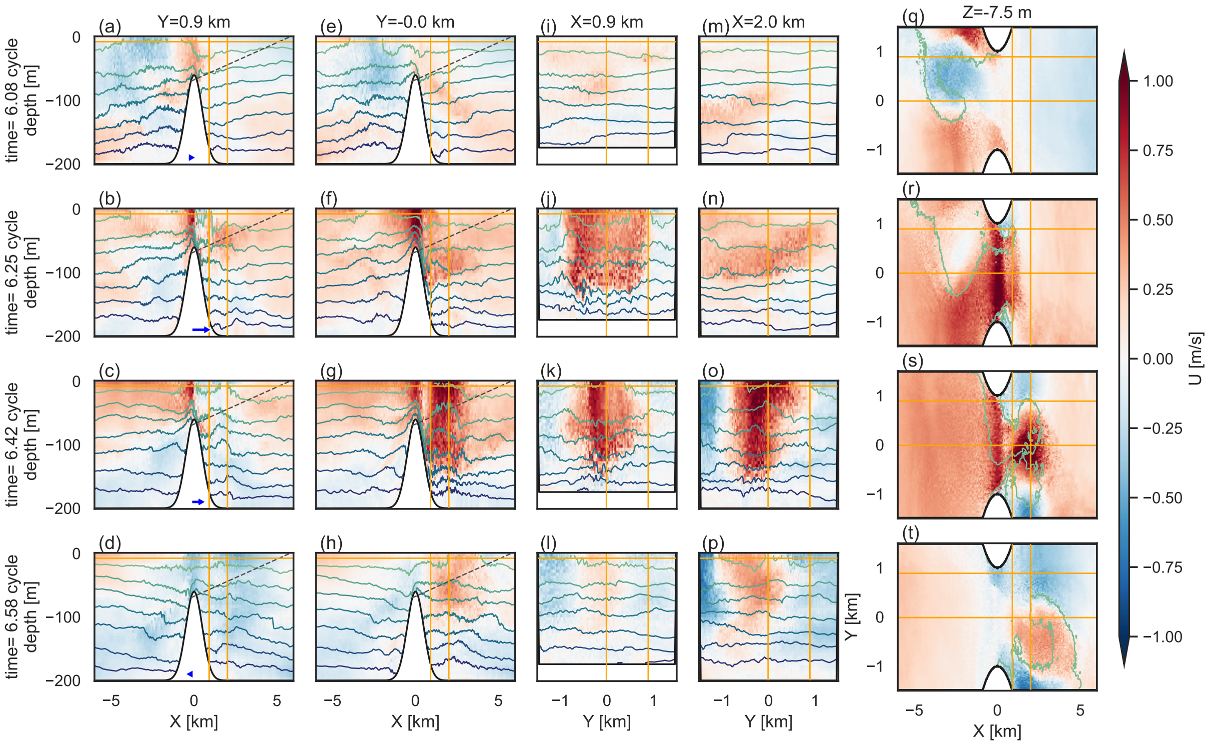

Figure 3.2: Temporal evolution of flow and density structures over a half tidal cycle where $Ro = 0.89, Fr = 0.095$. The first two columns (a-d, e-h) show along-channel transects at $Y = 0.9$ km and $Y = 0$ km, respectively. The third and fourth columns (i-l, m-p) display cross-channel transects at $X = 0.9$ km and $X = 2.0$ km. The fifth column (q-t) presents top-view snapshots at a depth of $Z = -7.5$ m. Rows correspond to specific tidal phases at 6.08, 6.25, 6.42, and 6.58 cycles, with arrows in the first column indicating tidal forcing magnitude. Velocity (U) is represented by shaded contours, while overlaid contours depict density fields, ranging from light blue to dark blue, indicates increasing density. Density contours in the contourf plot are uniformly spaced in depth, with an interval of 25 m (e.g., at depths of 2.5, 27.5, 52.5, ..., down to 177.5 m). In the top view snapshots (q-t) at 7.5 m, only the light blue isopycnal, originally at 27.5 m, is visible, indicating significant water uplift. The evolution near the ridge is akin to the typical behavior of nonlinear lee waves as oscillating flow is over supercritical ridges, with the additional presence of a vertical confined strong flow trailing the lee wave.

A distinct vertical confined strong flow trails the lee wave (Figure 3.2g,Figure 3.3c), closely resembling the flow observed in Klymak and Gregg (2001, Plate 7b) . This feature can be seen more clearly when compared to the experiment without headland (*only R*, Figure 3.3 ad,cf), as seen in both along- and cross-channel views. The vertical confined strong U flow is directed northward at $Y > 0$ and southward at $Y < 0$, though both are much weaker than the east-west flow (Figure 3.4 c,f). In the presence of headland vortices, the horizontal wavelength of the lee waves is stretched significantly, from approximately 100 m to over 1000 m ($0 < X < 1$ km, Figure 3.3 a,c). Consequently, the lee waves take a smoother, more undular form, contrasting with the sharper and steeper waves seen in the absence of vortices, where a group of isopycnals plunges almost attached to each other, forming abrupt jumps ($0 < X < 500$ m, Figure 3.3 a,b).

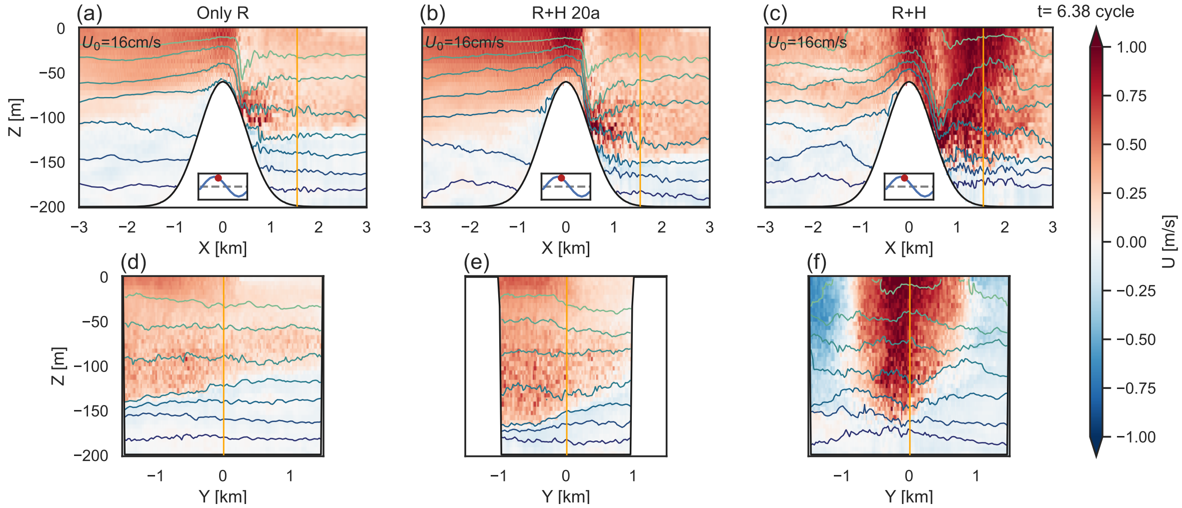

Figure 3.3: Flow and density structures 1.6 hrs after the flood peak tides ($t = 6.38$ cycles). The top row (a-c) shows along-channel transects at $Y = 0$ km, while the bottom row (d-f) presents cross-channel transects at $X = 1.5$ km. The first column (a, d) corresponds to the *only R* experiment, the second column (b, e) to the *R+H 20a* experiment, and the third column (c, f) to the *R+H* experiment. Shaded contours represent the U-velocity, with overlaid contours indicating the density fields. While isopycnal structures under wide headland scenario remain largely similar to the *only R* case, and both resemble the approach-controlled flow structure, in the presence of headland vortices, the horizontal wavelength of the lee waves is stretched significantly.

Above the ridge crest, the flow is resembling supercritical symmetric structure more than *only R* case (-200 m $< X <$ 200 m, Figure 3.3 a,c), although it is not fully supercritical. However, it is unclear whether this is solely due to the faster flow above the ridge, caused by the headland constriction. In another experiment with a much wider headland (*R+H 20a*, Figure 3.3 b), with the same level of being constricted by the extent of headland (b), but with no flow separation or vortex formation, the isopycnal structures under wide headland scenario remain largely similar to the *only R* case (Figure 3.3 a,b), and both resemble the approach-controlled flow structure reported in our prior study. This suggests that the flow above the ridge leaning more to supercritical flow in the R+H case may not be solely due to the headland constriction. Instead, it might be influenced by upstream residual vortices, which are visible in the subsequent vorticity plots, and cause isopycnal perturbations ($-3 < X < -1$ km, Figure 3.3 c).

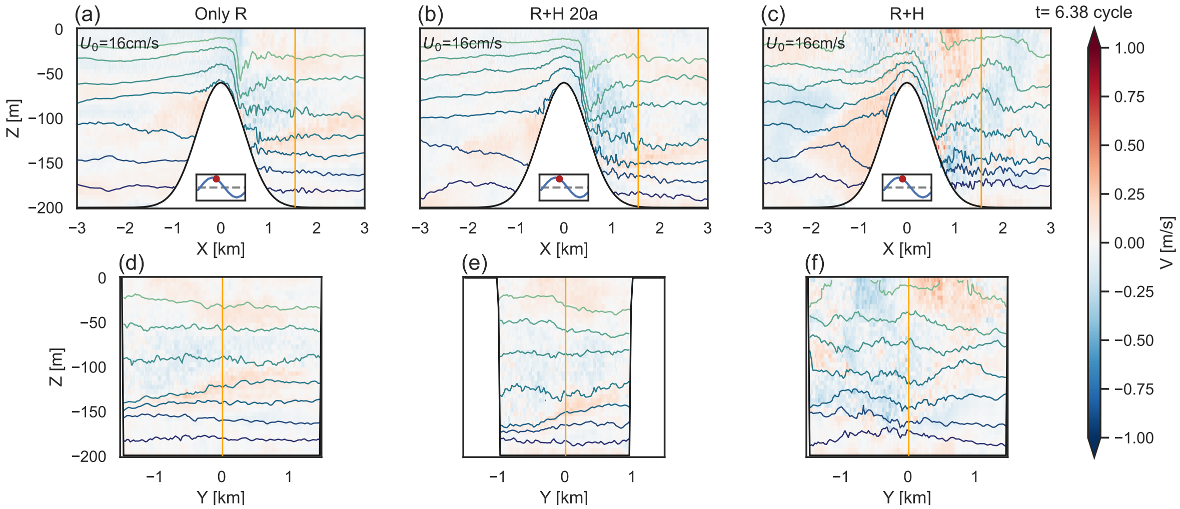

Figure 3.4: Flow and density structures 1.6 hrs after the flood peak tides ($t = 6.38$ cycles). This figure is similar to Figure 3.3, but shows V-velocity instead of U-velocity.

3.3.2 Vorticity Field

In this subsection, vorticity ($\zeta = \frac{\partial v}{\partial x} - \frac{\partial u}{\partial y}$) is shown to illustrate the temporal and spatial of vortex evolution. Vortices are generated in the lee of the headlands around both peak ebb and flood tides. Vortices generated during flood tides are referred to as flood vortices and are always located at $x > 0$ in our experiment, while those generated during ebb tides, referred to as ebb vortices, are located at $x < 0$. The vortices transition from barotropic during generation to baroclinic during development/advection, return to barotropic when trapped, and become baroclinic again due to tilting upon release.

The surface vorticity field is almost symmetric when vortices are generated at the tip of the headlands during peak tides (Figure 3.5 r). These flood vortices initially form as symmetric dipole structures (for $Y = 0$ axis) at the surface, with negative vorticity on the right-hand side and positive vorticity on the left-hand side relative to the flow direction. Vertically, the vertical confined structure of these vortices suggests predominantly barotropic motion during their initial formation (Figure 3.5j). However, deeper in the water column, the vortices with positive vorticity on the left-hand side become narrower and tilt rightward at depths below 80 m, introducing some asymmetry and baroclinicity in the deeper layers.

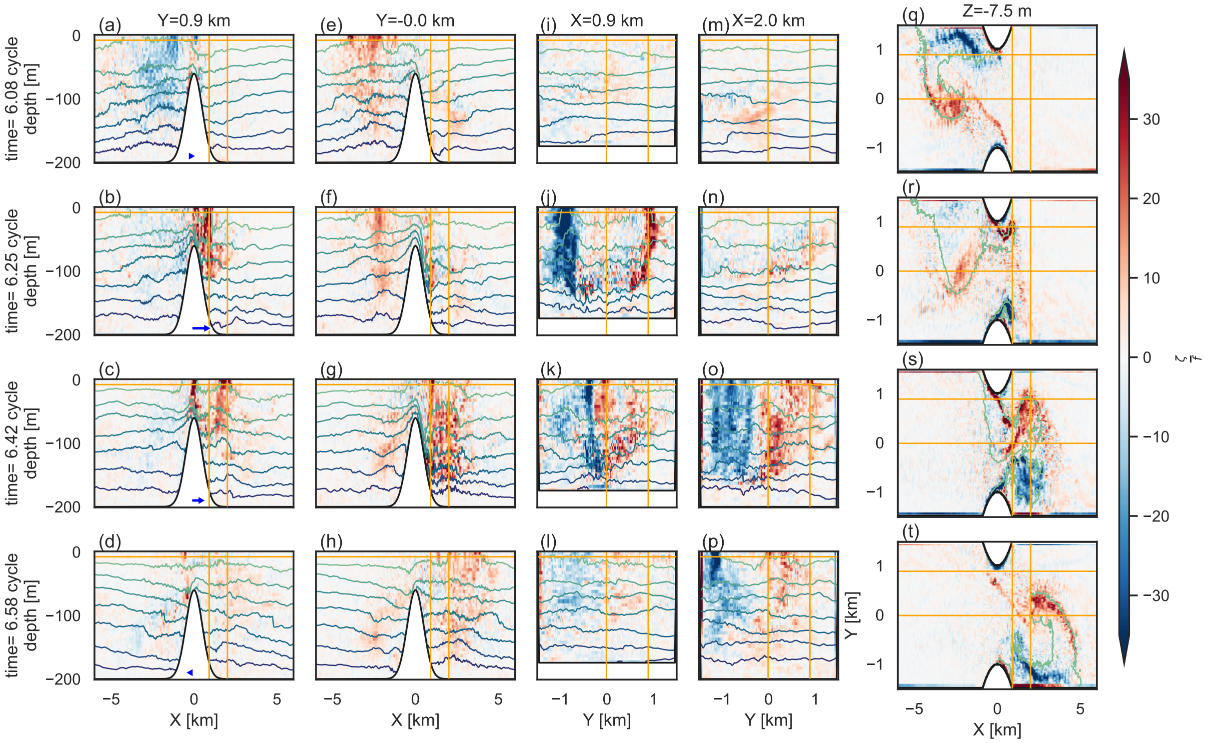

Figure 3.5: Temporal evolution of normalized vertical vorticity $\frac{\zeta}{f}$ and density structures over a half tidal cycle. This figure is similar to Figure 3.2. The vortices transition from (second row) barotropic during generation to (third row) baroclinic during development/advection, return to (fourth row) barotropic when trapped, and (first row see upstream) become baroclinic again due to tilting upon release.

About 1.6 hours after their formation, the flood vortices spread and shift slightly to the right, with the vortex extending to around 120 m deep and advecting downstream to approximately 3 km (Figure 3.5 k,o,s). As the vortices continue to advect, they further tilt toward the right-hand wall, especially noticeable in the positive vorticity vortex below 100 m (Figure 3.5 o). However, when vortices become trapped within the wake region (flood vortices in Figure 3.5 t), they regain a predominantly barotropic nature. Since flood and ebb vortices share a consistent pattern of evolution, the trapped stage observed for flood vortices (Figure 3.5t) can also represent that of ebb vortices, as seen in Figure 3.5a,e,q. By examining flood vortices up to 6.57 cycles and returning to 6.08 cycles to observe ebb vortices, we effectively capture the entire process without redundancy. Finally, when the trapped ebb vortices are released (Figure 3.5e,f,g), tilting once again reintroduces baroclinic contributions. The surface vorticity appears to retract toward the center ($x = 0$) with some residual positive vorticity persists at depths between 100 and 150 m (Figure 3.5g,h). This corresponds to some upstream isopycnal displacements mentioned in the flow field (Figure 3.3c), suggesting that while surface vortices may dissipate, deeper structures tend to linger longer.

This dipole configuration complements the flow field discussed earlier, where vorticity signals are observed in regions corresponding to the jet and vertical confined flow. As shown in Figure 3.5 g, the strong vertical confined flow is clearly aligned with the wake vortices, and the edge of these vortices corresponds to the trough of the lee waves. The more northern transect (Figure 3.5 b) shows that the lee waves coincide with the generation of vortices during flood tides, and these vortices continue to develop at the ridge crest (Figure 3.5 c). The vortices with positive vorticitiy contribute to the upward displacement of isopycnals at their core.

The life cycle of each vortex is approximately less than or equal to a full tidal cycle, with remnants from each phase persisting until the next vortex of the same phase fully replaces it. To illustrate the depth variation and life cycle of these vortices, we plotted the depth-integrated vorticity over a complete tidal cycle (Figure 3.6) and compared it with the surface vorticity (Figure 3.5 q-t). During peak tides, new vortices emerge at the headland tip (Figure 3.6 b), while remnants of vortices from the previous half cycle are still detectable upstream. The depth-integrated vorticity reveals that upstream vorticity can persist until the next vortex of the same phase forms.

For example, at peak flood tide (Figure 3.6b), new flood vortices form at the headland tip. These vortices advect downstream, tilt, and become trapped around $x = 2$ km as the flow transitions towards ebb tides (Figure 3.6c-e). By the time the flow returns to flood conditions (Figure 3.6a), the negative component of the previous flood vortex has nearly disappeared, while the positive component persists longer. This persistence is further evidenced in Figure 3.6b, where a weaker residual signal from older flood vortices is visible around $x = 2.5$ km, in addition to the strong

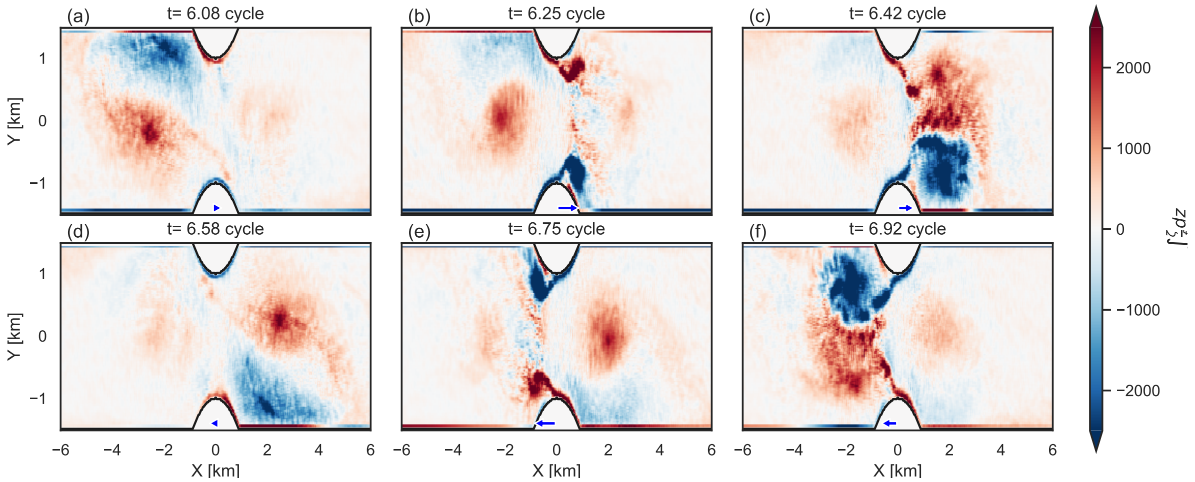

Figure 3.6: Temporal evolution of depth-integrated normalized vertical vorticity $\frac{\zeta}{f}$ over a tidal cycle. Arrows at bottom of the plots show the tidal forcing at that time. The life cycle of each vortex is approximately less than or equal to a full tidal cycle, with remnants from each phase persisting until the next vortex of the same phase fully replaces it.

signal of newly formed flood vortices at the headland tip. However, once the new flood vortex reaches the 2 km location (Figure 3.6c), the older flood vortices have fully dissipated, merged, or been replaced.

3.3.3 Vortex Decay and Mixing

The flow and vorticity fields indicate that the impact of vortices is primarily localized within approximately -6 km to 6 km from the generation site, with most vortices dissipating before the next vortices are generated. Here, we explore the key mechanisms influencing vortex decay, focusing on centrifugal and shear instabilities. While various potential mechanisms were discussed in the introduction—such as centrifugal, baroclinic, elliptical, and zigzag instabilities—our analysis concentrates on centrifugal and shear instabilities. Centrifugal instability typically occurs under conditions of high *Re* and *Ro*, which align with the flow characteristics in our study area. Meanwhile, shear instability is particularly significant where strong velocity gradients exist, especially within tilted vortex structures (Wynne-Cattanach et al., 2022).

Shear instability is suggested to be the primary mechanism influencing the decay of this headland-driven vortex, as opposed to centrifugal instability. The time series of maximum and minimum vorticity (not shown here) did not show signs of centrifugal

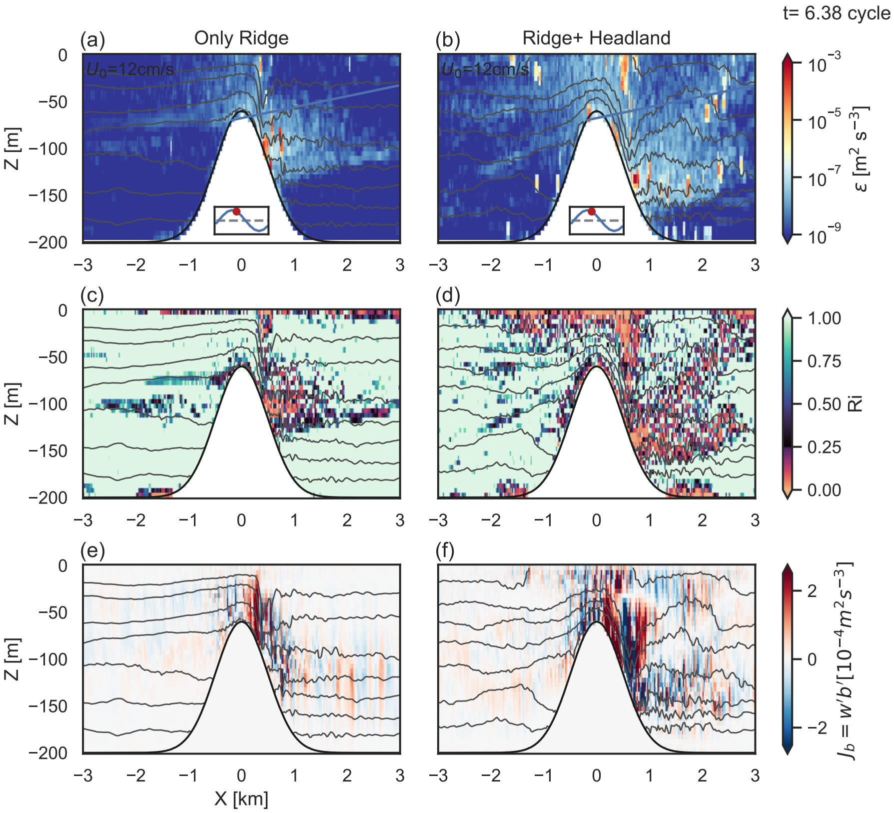

Figure 3.7: Snapshots of (a,b) vertical dissipation rate ϵ_v and (c,d) Ri (e,f) $J_b = w'b'$ at $Y = 0$ transect 1.6 hrs after the flood peak tides ($t = 6.38$ cycles). Left column is from *only R* and right column is from *R+H* experiments. Enhanced turbulent dissipation rates are in the region of the vertical confined flow where $Ri = \frac{N^2}{S^2} < 0.25$, suggesting shear instability may the primary mechanism driving turbulence for these headland wake vortices.

instability, such as the decay of high vorticity to inertial frequencies or asymmetric positive and negative vorticity. Another possibility is that our MITgcm model is hydrostatic, and centrifugal instability may require a non-hydrostatic mode to be accurately simulated (Dewar et al., 2015). Enhanced turbulent dissipation rates are in the region of the vertical confined flow (Figure 3.7b) where a Richardson number $Ri = \frac{N^2}{S^2} < 0.25$ (Figure 3.7d), where $N^2 = -\frac{g}{\rho}\frac{\partial \rho}{\partial z}$ and $S^2 = (\frac{\partial u}{\partial x})^2 + (\frac{\partial v}{\partial y})^2$. These results suggest that vortex-induced shear is an additional driver of turbulence and instability beyond the traditional lee wave dynamics. Thus, shear instability is the primary mechanism driving turbulence in headland wake vortices. This aligns with the findings of Srinivasan et al. (2021), which indicate that at relatively large Ro, such as in our case ($Ro = 0.89$), shear instability tends to dominate, whereas at small Ro, centrifugal instabilities are more prominent and contribute to stronger, asymmetric anticyclones.

Next, we explore the contribution of vortex decay to the vertical mixing by examining the buoyancy flux $J_b = w'b'$, where $b' = -g\frac{\rho-\rho_0}{\rho_0}$ and w' is the vertical velocity. We find that regions of strong dissipation often correspond to areas with larger $|J_b|$ magnitude. However, only the negative J_b values indicate the vertical mixing (i.e., heavy fluid parcels being transported upward and light parcels downward). These negative J_b regions are primarily located along isopycnal dipping zones.

Notably, in the headland case, additional negative J_b signals are observed not only downstream, but also upstream of the ridge, where the water was lifted more significantly than in the *only R* case. These enhanced upstream mixing signals are clearly visible in the temporal evolution of buoyancy flux shown in the following figure.

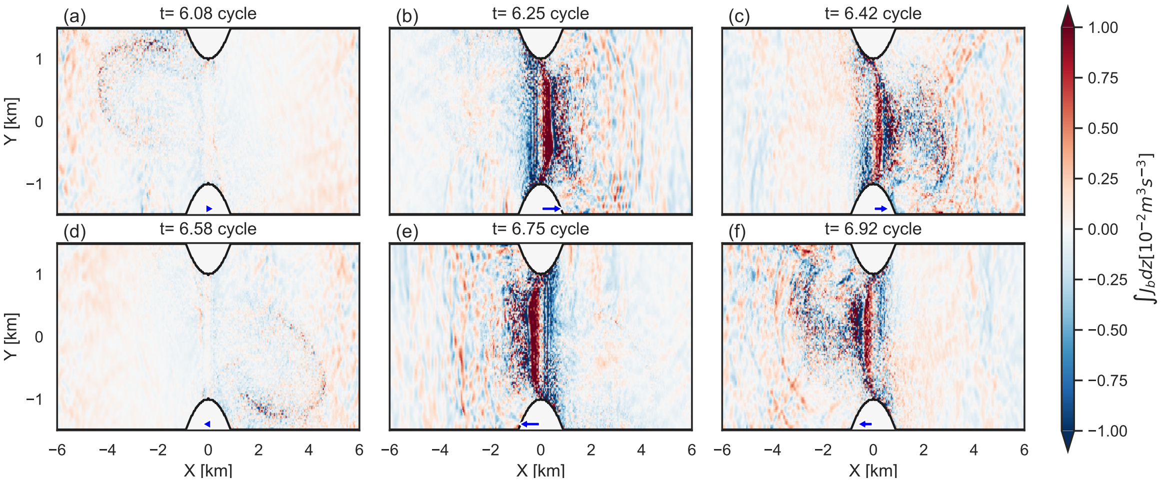

Figure 3.8: Temporal evolution of depth-integrated buoyancy flux J_b over a tidal cycle. Arrows at bottom of the plots show the tidal forcing at that time.

During the peak flood tide around cycle 6.25, strong negative J_b signals emerge both along the isopycnal dipping region downstream of the ridge and also in the upstream region where the water lifted up. Following the flood peak, as the flow continues in the flood direction and the vortex expands downstream, the J_b signals are observed trailing the vortex. However, once the flow reverses (transitioning from flood to ebb), the buoyancy flux signal diminishes sharply. Despite the continued presence of the flood-phase vortex (Figure 3.6), very little J_b remains. The same pattern occurs during the ebb tide.

3.4 Energetics

In this section, we explore the energetics of the stratified flow over a ridge-plus-headland channel, by examining how kinetic energy is distributed, how much tidal energy is converted into baroclinic motions, and how much these baroclinic energies are either locally dissipated or radiated away. We particularly examine how these processes are modified by the presence of headland-driven vortices by comparing two scenarios: *only R* and *R+H*. Finally, we expand our analysis to different tidal forcings and headland sizes to investigate how these energy processes scale with varying flow speeds and headland dimensions, which could provide insights for sub-grid mixing parameterization.

3.4.1 Kinetic energy

To understand the kinetic energy in the system, particularly in relation to vortices, we decompose the kinetic energy field into its 2D ($KE_{u_{2d}}$) and 3D ($KE_{u_{3d}}$) components, as outlined in the methods section. This decomposition can be useful because our ridge is a 2D feature, and by isolating the 3D kinetic energy $KE_{u_{3d}}$, we can attribute this component largely to the vortices generated by the headland in the *R+H* scenario. By performing the same decomposition for the *only R* scenario, we can directly compare the kinetic energy distribution and partitioning between the two configurations.

In the *R+H* scenario, our decomposition method for the 3D velocity component (u_{3d}) effectively isolates the vortex-related kinetic energy, demonstrating its reliability in capturing headland-driven dynamics. This is evidenced first by u_{3d} successfully extracting the signal of strong vertical confined flow (Figure 3.9b), consistent with the headland-driven vortices previously described in Figure 3.3c, which are absent in the *only R* scenario (Figure 3.9a). Second, the depth- and channel-integrated $\overline{\mathrm{KE}u_{3d}}^{yz}$ exhibits a clear advection pattern with tidal flow, extending up to $x = \pm 4$ km (Figure 3.9d). This signal aligns well with the vertical enstrophy ($\overline{\zeta^2}^{\mathrm{yz}}$; Figure 3.9f), confirming that $\mathrm{KE}_{u_{3d}}$ accurately represents the energy contribution of vortex dynamics.

The spatial distribution of tidally-averaged kinetic energy ($\langle\overline{KE}\rangle$) reveals a significant enhancement in the presence of headlands, with the total volume-integrated kinetic energy increasing by approximately 46 GJ in the *R+H* scenario, as annotated in the kinetic energy map (Figure 3.10a,b). This increase is primarily driven by the

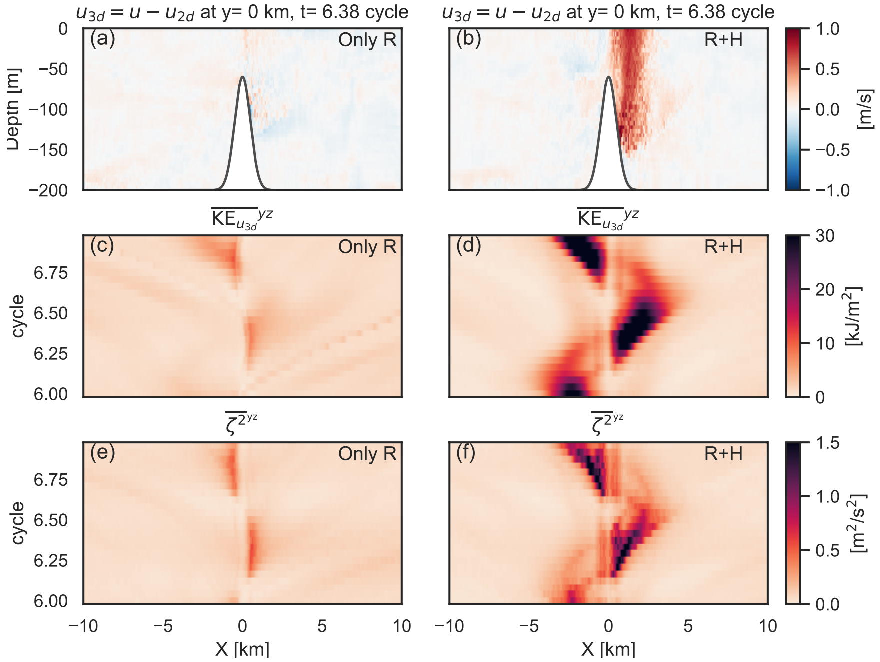

Figure 3.9: (a,b) Snapshot of u_{3d} near the ridge at $y = 0$ km and $t = 6.38$ cycle. Hovmöller diagram of area-integrated (in $y - z$ direction) (c,d) kinetic energy $\overline{\mathrm{KE}_{u_{3d}}}^{yz}$ and (e,f) vertical enstrophy $\overline{\zeta^2}^{yz}$. Left column is from *only R* and right column is from *R+H* experiments. Our decomposition method for the 3D velocity component (u_{3d}) effectively isolates the vortex-related kinetic energy.

barotropic component $\langle\overline{KE_{u_{bt}}}\rangle$, which accounts for 42 GJ of the total enhancement (Figure 3.10c,d). In contrast, the baroclinic component $\langle\overline{KE_{u_{bc}}}\rangle$ shows a more localized contribution of 4 GJ near the headlands, particularly around ($x = \pm(1-2)$ km, $y = \mp(0-500)$ m). The spatial map of $\langle\overline{KE_{u_{bc}}}\rangle$ also reveals the propagation of internal Kelvin waves along the right-hand side walls (Figure 3.10e,f).

The 2D kinetic energy field ($\langle\overline{KE_{u_{2d}}}\rangle$) remains consistent between the *R+H* and *only R* scenarios, confirming that the differences in 3D kinetic energy ($\langle\overline{KE_{u_{3d}}}\rangle$) arise primarily from vortices in the *R+H* scenario. While we do not explicitly decompose $\langle\overline{KE_{u_{2d}}}\rangle$ into barotropic and baroclinic components, the barotropic dominance is evident by comparing the separate maps of $\langle\overline{KE_{u_{bt}}}\rangle$ (Figure 3.10d) and $\langle\overline{KE_{u_{bc}}}\rangle$ (Figure 3.10f), which show that the former contributes more significantly to the total 2D field.

In the 3D energy field, $\langle\overline{KE_{u_{3d}}}^{V}\rangle$ in the *only R* scenario reflects contributions from internal Kelvin waves generated by the ridge. Comparing $\langle\overline{KE_{u_{3d}}}^{V}\rangle$ in the *only R* and *R+H* scenarios isolates the additional vortex-driven energy in the *R+H* case, since only the latter includes headland-generated vortices superimposed on the internal Kelvin waves. This comparison provides a framework for attributing the energetic difference in the 3D fields to vortex activity.

The time series of volume-integrated kinetic energy $\overline{KE}^V$ reveals the energy tendency ($\frac{dKE}{dt}$) (Figure 3.11), offering insights beyond the static reservoir analysis provided by kinetic energy fields. In the $R{+}H$ scenario, while the enhanced $\overline{KE}^V$ (blue curve, Figure 3.11) reservoir is dominated by barotropic energy ($\overline{KE_{u_{bt}}}^V$, orange curve, Figure 3.11), the temporal evolution shows that vortices are not purely barotropic (Figure 3.5 j,k,o). Instead, the time series highlights dynamic energy exchanges between barotropic and baroclinic components as vortices form, expand, and advect, and ultimately become trapped or released during tidal reversals.

At the initial stages of vortex generation near the headland tip, the vortices exhibit a largely barotropic character, consistent with the strong vertical confined flows observed in the vorticity field (Figure 3.5j). As vortices expand and advect downstream, tilting mechanisms begin to introduce baroclinic contributions (Figure 3.5k,o). The time series shows that when barotropic kinetic energy ($\overline{KE_{u_{bt}}}^V$, orange curve in Figure 3.11) decreases, there is a corresponding increase in baroclinic ($\overline{KE_{u_{bc}}}^V$, green curve in Figure 3.11) and 3D kinetic energy ($\overline{KE_{u_{3d}}}^V$, purple curve in Figure 3.11), reflecting energy transfer associated with vortex tilting and vertical structure. When vortices become trapped and stabilize, they regain a predominantly barotropic nature (upstream in Figure 3.5e,f), but as the tides reverse and release the trapped vortices, tilting reintroduces baroclinic and 3D components into the system (upstream in Figure 3.5g,h).

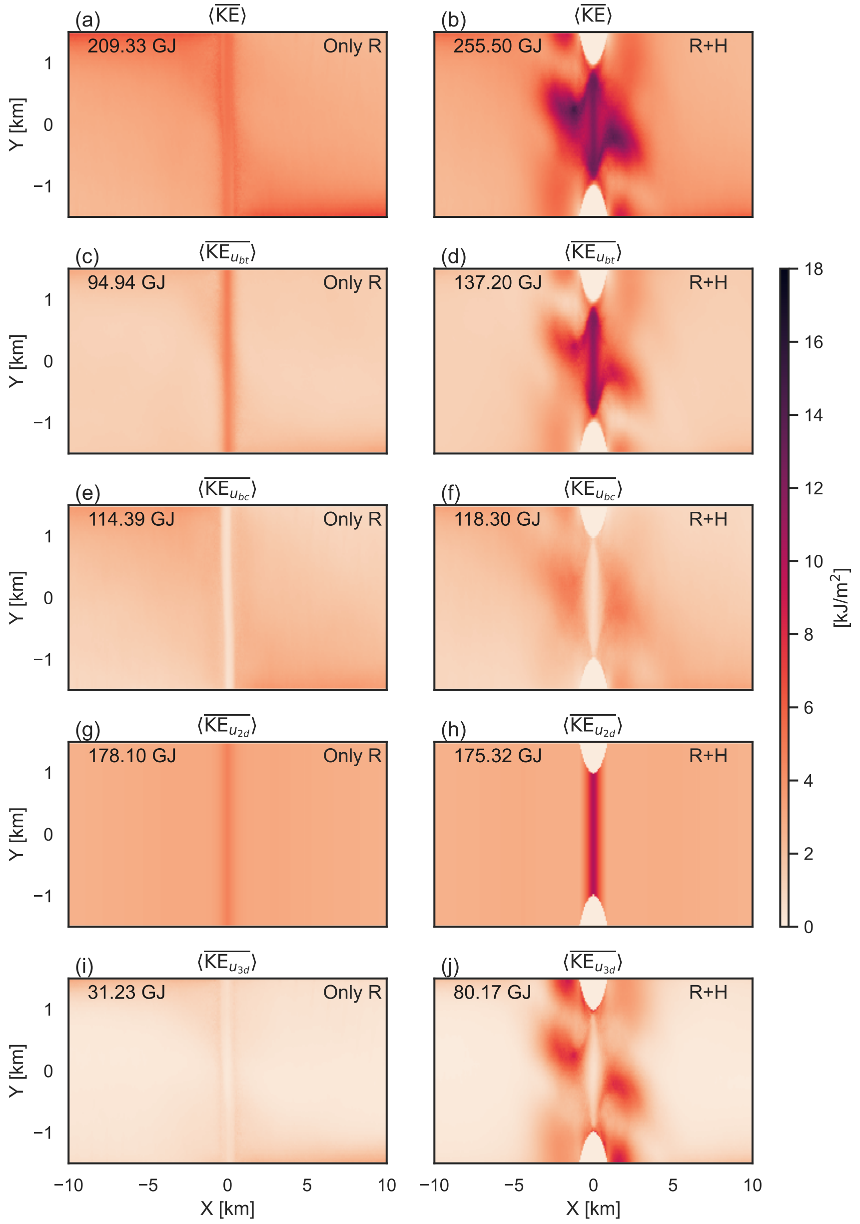

Figure 3.10: Tidally-averaged, depth-integrated kinetic energy distributions. Rows show $x-y$ spatial distributions for (a, b) total kinetic energy $\langle\overline{KE}\rangle$, (c, d) barotropic kinetic energy ($\langle\overline{KE_{u_{bt}}}\rangle$), (e, f) baroclinic kinetic energy $\langle\overline{KE_{u_{bc}}}\rangle$, (g, h) 2D kinetic energy $\langle\overline{KE_{u_{2d}}}\rangle$, and (i, j) 3D kinetic energy $\langle\overline{KE_{u_{3d}}}\rangle$. Each volume-integrated energy over -10 km $< x <$ 10 km is shown as text. Left column is from *only* R and right column is from R+H experiments. The spatial distribution of tidally-averaged kinetic energy reveals a significant enhancement in the presence of headlands, mostly from barotropic kinetic energy and 3D kinetic energy.

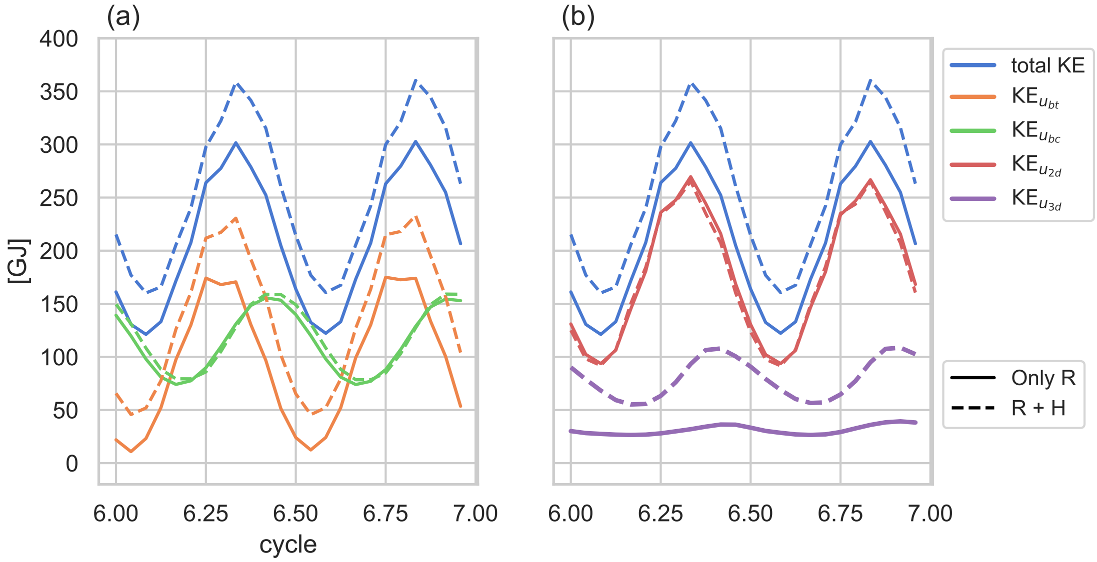

Figure 3.11: Time series of volume-integrated kinetic energy $\overline{KE}^V$. (a) Blue curves represent total kinetic energy $\overline{KE}^V$, orange for BT kinetic energy $\overline{KE_{u_{bt}}}^V$, green for BC kinetic energy $\overline{KE_{u_{bc}}}^V$, (b) red for 2D kinetic energy $\overline{KE_{u_{2d}}}^V$, and purple for 3D kinetic energy $\overline{KE_{u_{3d}}}^V$. Solid lines indicate the *only* R scenario, while dashed lines indicate the R+H scenario. The time series of volume-integrated kinetic energy $\overline{KE}^V$ shows that vortices in the R+H scenario consume approximately 3.84 MW more energy than in the *only* R scenario. This was estimated by analyzing the rate of change in $\overline{KE_{u_{3d}}}^V$ over a quarter tidal cycle, converting the energy difference in GJ to an average power input in MW.

Finally, we quantify the power input into vortices by analyzing the rate of change in $\overline{KE_{u_{3d}}}^V$. Over a quarter tidal cycle (from 6.417 to 6.167 cycles), $\overline{KE_{u_{3d}}}^V$ in the R+H scenario increases from 55 GJ to 108 GJ, corresponding to an average power input of 4.72 MW. In the *only* R scenario, $\overline{KE_{u_{3d}}}^V$ increases from 26.5 GJ to 36.4 GJ, corresponding to an average power input of 0.88 MW. The difference of $\overline{KE_{u_{3d}}}^V$ between R+H and *only* R scenarios gives us an estimate that the vortices in the R+H scenario take approximately 3.84 MW of additional energy.

3.4.2 Baroclinic energy

After examining the kinetic energy field, the rate of change in $\overline{KE_{u_{3d}}}^V$ provides an average estimate of how much energy the vortices gain over time, 3.84 MW. Now, we will look at the baroclinic energy balance and also compare the two scenarios: *only* R and R+H, to tackle the energetics role of vortices.

The conversion of tidal energy into the baroclinic motions $\langle\overline{C_{BT-BC}}\rangle$ is enhanced by the precence of the headland. The spatial distribution of conversion is concentrated along the flanks of the ridge (Figure 3.12b,d) in both scenarios *only R* and *R+H*, but the introduction of the headland amplifies the conversion. While the *only R* scenario shows a fairly two-dimensional pattern deflected toward the right wall due to rotation (Figure 3.12 b), *R+H* case introduces intensification near the inner faces of the headlands where it connects with the ridge and broader along-channel range (Figure 3.12 d). Integrating conversion across the channel $\langle\overline{C_{BT-BC}}^{yz}\rangle$, the range of energy conversion is slightly broader in the presence of the headland than with *only R* (Figure 3.12 f). This broader range of conversion, when integrated over the entire volume $\langle\overline{C_{BT-BC}}^{V}\rangle$, results in an increased total energy budget, adding an additional 3.7 MW in the *R+H* case.

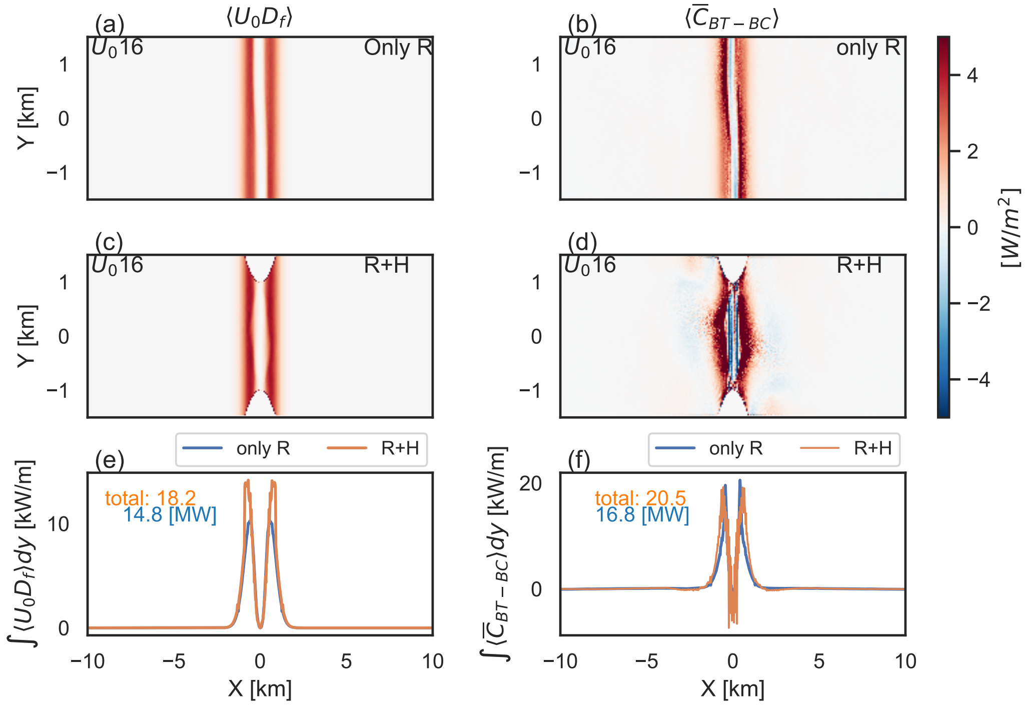

Figure 3.12: Tidally-averaged power loss and energy conversion distributions. Left column (a,c) shows tidally-averaged power loss from form drag, $\langle U_0 D_f \rangle$; and right column (b,d) shows tidally-averaged depth-integrated BT-BC conversion $\langle \overline{C_{BT-BC}} \rangle$. Spatial distributions of energy in the $x-y$ plane for the (a,b) *only R* and (c,d) *R+H* scenarios. The third row (e,f) shows the y-integrated values for each scenario as line plots, with volume-integrated values (integrated over y and x) annotated as text on the plots. Note that (e) and (f) have different y values. The additional tidal power loss caused by the headland is estimated from the power loss due to form drag (3.4 MW = 18.2 - 14.8 MW) and barotropic-baroclinic (BT-BC) conversion (3.7 MW = 20.5 - 16.8 MW). Although form drag losses are consistently weaker in intensity compared to BT-BC conversion, both provide similar estimates of the additional power loss.

Another way to estimate how much tidal energy is lost in the presence of topography is by calculating the power loss due to form drag ($\mathcal{D}_{\mathrm{f}}$), which can be expressed as $U_0\mathcal{D}_{\mathrm{f}}$, where $\mathcal{D}_{\mathrm{f}} = \int\int P_{bot}\frac{dh}{dx}dxdy$. In order to make the consistent physical term with $\langle\overline{C_{BT-BC}}\rangle$, the term $P_{bot}\frac{dh}{dx}$ is defined here as local form drag $\mathcal{D}_{\mathrm{local}}$, and the spatial distribution of tidally-averaged local energy loss from form drag as $\langle U_0\mathcal{D}_{\mathrm{local}}\rangle$ is shown in Figure 3.12a,c. Overall, energy loss due to form drag occurs in similar locations to conversion but is consistently weaker in intensity (Figure 3.12ac vs bd). In the *only R* scenario, the distribution of power loss due to form drag primarily occurs on both flanks of the ridge. The y-integrated power loss $\langle\overline{U_0\mathcal{D}_{\mathrm{local}}}^{y}\rangle$ (Figure 3.12e) shows lower peak values compared to conversion (Figure 3.12f). The area-integrated power loss $\langle U_0\mathcal{D}_f\rangle$ estimates from form drag are consistently about 2 MW less than the conversion (i.e., 14.8 v.s 16.8 MW in *only R* and 18.2 v.s 20.5 MW in *R+H*; Figure 3.12e,f). Despite this difference, the additional tidal power loss caused by the presence of headland (3.4 MW = 18.2-14.8 MW) is very close to the 3.7 MW increase in conversion.

It is important to note that in this study, the headland is represented as a vertical sidewall rather than a sloping topography. As a result, the headland itself does not contribute explicitly to form drag calculations because its slope ($\frac{dh}{dx}$ is infinity, making $P_{bot}\frac{dh}{dx}$ vanish. However, the presence of the headland still modifies the local pressure field, creating a pressure difference between the upstream and downstream regions. Furthermore, while the headland walls themselves do not generate form drag, they are connected to the underwater ridge, where dh/dx is nonzero. This connection suggests that some degree of headland influence on form drag may still be present.

The time series of form drag $\mathcal{D}_f$ reveals that the presence of the headland enhances its magnitude by approximately 1.2 times, while the phase relationship with U_0 remains consistent between scenarios (Figure 3.13a). This enhanced magnitude directly increases the power loss associated with form drag, which is also approximately 1.2 times greater in the *R+H* scenario (Figure 3.13b). In the *only R* scenario, the time series of form drag $\mathcal{D}_f$ shows a weakening after reaching its peak (blue curve, Figure 3.13 a), which is likely linked to the approach-controlled flow, as discussed in our previous research and also captured here (Figure 3.3 a). Form drag manifests as the pressure drop associated with the isopycnal depression on the downstream side of the ridge. The isopycnals in approach-controlled flow respond differently compared to crest-controlled flow. The addition of the headland amplifies the magnitude of form drag without altering its phase, ultimately enhancing tidal power loss.

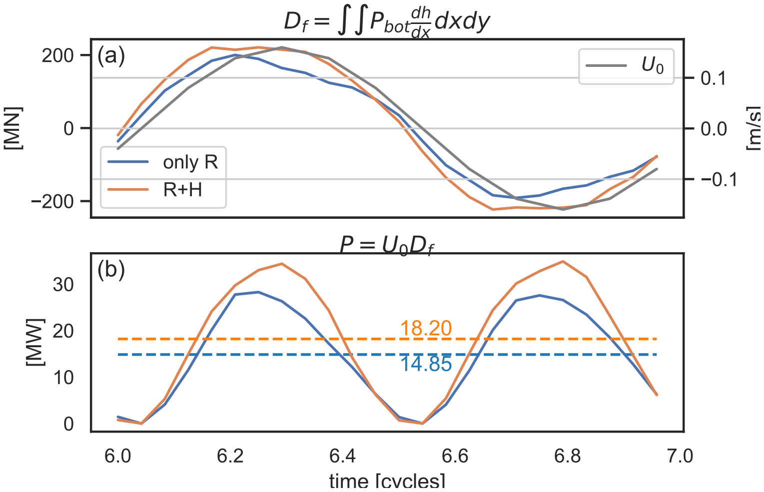

Figure 3.13: Time series of form drag $\mathcal{D}_f$ and its power loss $U_0\mathcal{D}_f$. Blue curves are for *only R* scenarios and orange for *R+H* scenarios. Dashed lines are tidally-averaged values (14.84 MW for *only R* and 18.20 MW for *R+H*). The time series of form drag $\mathcal{D}_f$ reveals that the presence of the headland enhances its magnitude by approximately 1.2 times, while the phase relationship with U_0 remains consistent between scenarios.

Turbulent dissipation is intensified by the presence of the headland, particularly around the vortex formation and advection region (-5 km $< x <$ 5 km). Horizontal ($\langle\overline{\epsilon_h}\rangle$) and vertical ($\langle\overline{\epsilon_v}\rangle$) turbulent dissipation show substantial differences between scenarios. In the *only R* case, dissipation is concentrated along the ridge flanks, with horizontal dissipation skewed by internal Kelvin waves and vertical dissipation exhibiting a uniform 2D pattern (Figure 3.14a,b). In the *R+H* case, vortices generated by the headland amplify dissipation near $x = 0$, spreading diagonally outward (Figure 3.14c,d). Integration along y (solid curves, Figure 3.14e,f) shows higher peak dissipation values but also broader ranges of dissipation along x compared to *only R*. Note that the vertical and horizontal dissipation plots have different y-axis limits due to the large difference between peak values and the surrounding dissipation levels in the vertical dissipation.

Further integrating the y-integrated dissipation cumulatively along x (dashed curves, Figure 3.14e,f), in the *R+H* scenario, dissipation continues to increase past where the ridge is located ($x =$ 0–1 km), whereas in the *only R* scenario, dissipation plateaus. In *R+H* scenario, horizontal turbulent dissipation $\langle\overline{\epsilon_h}^V\rangle$ increases by approximately 1.1 MW (i.e., 1.9 MW in *R+H* compared to 0.8 MW in *only R*). The additional 1.1 MW represents dissipation attributed to vortices, contrasting with the

0.8 MW contributed by internal tides alone. This indicates that local dissipation due to vortices can exceed that caused by internal tide-driven interior turbulence. Similarly, vertical turbulent dissipation $\langle \overline{\epsilon_v}^V \rangle$ increases by around 1.9 MW (i.e., 3.5-1.6 MW). The total dissipation from vortices in this case amounts to about 3 MW (1.9 + 1.1 MW), while dissipation from internal tides alone is 2.4 MW (1.6 + 0.8 MW). These findings are comparable to Klymak and Gregg (2004), where breaking lee waves were estimated to contribute around 1 MW to interior turbulence, compared to 2.2 MW attributed to vortices.

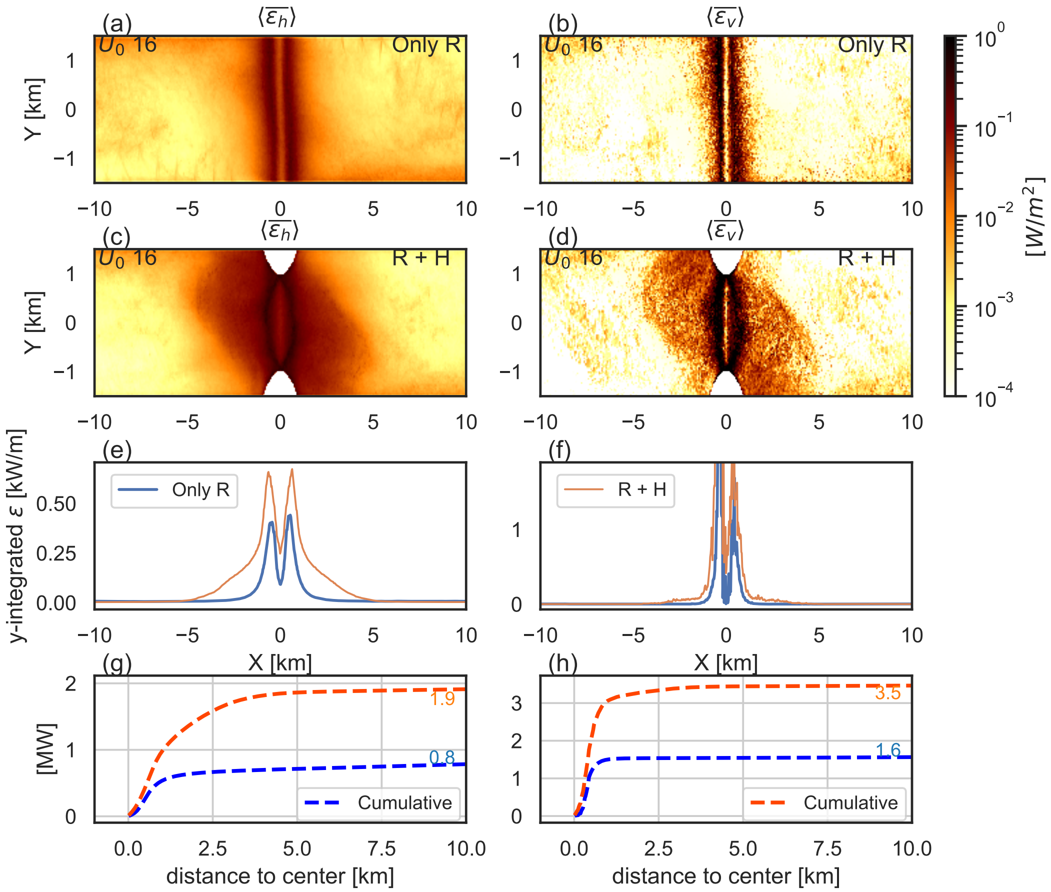

Figure 3.14: Tidally-averaged depth-integrated turbulent dissipation. Left column (a,c,e) shows horizontal dissipation rate, $\langle\overline{\epsilon_h}\rangle$; and right column (b,d,f) shows vertical dissipation rate, $\langle\overline{\epsilon_v}\rangle$. Spatial distributions of energy in the $x-y$ plane for the (a,b) *only* R and (c,d) R+H scenarios. The third row (e,f) shows the y-integrated values for each scenario as line plots. Note that (e) and (f) have different y values. (g,h) The cumulative integrals, represented by dashed curves, are calculated by integrating symmetrically from $x = 0$, where contributions from $x > 0$ and $x < 0$, are combined into a single cumulative value at each step. The final cumulative totals are annotated as text on the plots. The presence of the headland intensifies turbulent dissipation, with vortices contributing about 3 MW (1.9 + 1.1 MW) compared to 2.4 MW (1.6 + 0.8 MW) from internal tides, and local vortex dissipation exceeding that of internal tide-driven turbulence.

Despite the noticeable increase in turbulence near the generation region in the presence of the headland, the baroclinic energy flux along the channel, a measure of the energy carried by radiating internal tides, remains similar to that in the case without the headland (blues compared to oranges in Figure 3.15). The baroclinic energy flux is integrated along the y-direction to obtain a net flux at specific x-transects; thus, the total radiating energy from the region is calculated by subtracting the net flux values at two different x-locations. This baroclinic energy flux consists of two components: pressure work $u_{bc}p_{bc}$ (dashed curves) and energy advection uE_{bc} (dotted curves). While both components are generally similar, there are differences in uE_{bc} around -4 $< x <$ 4 km. However, this difference can neglect when considering the total radiating energy leaving the region, as our energy budget focuses on flux values at $x = \pm 10$ km), where both scenarios yield similar values, with the R+H scenario showing a slight reduction of approximately 0.3–0.4 MW. This does tell us the impact of presence of headland-driven vortices on how much internal tides radiate is minimal. For the total radiation of internal tides, we calculate 5.5 - (-5.5) = 11 MW at $x = \pm 10$ km, which also aligns with 15 MW estimated by Klymak and Gregg (2004).

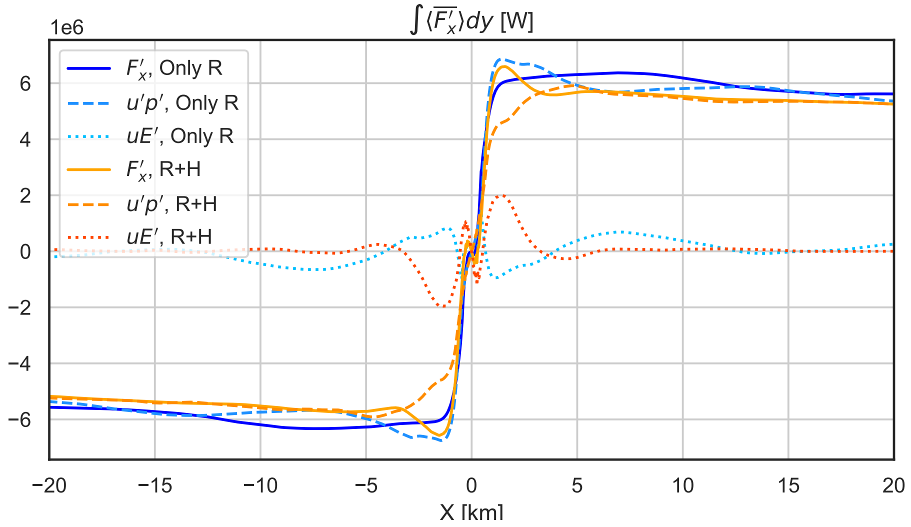

Figure 3.15: Tidally-averaged yz-integrated baroclinic energy flux $F_{bc,x}$ along the channel. Blues are *only* R scenarios and oranges are R+H. This baroclinic energy flux consists of two components: pressure work $u_{bc}p_{bc}$ as dashed curves and energy advection uE_{bc} as dotted curves. The baroclinic energy flux along the channel, a measure of the energy carried by radiating internal tides, remains similar to which is without headland.

The additional tidal energy loss in the presence of the headland was estimated using several methods, all yielding similar results: 3.7 MW calculated from the energy BT-BC conversion, 3.4 MW from form drag estimates, and 3.84 MW from the time-averaged kinetic energy input in the time series. The consistency across these methods provides strong support for our estimates. Turbulent dissipation measurements show that approximately 3 MW of this additional energy is dissipated locally by vortices, indicating that most of the extra energy drawn from the tides by vortices is lost locally. Meanwhile, the amount of energy radiated outward by internal tides remains largely unaffected by the generation, advection, and dissipation of vortices, with a substantial 11 MW of energy continuing to radiate outward.

3.4.3 Power loss estimate from bluff body law

We hypothesize that the energy loss induced by the headland can be estimated using the bluff body law, but careful selection of the flow velocity and cross-sectional area is crucial. Initial calculations show that when using the flow velocity influenced by the ridge and the exposed-only area, the estimated energy loss is very close to the actual simulated value.

To estimate this additional power loss due to headland vortices, we apply the bluff body formula $D_b = 0.5\rho C_d U^3 A$. Using a flow velocity $U_0 = 0.16$ m/s, , we consider two possible cross-sectional areas for A: (1) the full headland depth down to the seafloor, giving $A = 2 \times 500 \times 60 = 200,000 \text{ m}^2$, and (2) only the exposed portion above the ridge, where the height is 60 m, giving $A = 2 \times 500 \times 60 = 60{,}000 \text{ m}^2$. The possible estimated power loss are (1) 0.4 MW and (2) 0.12 MW, which are both significantly smaller than the observed difference in drag. This suggests that either the drag coefficient or the effective flow velocity needs adjustment or bluff body law is not applicable.

If we consider adjusting the flow velocity, a rough estimate shows that a two- or three-fold increase in velocity would be required to match the observed power difference (i.e., $(\frac{3.4}{0.12})^{\frac{1}{3}} \approx 3, (\frac{3.4}{0.4})^{\frac{1}{3}} \approx 2$). Under ridge-induced constriction, the flow velocity increases by a factor of 3.3. When further constricted by the headland, the velocity increases additionally by a factor of 1.5, resulting in a combined acceleration factor of approximately 4.95. Here, the ridge-constricted velocity U_r is defined as $U_r = U\frac{H}{H-h}$, where U_0 is the undisturbed flow velocity, H is the total water depth, and $H - h$ represents the constricted depth. Applying the ridge-constricted only velocity and exposed-only area to our bluff body estimation, with $U_r = 0.533$ m/s, $A = 60,000$ m^2, and assuming a drag coefficient $C_d = 1$, energy loss is estimated approximately 4.55 MW.

These calculations suggest that the energy loss induced by the headland, even when lee waves are co-generated, may be reasonably estimated using the simple bluff body law, provided that the flow velocity is appropriately adjusted to account for the effects of topographic constriction and the appropriate cross-sectional area. We will see this being tested later in this study to different tidal forcing and headland shapes.

3.4.4 Power law of baroclinic energy with U_0

Previously, we demonstrated how the presence of headland-driven vortices under a tidal forcing of $U_0 = 16$ cm/s affects the flow structure, vorticity, kinetic energy, and baroclinic energy. Our analysis illustrates the role that headland-driven vortices play in the system's dynamics and energetics. To further explore this, we expanded our experiments to cover a range of tidal forcings, as detailed in the methods section. This expansion allows us to investigate a broader parameter space, crossing from $Ro < 1$ to $Ro > 1$, maintaining $Fr \ll 1$ and $Bu = 88.2$, and transitioning from $Kc < 1$ to $Kc > 1$, and from $St = 1$ to $St \ll 1$. Notably, we also crossed the critical $St = 0.13$ that indicates vortex shedding (see Table 3.1). Our focus here is to understand how baroclinic energy scales with U_0 within these parameter ranges.

In our experiments, the energy conversion for the *only R* scenario, closely follows the predictions of the Knife-edge model, up until $U_0 > 16$ cm/s (Figure 3.16a). The Knife-edge model is an analytical framework predicting energy conversion in supercritical topography interacting with tidal flows, scaling with tidal forcing ($\propto U_0^2$). Beyond this, energy conversion begins to deviate and slows down, a phenomenon we described in our previous work as conversion saturation associated to onset of approach-controlled flow. However, in the *R+H* scenario, the presence of the headland alters this saturation (Figure 3.16b), bringing the energy conversion back in line with the Knife-edge model. This increased conversion mirrors our earlier results at $U_0 = 16$ cm/s, where the addition of the headland caused the tides to lose more energy.

When we subtract the conversion in the *only R* scenario from that in the *R+H* scenario, we find that the difference scales with U_0^3 (Figure 3.16c). Extending the analysis discussed previously, we hypothesize that the energy loss induced by headland-driven vortices can be reasonably estimated using the bluff body drag law $D_b = 0.5\rho C_d U^3 A$,

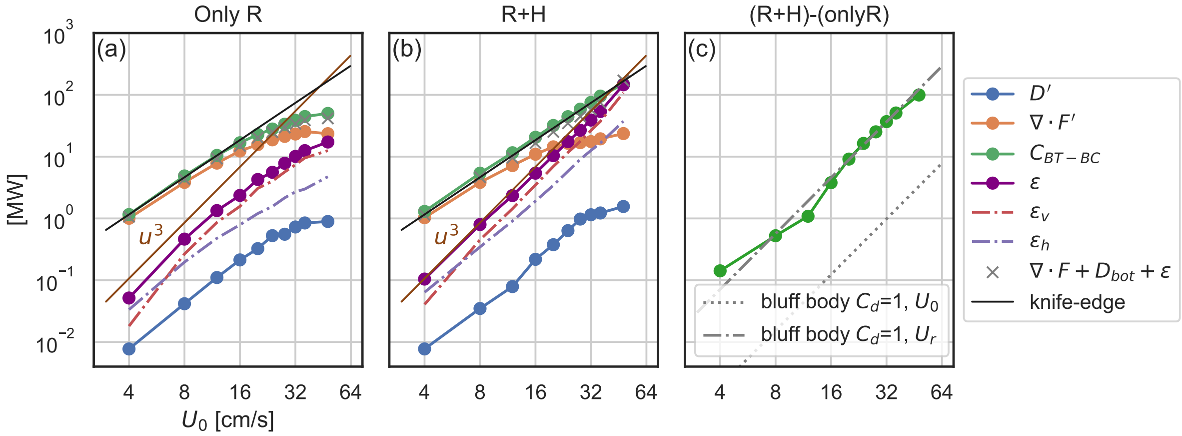

Figure 3.16: Tidally-averaged volume-integrated baroclinic energy budget as a function of U_0 for different scenarios: (a) *only R* experiment, (b) R+H experiment, and (c) the difference in conversion between R+H and *only R*. Green lines indicate conversion, orange lines represent baroclinic energy flux divergence (radiation), purple lines show total dissipation (dashed light red for vertical, dashed light blue for horizontal), blue lines are bottom drag, black lines correspond to the Knife-edge model (U_0^2 scaling), brown lines are U_0^3 scaling, and gray x-mark lines show total energy sink, including radiation, dissipation, and bottom drag. (a) shows energy saturation ($U_0 > 16$ cm/s), while (b) demonstrates that headland addition removes saturation except for radiation. (c) highlights that the additional conversion caused by the headland aligns with bluff body drag estimates using ridge-constricted velocity U_r (dash-dotted) but not U_0 (dotted).

provided that the flow velocity and cross-sectional area are appropriately selected. This hypothesis aligns well with our earlier discussion, where the ridge-constricted velocity U_r, the exposed cross-sectional area and drag coefficient $C_d = 1$ were found to yield power loss estimates closely matching our simulation result (see Figure 3.16c, gray dash-dotted line).

Another intriguing finding is that, regardless of the presence of headland, the energy radiated as internal tides remains nearly similar (orange curves in *only R* v.s R+H; Figure 3.16a,b). This result extends our earlier result, where the addition of a headland had no significant impact on the radiated energy under one specific forcing.

3.4.5 Impact of headland size on baroclinic energy

To better understand the influence of headland size, we extended our analysis across different headland sizes, varying both the cross-channel (b) and along-channel (a)

lengths, with the aspect ratio $0.01 < \lambda < 0.45$. We altered parameters related to headland along-channel size, such as Ro, Kc, St, and Bu, while the Froude number (Fr) remained in a similar range to the base run, staying below 1 ($Fr < 1$). (see method Table 3.1).

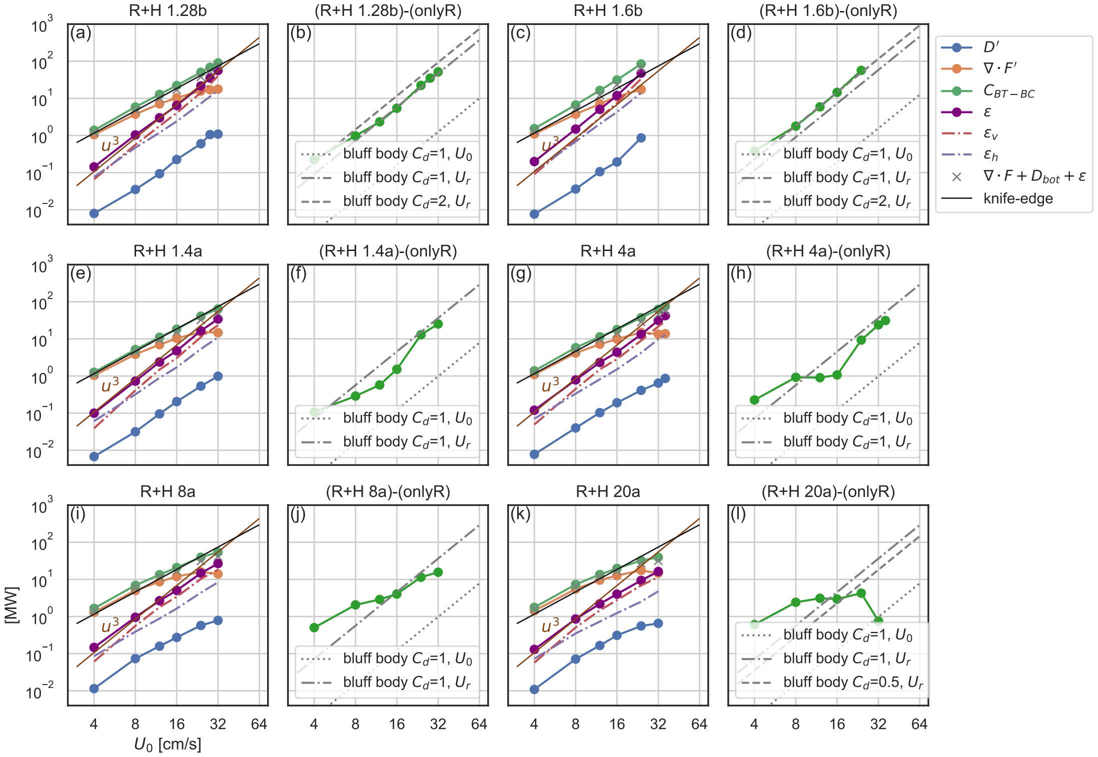

Figure 3.17: This figure is similar to Figure 15, except it examines the impact of varying headland cross-channel size (b) and along-channel size (a), with subfigures showing energy budget differences compared to the *only R* scenario. (a-d) correspond to increasing b, (e-h) to increasing a moderately, and (i-l) to highly streamlined headlands. The additional energy loss caused by the headland generally aligns well with bluff body predictions, except when the headland is highly streamlined ($a' > 8a$). For very sharp headlands ($b' = 1.6b$), the energy loss is better estimated with $C_d = 2$.

For sharper headlands (increasing b), the difference in conversion between the *only R* and R+H scenarios consistently follows a U_0^3 relationship and aligns well with the bluff body drag power estimated using the ridge-constricted velocity U_r and a drag coefficient $C_d = 1$ (Figure 3.17a-d). For the sharpest headland ($b' = 1.6b$), the best fit is achieved with $C_d = 2$, which is logical since sharper obstacles typically have higher drag coefficients. Conversely, for gentler headlands (increasing a, more streamlined), the relationship with U_0^3 gradually weakens (Figure 3.17e-k). In the extreme case of

$a' = 20a$, the conversion nearly reverts to the saturation level observed in the *only R* scenario (Figure 3.17k), where vortex generation is minimal or absent.

This scaling analysis provides valuable insights for sub-grid parameterization, particularly in coastal regions where complex three-dimensional topography, similar to that in our experiments, is common. We have demonstrated a method for using bluff body drag to estimate how much additional energy is lost by tides when a ridge is surrounded by a headland.

Moreover, even with varying headland geometries, the radiated energy remains unchanged for the same tidal forcing (orange curves in Figure 3.17). One possible explanation for this could be that, in our parameter space, the lee waves are generated in a relatively shallow, strongly forced environment, resulting predominantly in mode-1 internal tides, with only minor contributions from higher modes (e.g., modes 2-4). The stability and robustness of mode-1 may shield it from the increased turbulence caused by near-field vortices. However, in different environmental conditions where higher vertical modes dominate, the interaction with vortex-induced turbulence could have a more significant impact.

3.5 Summary

This study investigates the role of wake vortices in modulating tidal energy balance while internal tides co-generated. Using an experimental design combining an underwater sill and a headland, we reveal how wake vortices influence flow structure, energetics, and turbulence in shallow coastal environments.

The simultaneous presence of headland-driven vortices influences the structure of lee waves, stretching them horizontally in the channel's middle section and generating smaller lee waves near the headland. The tail end of the lee waves in the middle section was connected with the vertical confined strong flow vortices structure. Residual vortices from the earlier phase also impacted the upstream conditions, leading to the absence of approach-controlled flow characteristics when wake vortices were present.

Wake vortices form, persist, and dissipate within a single tidal cycle, following a consistent life cycle. At the start of the flood tide (or ebb tide), dipole vortices with opposite directions form near the northern and southern headlands. These vortices persist until the opposite tide (ebb or flood) generates its vortices. Over time, the negative vorticity vortex diminishes rapidly, while the remaining positive vortex lingers in deeper regions even after the next vortex cycle begins. After that, the residual vortex disappears when the new vortex grows into its position. The vortices exhibit tilting and exist within shear zones in the flow field, where they meet the criteria for shear instabilities, suggesting that these instabilities are responsible for generating interior turbulence in the vortices.

In addition to their dynamic evolution, vortex decay also contributes to vertical mixing, which is important for processes like phytoplankton growth and estuarine exchange. Compared to the *only R* case, the headland induces more mixing both downstream - by advecting the mixing region farther beyond the ridge - and upstream, where the water is lifted more strongly. This enhanced mixing primarily occurs before flow reversal, after which the buoyancy flux weakens.

Energetically, wake vortices cause tides to lose additional energy, most of which dissipates locally within the vortices' advection range. Importantly, internal tide radiation remains unaffected, with consistent energy radiated outward, likely due to the dominance of mode-1 internal tides. Estimating the energy loss caused by wake vortices is challenging; therefore, we applied multiple independent methods, including the power input to the 3D kinetic energy, the tidal power loss by form drag, and the barotropic-baroclinic conversion term. Remarkably, all three methods yielded consistent estimates of the tidal energy lost due to wake vortices, reinforcing the robustness of our approach.

Expanding the study to a broad parameter space ($Ro < 1$ to $Ro > 1$, $Kc < 1$ to $Kc > 1$, with $Fr \ll 1$) by varying tidal forcings and headland shapes confirms that the additional energy loss induced by headland vortices can be estimated using a simple bluff body law. However, the velocity (U) and cross-sectional area (A) must be carefully selected, ours with the velocity enhanced by the ridge-constricted flow and exposed-only headland cross-section area. This approach provides a method for quantifying tidal energy loss in coastal regions with complex topographies. Similar results were observed under various tidal forcing and headland geometries, where the internal tide radiation remained unaffected.

These results are particularly relevant in shallow coastal areas where internal tide generation is dominated by low-mode waves (mode-1 or mode-2, with U/c_1 approaching 1) and pure tidal forcing, as discussed in our previous study. Under such conditions, wake vortices and internal tides are co-generated with limited interactions, allowing for a clearer separation of their respective energy pathways. However, in the open ocean, such as around islands or seamounts, the presence of mean flows (Puthan et al., 2022b) and higher-mode internal tide generation could alter the dynamics. In these environments, internal tides are often dominated by higher modes (Klymak et al., 2008), which are more susceptible to near-field turbulence induced by vortices, potentially increasing interactions between the two phenomena. Future work should incorporate these factors to extend the applicability of our results to broader oceanic contexts.

In the open ocean, it has been observed that internal tides can propagate over distances of 2,000 to 3,000 kilometers with minimal energy loss (Ray and Mitchum, 1997). This phenomenon is attributed to the stability of low-mode internal tides, which are resistant to breaking. However, an outstanding question remains: where do these internal tides eventually break? One plausible hypothesis is that they break at the continental shelf or due to interactions with other topography, leading to mode conversion and subsequent breaking. In our motivated study site at Knight Inlet, a potential location for the breaking of propagating mode-1 waves could be the 90-degree bend in the inlet, where reflection or breaking may occur before they continue progressing toward the headland.

Another active area of research along the fate of low-mode internal tides is the interaction between incident internal waves and pre-existing vortices (Ito and Nakamura, 2023), which could be an important pathway in the oceanic energy cascade. These interactions, distinct from the co-generation dynamics discussed in this study, affect wave propagation, phase, and dissipation through mechanisms such as refraction (Chavanne et al., 2010), beam-like scattering (Dunphy and Lamb, 2014; Dunphy et al., 2017), and wave trapping or reflection (Pereira et al., 2007).

Chapter 4

Conclusion

4.1 Key Research Findings

Saturation of Internal Tide Generation

This study is the first to reveal the phenomenon of saturation in internal tide generation: when the barotropic tidal flow speed reaches a critical value where the barotropic velocity over the ridge equals the mode-1 phase speed ($Fr_c = \frac{U_c}{c_1} = 1$). The internal tide generation ceases to increase with the square of the tidal flow speed (U_0^2); instead, it exhibits saturation behavior. This discovery introduces a new parameter for describing the regime of flows generating internal tides. The $Fr_c \approx 1$ or $Fr_c > 1$ condition is more likely to occur in shallow water environments where the mode-1 phase speed is lower, and the tidal flow is stronger.

Internal Tide Generation at $Fr_c > 1$

Traditionally, two-layer models of internal tide generation in fjord suggest that internal tides are not generated when $Fr_c > 1$. However, this study finds that mode-1 internal tides can still be generated under such conditions, albeit at a saturated level. These tides continue to propagate outward, challenging the conventional understanding of internal tide generation in fjord-like regions and providing a revised framework for interpreting the phenomenon.

Additional Tidal Energy Loss Due to Wake Vortices

In topographic settings where wake vortices form in conjunction with internal tides, the tidal energy loss is unsurprisingly enhanced due to the presence of additional physical mechanisms. This study systematically demonstrates that this increased energy loss can be effectively estimated using the bluff body law, provided that flow speed and flow area parameters are carefully selected. To the best of our knowledge, this is the first study to comprehensively examine methods for estimating the additional tidal energy loss caused by wake vortices in such scenarios. Notably, the analysis yields reliable estimates when considering the ridge-constricted flow and the cross-sectional area above the ridge crest.

Energy Dissipation of Wake Vortices

The tidal energy fed to generate wake vortices dissipates rapidly within one tidal cycle, mostly within few kilometers from the generation region. This finding highlights the role of wake vortices as an important pathway for tidal energy dissipation and underscores their localized characteristics.

Energy Partition and Interaction Between Internal Tides and Wake Vortices

The study shows that the presence of wake vortices does not significantly alter the proportion of internal tide energy dissipation or the amount of energy propagating outward. The dissipation and propagation characteristics of internal tides remain stable regardless of whether wake vortices are present, suggesting weak interactions between the two mechanisms.

4.2 Research Contributions and Significance

Filling Research Gaps

This study advances the understanding of internal tide saturation in a strongly nonlinear flow regime ($Fr_c \approx 1$ and $10 > Nh/U > 1$), where analytical solutions have not been explored. The fact that internal tides are still generated and propagate into the far-field in the flow regime of $Fr_c > 1$ is groundbreaking, challenging traditional theories that predicted the absence of internal tide generation in such conditions. Additionally, through innovative experimental design, this study overcomes challenges in isolating the energy contributions of internal tides and wake vortices, systematically investigating their respective shares of tidal energy, the localized dissipation characteristics of wake vortices and stability of mode-1 internal tides. These findings deepen the understanding of tidal energy distribution and dissipation mechanisms in shallow coastal regions.

Practical Applications

The findings hold significant implications for improving parameterization of internal tides and wake vortices in ocean numerical models. This study's results enhance predictions of ocean energy distribution and mixing processes, providing a robust scientific basis for model development and a valuable reference framework for future research.

4.3 Research Limitations and Future Directions

In addition to the physical insights gained through this study, it is important to consider the sources of uncertainty associated with the modeling approach. These uncertainties, together with broader research limitations, arise primarily from the idealized model setup, parameter selection, and the exclusion of certain real-world physical processes. The following discussion outlines key factors that may influence the generalizability of the results and identifies areas for improvement in future studies.

Sources of Uncertainty and Research Limitations

This study employs idealized model setups, which may not fully capture the complexities of real-world ocean environments. For instance, it does not account for irregular topographic features (e.g., asymmetrical ridges or headlands) or other dynamic factors such as wind forcing or mean flows. As MacKinnon et al. (2019) suggests, a smaller mean flow than tides can lead to the downstream advection of wake vortices with both positive and negative vorticity. In that way, it would prevent them from dissipating near the generation region and potentially have more interactions with internal tides as they both radiate further downstream.

Additionally, the study's parameter choices (e.g., ridge height, slope, channel width, stratification strength, and Coriolis effects) may limit the generalizability of the findings. Specifically, one limitation of this study is that the height of the ridge was only tested at a single value in experiments involving wake vortices. This raises the question of whether changes in ridge height could alter the dynamics observed. Another potential limitation lies in the findings regarding internal tide radiation. While our results suggest that the size of the headland does not significantly affect internal tide radiation, the current setup features sharpest headlands with a cross-channel length that leaves approximately 46% of the channel width available for flow. If the cross-channel lengths of the north and south headlands were increased even more, further constricting the flow area, it is unclear whether the same internal tide radiation would persist. As the flow area decreases significantly with larger headlands, it is plausible that internal tide radiation might be adversely impacted, a scenario that warrants further investigation.

Future Research Directions

Inspired by the study area of Knight Inlet, this research lays the groundwork for future exploration of mode-1 internal tide dynamics. Key questions for future investigation include: When mode-1 internal tides propagate about 15 km from the generation region and experience a 90-degree bending, how much energy is reflected or dissipated? What proportion of energy continues toward the fjord head, and how much dissipates there? Does the energy dissipation balance the energy budget? These questions remain outstanding not only in enclosed basins like Knight Inlet but also in open ocean settings. Knight Inlet's enclosed nature offers an ideal environment for tracking internal tide dynamics and addressing these challenges.

Bibliography

Alford, M. H., MacKinnon, J. A., Nash, J. D., Simmons, H., Pickering, A., Klymak, J. M., Pinkel, R., Sun, O., Rainville, L., Musgrave, R., Beitzel, T., Fu, K.-H., and Lu, C.-W. (2011). Energy flux and dissipation in luzon strait: Two tales of two ridges. *J. Phys. Oceanogr.*, 41(11):2211–2222.

Alford, M. H., MacKinnon, J. A., Simmons, H. L., and Nash, J. D. (2016). Near-inertial internal gravity waves in the ocean. *Annual Review of Marine Science*, 8(1):95–123.

Alford, M. H., MacKinnon, J. A., Zhao, Z., Pinkel, R., Klymak, J., and Peacock, T. (2007). Internal waves across the pacific. *Geophysical Research Letters*, 34(24).

Alford, M. H., Peacock, T., MacKinnon, J. A., Nash, J. D., Buijsman, M. C., Centurioni, L. R., Chao, S.-Y., Chang, M.-H., Farmer, D. M., Fringer, O. B., Fu, K.-H., Gallacher, P. C., Graber, H. C., Helfrich, K. R., Jachec, S. M., Jackson, C. R., Klymak, J. M., Ko, D. S., Jan, S., Johnston, T. M. S., Legg, S., Lee, I.-H., Lien, R.-C., Mercier, M. J., Moum, J. N., Musgrave, R., Park, J.-H., Pickering, A. I., Pinkel, R., Rainville, L., Ramp, S. R., Rudnick, D. L., Sarkar, S., Scotti, A., Simmons, H. L., Laurent, L. C. S., Venayagamoorthy, S. K., Wang, Y.-H., Wang, J., Yang, Y. J., Paluszkiewicz, T., and Tang, T.-Y. D. (2015). The formation and fate of internal waves in the south china sea. *Nature*, 521(7550):65–69.

Arbic, B. K., Garner, S. T., Hallberg, R. W., and Simmons, H. L. (2004). The accuracy of surface elevations in forward global barotropic and baroclinic tide models. *Deep Sea Res. I*, 51(25–26):3069–3101.

Arbic, B. K. and Scott, R. B. (2008). On quadratic bottom drag, geostrophic turbulence, and oceanic mesoscale eddies. *J. Phys. Oceanogr.*, 38(1):84–103.

Armi, L. (1986). The hydraulics of two flowing layers with different densities. *J. Fluid Mech.*, 163:27–58.

Arneborg, L., Jansson, P., Staalstrøm, A., and Broström, G. (2017). Tidal energy loss, internal tide radiation, and local dissipation for two-layer tidal flow over a sill. *J. Phys. Oceanogr.*, 47(7):1521–1538.

Baines, P. (1995). Topographic effects in stratified flows. page 482.

Baines, P. G. and Hoinka, K. P. (1985). Stratified flow over two-dimensional topography in fluid of infinite depth: A laboratory simulation. *J. Atmos. Sci.*, 42(15):1614–1630.

Balmforth, N. J., Ierley, G. R., and Young, W. R. (2002). Tidal conversion by subcritical topography. *J. Phys. Oceanogr.*, 32(10):2900 –2914.

Bell, T. H. (1975). Lee waves in stratified flows with simple harmonic time dependence. *J. Fluid Mech.*, 67(4):705–722.

Billant, P. and Chomaz, J.-M. (2000). Theoretical analysis of the zigzag instability of a vertical columnar vortex pair in a strongly stratified fluid. *Journal of Fluid Mechanics*, 419:29–63.

Bindoff, N. L., Cheung, W. W., Kairo, J. G., Arístegui, J., Guinder, V. A., Hallberg, R., Hilmi, N. J. M., Jiao, N., Karim, M. S., Levin, L., O'Donoghue, S., Purca Cuicapusa, S. R., Rinkevich, B., Suga, T., Tagliabue, A., and Williamson, P. (2019). Changing ocean, marine ecosystems, and dependent communities. In *IPCC Special Report on the Ocean and Cryosphere in a Changing Climate*, pages 477–587. Intergovernmental Panel on Climate Change, Switzerland.

Black, K. P. and Gay, S. L. (1987). Eddy formation in unsteady flows. *J. Geophys. Res.*, 92(C9):9514–9522.

Blakely, C. P., Ling, G., Pringle, W. J., Contreras, M. T., Wirasaet, D., Westerink, J. J., Moghimi, S., Seroka, G., Shi, L., Myers, E., Owensby, M., and Massey, C. (2022). Dissipation and bathymetric sensitivities in an unstructured mesh global tidal model. *J. Geophys. Res.*, 127(5).

Bourgault, D. and Kelley, D. E. (2003). Wave-induced boundary mixing in a partially mixed estuary. *J. Mar. Res.*, 61(5):553–576.

Buijsman, M., Arbic, B., Green, J., Helber, R., Richman, J., Shriver, J., Timko, P., and Wallcraft, A. (2015). Optimizing internal wave drag in a forward barotropic model with semidiurnal tides. *Ocean Modell.*, 85:42–55.

Canals, M. and Pawlak, G. (2011). Three-dimensional vortex dynamics in oscillatory flow separation. *J. Fluid Mech.*, 674:408–432.

Canals, M., Pawlak, G., and MacCready, P. (2009). Tilted baroclinic tidal vortices. *Journal of Physical Oceanography*, 39(2):333–350.

Carter, G. S., Merrifield, M. A., Becker, J. M., Katsumata, K., Gregg, M. C., Luther, D. S., Levine, M. D., Boyd, T. J., and Firing, Y. L. (2008). Energetics of m2 barotropic-to-baroclinic tidal conversion at the hawaiian islands. *J. Phys. Oceanogr.*, 38(10):2205–2223.

Chang, M.-H., Jan, S., Liu, C.-L., Cheng, Y.-H., and Mensah, V. (2019). Observations of island wakes at high rossby numbers: Evolution of submesoscale vortices and free shear layers. *J. Phys. Oceanogr.*, 49(11):2997–3016.

Chang, M.-H., Tang, T. Y., Ho, C.-R., and Chao, S.-Y. (2013). Kuroshio-induced wake in the lee of green island off taiwan. *J. Geophys. Res.*, 118(3):1508–1519.

Chavanne, C., Flament, P., Luther, D., and Gurgel, K.-W. (2010). The surface expression of semidiurnal internal tides near a strong source at hawaii. part ii: Interactions with mesoscale currents*. *Journal of Physical Oceanography*, 40(6):1180â 1200.

Cummins, P. F. and Armi, L. (2010). Upstream internal jumps in stratified sill flow: Observations of formation, evolution, and release. *J. Phys. Oceanogr.*, 40(6):1419–1426.

Cummins, P. F., Armi, L., and Vagle, S. (2006). Upstream internal hydraulic jumps. *J. Phys. Oceanogr.*, 36(5):753–769.

Cummins, P. F., Vagle, S., Armi, L., and Farmer, D. M. (2003). Stratified flow over topography: upstream influence and generation of nonlinear internal waves. *Proc. Roy. Soc. London A*, 459(2034):1467–1487.

de Lavergne, C., Madec, G., Le Sommer, J., Nurser, A. J. G., and Naveira Garabato, A. C. (2016). On the consumption of antarctic bottom water in the abyssal ocean. *Journal of Physical Oceanography*, 46(2):635â 661.

Dewar, W. K., McWilliams, J. C., and Molemaker, M. J. (2015). Centrifugal instability and mixing in the california undercurrent. *Journal of Physical Oceanography*, 45(5):1224â 1241.

Dong, C., McWilliams, J. C., and Shchepetkin, A. F. (2007). Island wakes in deep water. *J. Phys. Oceanogr.*, 37(4):962–981.

Dunphy, M. and Lamb, K. G. (2014). Focusing and vertical mode scattering of the first mode internal tide by mesoscale eddy interaction. *Journal of Geophysical Research: Oceans*, 119(1):523â 536.

Dunphy, M., Ponte, A. L., Klein, P., and Gentil, S. L. (2017). Low-mode internal tide propagation in a turbulent eddy field. *J. Phys. Oceanogr.*, 47(3):649–665.

Durran, D. R. (1986). Another look at downslope windstorms. part i: The development of analogs to supercritical flow in an infinitely deep, continuously stratified fluid. *J. Atmos. Sci.*, 43(21):2527–2543.

Edwards, K. A., MacCready, P., Moum, J. N., Pawlak, G., Klymak, J. M., and Perlin, A. (2004). Form drag and mixing due to tidal flow past a sharp point. *J. Phys. Oceanogr.*, 34(6):1297–1312.

Egbert, G. D., Ray, R. D., and Bills, B. G. (2004). Numerical modeling of the global semidiurnal tide in the present day and in the last glacial maximum. *J. Geophys. Res.*, 109(C3).

Farmer, D., Alford, M., Lien, R.-C., Yang, Y. J., Chang, M.-H., and Li, Q. (2011). From luzon strait to dongsha plateau: Stages in the life of an internal wave. *Oceanography*, 24(4):64–77.

Farmer, D. and Armi, L. (1999a). The generation and trapping of solitary waves over topography. *Science*, 283(5399):188–190.

Farmer, D. and Armi, L. (1999b). Stratified flow over topography: the role of small-scale entrainment and mixing in flow establishment. *Proc. Roy. Soc. London A*, 455(1989):3221–3258.

Farmer, D., Pawlowicz, R., and Jiang, R. (2002). Tilting separation flows: a mechanism for intense vertical mixing in the coastal ocean. *Dyn. Atmos. Oceans*, 36(1-3):43–58.

Farmer, D. M. and Denton, R. A. (1985). Hydraulic control of flow over the sill in observatory inlet. *J. Geophys. Res.*, 90(C5):9051–9068.

Farmer, D. M. and Freeland, H. J. (1983). The physical oceanography of fjords. *Prog. Oceanogr.*, 12(2):147 – 219.

Farmer, D. M. and Smith, J. D. (1980a). Generation of lee waves over the sill in knight inlet. In *Fjord Oceanography*, pages 259–269. Springer US.

Farmer, D. M. and Smith, J. D. (1980b). Tidal interaction of stratified flow with a sill in knight inlet. *Deep Sea Res.*, 27(3):239–254.

Freeland, H. J. (1984). The partition of internal tidal motions in knight inlet, british columbia. *Atmosphere-Ocean*, 22(2):144–150.

Freeland, H. J. and Farmer, D. M. (1980). Circulation and energetics of a deep, strongly stratified inlet. *Can. J. Fish. Aquat. Sci.,*, 37(9):1398–1410.

Garrett, C. and Kunze, E. (2007). Internal tide generation in the deep ocean. *Ann. Rev. Fluid Mech.*, 39(1):57–87.

Garrett, C. and Munk, W. (1975). Space-time scales of internal waves; a progress report. *J. Geophys. Res.*, 80(3):291 –297.

Gerkema, T. and Zimmerman, J. (2008). An introduction to internal waves. *Lecture Notes, Royal NIOZ, Texel*, 207.

Geyer, W. R. (1993). Three-dimensional tidal flow around headlands. *Journal of Geophysical Research: Oceans*, 98(C1):955–966.

Geyer, W. R. and Signell, R. (1990). Measurements of tidal flow around a headland with a shipboard acoustic doppler current profiler. *J. Geophys. Res.*, 95(C3):3189.

Green, J. A. M. and Nycander, J. (2013). A comparison of tidal conversion parameterizations for tidal models. *J. Phys. Oceanogr.*, 43(1):104–119.

Griffiths, S. D. and Peltier, W. R. (2009). Modeling of polar ocean tides at the last glacial maximum: Amplification, sensitivity, and climatological implications. *J. Climate*, 22(11):2905–2924.

Gula, J., Molemaker, M. J., and McWilliams, J. C. (2016). Topographic generation of submesoscale centrifugal instability and energy dissipation. *Nat. Commun.*, 7(1).

Hamann, M. M., Alford, M. H., and Mickett, J. B. (2018). Generation and propagation of nonlinear internal waves in sheared currents over the washington continental shelf. *Journal of Geophysical Research: Oceans*, 123(4):2381–2400.

Hughes, K. G. and Klymak, J. M. (2019). Tidal Conversion and Dissipation at Steep Topography in a Channel Poleward of the Critical Latitude. *J. Phys. Oceanogr.*, 49(5):1269–1291.

Inall, M., Cottier, F., Griffiths, C., and Rippeth, T. (2004). Sill dynamics and energy transformation in a jet fjord. *Ocean Dyn.*, 54(3):307–314.

Inall, M., Rippeth, T., Griffiths, C., and Wiles, P. (2005). Evolution and distribution of tke production and dissipation within stratified flow over topography. *Geophys. Res. Lett.*, 32(8).

Inoue, R., Tsutsumi, E., and Nakamura, H. (2024). Numerical simulation of the kuroshio flowing over the hirase seamount in the tokara strait in autumn: Tidal vortex shedding in a baroclinic jet. *Journal of Physical Oceanography*, 54(1):153–172.

Ito, K. and Nakamura, T. (2023). Three regimes of internal gravity waveâ stable vortex interaction classified by a nondimensional parameter î´: Scattering, wheel-trapping, and spiral-trapping with vortex deformation. *Journal of Physical Oceanography*, 53(4):1087â 1106.

Jayne, S. R. and Laurent, L. C. S. (2001). Parameterizing tidal dissipation over rough topography. *Geophys. Res. Lett.*, 28(5):811–814.

Johnston, S., , MacKinnon, J., Colin, P., Haley, P., Lermusiaux, P., Lucas, A., Merrifield, M., Merrifield, S., Mirabito, C., Nash, J., Ou, C., Siegelman, M., Terrill, E., and Waterhouse, A. (2019). Energy and momentum lost to wake eddies and lee waves generated by the north equatorial current and tidal flows at peleliu, palau. *Oceanography*, 32(4):110–125.

Johnston, T. M. S. (2003). Internal tide scattering at seamounts, ridges, and islands. *J. Geophys. Res.*, 108(C6).

Johnston, T. M. S., Rudnick, D. L., and Kelly, S. M. (2015). Standing internal tides in the tasman sea observed by gliders. *J. Phys. Oceanogr.*, 45(11):2715–2737.

Kang, D. (2011). *Energetics and dynamics of internal tides in Monterey Bay using numerical simulations*. PhD thesis, Stanford University.

Kang, D. and Fringer, O. (2012). Energetics of barotropic and baroclinic tides in the monterey bay area. *J. Phys. Oceanogr.*, 42(2):272–290.

Kelly, S. M., Nash, J. D., and Kunze, E. (2010). Internal-tide energy over topography. *J. Geophys. Res.*, 115(C6).

Khatiwala, S. (2003). Generation of internal tides in an ocean of finite depth: analytical and numerical calculations. *Deep Sea Res. I*, 50(1):3–21.

Klymak, J., Legg, S., Alford, M., Buijsman, M., Pinkel, R., and Nash, J. (2012). The direct breaking of internal waves at steep topography. *Oceanography*, 25(2):150–159.

Klymak, J. M. (2018). Nonpropagating form drag and turbulence due to stratified flow over large-scale abyssal hill topography. *J. Phys. Oceanogr.*, 48(10):2383–2395.

Klymak, J. M., Alford, M. H., Pinkel, R., Lien, R.-C., Yang, Y. J., and Tang, T.-Y. (2011). The breaking and scattering of the internal tide on a continental slope. *J. Phys. Oceanogr.*, 41(5):926–945.

Klymak, J. M., Buijsman, M., Legg, S., and Pinkel, R. (2013). Parameterizing surface and internal tide scattering and breaking on supercritical topography: The one- and two-ridge cases. *J. Phys. Oceanogr.*, 43(7):1380–1397.

Klymak, J. M. and Gregg, M. C. (2001). Three-dimensional nature of flow near a sill. *J. Geophys. Res.*, 106(C10):22295–22311.

Klymak, J. M. and Gregg, M. C. (2003). The role of upstream waves and a downstream density pool in the growth of lee waves: Stratified flow over the knight inlet sill. *J. Phys. Oceanogr.*, 33(7):1446–1461.

Klymak, J. M. and Gregg, M. C. (2004). Tidally generated turbulence over the knight inlet sill. *J. Phys. Oceanogr.*, 34(5):1135–1151.

Klymak, J. M., Legg, S., and Pinkel, R. (2010a). A simple parameterization of turbulent tidal mixing near supercritical topography. *J. Phys. Oceanogr.*, 40(9):2059–2074.

Klymak, J. M. and Legg, S. M. (2010). A simple mixing scheme for models that resolve breaking internal waves. *Ocean Modell.*, 33(3-4):224–234.

Klymak, J. M., Legg, S. M., and Pinkel, R. (2010b). High-mode stationary waves in stratified flow over large obstacles. *J. Fluid Mech.*, 644:321–336.

Klymak, J. M. and Moum, J. N. (2003). Internal solitary waves of elevation advancing on a shoaling shelf. *Geophys. Res. Lett.*, 30(20).

Klymak, J. M., Moum, J. N., Nash, J. D., Kunze, E., Girton, J. B., Carter, G. S., Lee, C. M., Sanford, T. B., and Gregg, M. C. (2006). An estimate of tidal energy lost to turbulence at the hawaiian ridge. *J. Phys. Oceanogr.*, 36(6):1148–1164.

Klymak, J. M., Pinkel, R., and Rainville, L. (2008). Direct breaking of the internal tide near topography: Kaena ridge, hawaii. *J. Phys. Oceanogr.*, 38(2):380–399.

Klymak, J. M., Simmons, H. L., Braznikov, D., Kelly, S., MacKinnon, J. A., Alford, M. H., Pinkel, R., and Nash, J. D. (2016). Reflection of linear internal tides from realistic topography: The tasman continental slope. *J. Phys. Oceanogr.*, 46(11):3321–3337.

Kunze, E. (2017a). The internal-wave-driven meridional overturning circulation. *J. Phys. Oceanogr.*, 47(11):2673–2689.

Kunze, E. (2017b). Internal-wave-driven mixing: Global geography and budgets. *Journal of Physical Oceanography*, 47(6):1325â 1345.

Lamb, K. G. and Farmer, D. (2011). Instabilities in an internal solitary-like wave on the oregon shelf. *J. Phys. Oceanogr.*, 41(1):67–87.

Lawrence, G. A. (1993). The hydraulics of steady two-layer flow over a fixed obstacle. *J. Fluid Mech.*, 254:605–633.

Legg, S. (2014). Scattering of low-mode internal waves at finite isolated topography. *J. Phys. Oceanogr.*, 44(1):359–383.

Legg, S. (2021). Mixing by oceanic lee waves. *Ann. Rev. Fluid Mech.*, 53(1):173–201.

Legg, S. and Adcroft, A. (2003). Internal wave breaking at concave and convex continental slopes. *J. Phys. Oceanogr.*, 33(11):2224–2246.

Legg, S. and Klymak, J. (2008). Internal hydraulic jumps and overturning generated by tidal flow over a tall steep ridge. *J. Phys. Oceanogr.*, 38(9):1949–1964.

Li, Q. and Farmer, D. M. (2011). The generation and evolution of nonlinear internal waves in the deep basin of the south china sea. *J. Phys. Oceanogr.*, 41(7):1345–1363.

Llewellyn Smith, S. G. and Young, W. R. (2002). Conversion of the barotropic tide. *J. Phys. Oceanogr.*, 32(5):1554–1566.

Llewellyn Smith, S. G. and Young, W. R. (2003). Tidal conversion at a very steep ridge. *J. Fluid Mech.*, 495:175–191.

MacCready, P. and Pawlak, G. (2001). Stratified flow along a corrugated slope: Separation drag and wave drag. *J. Phys. Oceanogr.*, 31(10):2824–2839.

MacKinnon, J. A., Alford, M. H., Pinkel, R., Klymak, J., and Zhao, Z. (2013). The latitudinal dependence of shear and mixing in the pacific transiting the critical latitude for PSI. *J. Phys. Oceanogr.*, 43(1):3–16.

MacKinnon, J. A., Alford, M. H., Voet, G., Zeiden, K. L., Shaun Johnston, T. M., Siegelman, M., Merrifield, S., and Merrifield, M. (2019). Eddy wake generation from broadband currents near palau. *J. Geophys. Res.*, 124(7):4891–4903.

MacKinnon, J. A. and Gregg, M. C. (2003). Mixing on the late-summer new england shelf—solibores, shear, and stratification. *J. Phys. Oceanogr.*, 33(7):1476–1492.

MacKinnon, J. A., Zhao, Z., Whalen, C. B., Waterhouse, A. F., Trossman, D. S., Sun, O. M., Laurent, L. C. S., Simmons, H. L., Polzin, K., Pinkel, R., Pickering, A., Norton, N. J., Nash, J. D., Musgrave, R., Merchant, L. M., Melet, A. V., Mater, B., Legg, S., Large, W. G., Kunze, E., Klymak, J. M., Jochum, M., Jayne, S. R., Hallberg, R. W., Griffies, S. M., Diggs, S., Danabasoglu, G., Chassignet, E. P., Buijsman, M. C., Bryan, F. O., Briegleb, B. P., Barna, A., Arbic, B. K., Ansong, J. K., and Alford, M. H. (2017). Climate process team on internal wave–driven ocean mixing. *Bull. Am. Meteorol. Soc.*, 98(11):2429–2454.

Marsden, R. F. and Greenwood, K. C. (1994). Internal tides observed by an acoustic doppler current profiler. *J. Phys. Oceanogr.*, 24(6):1097–1109.

Marshall, J., Adcroft, A., Hill, C., Perelman, L., and Heisey, C. (1997). A finite-volume, incompressible navier stokes model for studies of the ocean on parallel computers. *J. Geophys. Res.*, 102(C3):5753–5766.

Mathur, M., Carter, G. S., and Peacock, T. (2014). Topographic scattering of the low-mode internal tide in the deep ocean. *J. Geophys. Res.*, 119(4):2165–2182.

McCabe, R. M., MacCready, P., and Pawlak, G. (2006). Form drag due to flow separation at a headland. *J. Phys. Oceanogr.*, 36(11):2136–2152.

Melet, A., Hallberg, R., Legg, S., and Nikurashin, M. (2014). Sensitivity of the ocean state to lee wave–driven mixing. *J. Phys. Oceanogr.*, 44(3):900–921.

Melet, A., Hallberg, R., Legg, S., and Polzin, K. (2013a). Sensitivity of the ocean state to the vertical distribution of internal-tide-driven mixing. *J. Phys. Oceanogr.*, 43(3):602–615.

Melet, A., Nikurashin, M., Muller, C., Falahat, S., Nycander, J., Timko, P. G., Arbic, B. K., and Goff, J. A. (2013b). Internal tide generation by abyssal hills using analytical theory. *J. Geophys. Res.*, 118(11):6303–6318.

Müller, P. and Liu, X. (2000). Scattering of internal waves at finite topography in two dimensions. part i: Theory and case studies. *J. Phys. Oceanogr.*, 30(3):532 – 549.

Müller, P. and Xu, N. (1992). Scattering of oceanic internal gravity waves off random bottom topography. *J. Phys. Oceanogr.*, 22(5):474 – 488.

Munk, W. and Wunsch, C. (1998). Abyssal recipes ii: energetics of tidal and wind mixing. *Deep Sea Res. I*, 45(12):1977–2010.

Murray, S. P., Hecht, A., and Babcock., A. (1984). On the mean flow in the tiran strait in winter. *J. Mar. Res.*, 42(2):265–287.

Musgrave, R. C., MacKinnon, J. A., Pinkel, R., Waterhouse, A. F., and Nash, J. (2016). Tidally driven processes leading to near-field turbulence in a channel at the crest of the mendocino escarpment. *J. Phys. Oceanogr.*, 46(4):1137–1155.

Musgrave, R. C., MacKinnon, J. A., Pinkel, R., Waterhouse, A. F., Nash, J., and Kelly, S. M. (2017). The influence of subinertial internal tides on near-topographic turbulence at the mendocino ridge: Observations and modeling. *J. Phys. Oceanogr.*, 47(8):2139–2154.

Nash, J. D., Kunze, E., Toole, J. M., and Schmitt, R. W. (2004). Internal tide reflection and turbulent mixing on the continental slope. *J. Phys. Oceanogr.*, 34(5):1117–1134.

New, A., Dyer, K., and Lewis, R. (1987). Internal waves and intense mixing periods in a partially stratified estuary. *Estuar. Coast. Shelf Sci.*, 24(1):15–33.

Nikurashin, M. and Ferrari, R. (2010). Radiation and dissipation of internal waves generated by geostrophic motions impinging on small-scale topography: Theory. *J. Phys. Oceanogr.*, 40(5):1055–1074.

Nikurashin, M., Ferrari, R., Grisouard, N., and Polzin, K. (2014). The impact of finite-amplitude bottom topography on internal wave generation in the southern ocean. *J. Phys. Oceanogr.*, 44(11):2938–2950.

Nikurashin, M. and Legg, S. (2011). A mechanism for local dissipation of internal tides generated at rough topography. *J. Phys. Oceanogr.*, 41(2):378–395.

Papoutsellis, C. E., Mercier, M. J., and Grisouard, N. (2023). Internal tide generation from non-uniform barotropic body forcing. *J. Fluid Mech.*, 964:A20.

Pawlak, G. and MacCready, P. (2002). Oscillatory flow across an irregular boundary. *Journal of Geophysical Research: Oceans*, 107(C5).

Pawlak, G., MacCready, P., Edwards, K. A., and McCabe, R. (2003a). Observations on the evolution of tidal vorticity at a stratified deep water headland. *Geophysical Research Letters*, 30(24).

Pawlak, G., MacCready, P., and McCabe, R. (2003b). Evolution of vortical flow structure in an ocean-boundary process. In *Near-Boundary Processes and their Parameterization. Proc.'Aha Huliko 'a Hawaiian Winter Workshop*, pages 131–142. Citeseer.

Pereira, A. F., Castro, B. M., Calado, L., and da Silveira, I. C. A. (2007). Numerical simulation of m2 internal tides in the south brazil bight and their interaction with the brazil current. *Journal of Geophysical Research: Oceans*, 112(C4).

Perfect, B., Kumar, N., and Riley, J. J. (2018). Vortex structures in the wake of an idealized seamount in rotating, stratified flow. *Geophys. Res. Lett.*, 45(17):9098–9105.

Perfect, B., Kumar, N., and Riley, J. J. (2020a). Energetics of seamount wakes. part i: Energy exchange. *J. Phys. Oceanogr.*, 50(5):1365–1382.

Perfect, B., Kumar, N., and Riley, J. J. (2020b). Energetics of seamount wakes. part II: Wave fluxes. *J. Phys. Oceanogr.*, 50(5):1383–1398.

Pickard, G. L. and Rodgers, K. (1959). Current measurements in knight inlet, british columbia. *Journal of the Fisheries Research Board of Canada*, 16(5):635–678.

Pingree, R. and Maddock, L. (1979). The tidal physics of headland flows and offshore tidal bank formation. *Marine Geology*, 32(3-4):269–289.

Pingree, R. D. and New, A. L. (1991). Abyssal penetration and bottom reflection of internal tidal energy in the bay of biscay. *J. Phys. Oceanogr.*, 21(1):28–39.

Provenzale, A. (1999). Transport by coherent barotropic vortices. *Ann. Rev. Fluid Mech.*, 31(1):55â 93.

Puthan, P., Jalali, M., Ortiz-Tarin, J. L., Chongsiripinyo, K., Pawlak, G., and Sarkar, S. (2020). The wake of a three-dimensional underwater obstacle: Effect of bottom boundary conditions. *Ocean Modell.*, 149:101611.

Puthan, P., Pawlak, G., and Sarkar, S. (2022a). High drag states in tidally modulated stratified wakes. *J. Phys. Oceanogr.*, 52(6):1033–1048.

Puthan, P., Pawlak, G., and Sarkar, S. (2022b). Wake vortices and dissipation in a tidally modulated flow past a three-dimensional topography. *J. Geophys. Res.*, 127(8).

Rainville, L. and Pinkel, R. (2006). Propagation of low-mode internal waves through the ocean. *J. Phys. Oceanogr.*, 36(6):1220–1236.

Ray, R. D. and Mitchum, G. T. (1997). Surface manifestation of internal tides in the deep ocean: observations from altimetry and island gauges. *Prog. Oceanogr.*, 40(1-4):135–162.

Robertson, R. (2011). Interactions between tides and other frequencies in the indonesian seas. *Ocean Dyn.*, 61(1):69–88.

Rubidge, E., Jeffery, S., Gregr, E., Gale, K., and Frid, A. (2020). *Assessment of nearshore features in the Northern Shelf Bioregion against criteria for determining Ecologically and Biologically Significant Areas (EBSAs).*

Sánchez-Garrido, J. C., Sannino, G., Liberti, L., García Lafuente, J., and Pratt, L. (2011). Numerical modeling of three-dimensional stratified tidal flow over camarinal sill, strait of gibraltar. *J. Geophys. Res.*, 116(C12).

Signell, R. P. and Geyer, W. R. (1991). Transient eddy formation around headlands. *J. Geophys. Res.*, 96(C2):2561–2575.

Simmons, H. L., Hallberg, R. W., and Arbic, B. K. (2004). Internal wave generation in a global baroclinic tide model. *Deep Sea Res. II*, 51(25-26):3043–3068.

Srinivasan, K., McWilliams, J. C., and Jagannathan, A. (2021). High vertical shear and dissipation in equatorial topographic wakes. *J. Phys. Oceanogr.*

Srinivasan, K., McWilliams, J. C., Molemaker, M. J., and Barkan, R. (2019). Submesoscale vortical wakes in the lee of topography. *J. Phys. Oceanogr.*, 49(7):1949–1971.

St. Laurent, L. and Garrett, C. (2002). The role of internal tides in mixing the deep ocean. *J. Phys. Oceanogr.*, 32(10):2882–2899.

St. Laurent, L., Stringer, S., Garrett, C., and Perrault-Joncas, D. (2003). The generation of internal tides at abrupt topography. *Deep Sea Res. I*, 50(8):987–1003.

St. Laurent, L. C. and Nash, J. D. (2004). An examination of the radiative and dissipative properties of deep ocean internal tides. *Deep Sea Research Part II: Topical Studies in Oceanography*, 51(25-26):3029–3042.

St. Laurent, L. C., Simmons, H. L., and Jayne, S. R. (2002). Estimating tidally driven mixing in the deep ocean. *Geophys. Res. Lett.*, 29(23):21–1–21–4.

Staalstrøm, A., Aas, E., and Liljebladh, B. (2012). Propagation and dissipation of internal tides in the oslofjord. *Ocean Sci.*, 8(4):525–543.

Staalstrøm, A., Arneborg, L., Liljebladh, B., and Broström, G. (2015). Observations of turbulence caused by a combination of tides and mean baroclinic flow over a fjord sill. *J. Phys. Oceanogr.*, 45(2):355–368.

Staalstrøm, A. and Røed, L. P. (2016). Vertical mixing and internal wave energy fluxes in a sill fjord. *J. Mar. Syst.*, 159:15–32.

Stacey, M. W. (1985). Some aspects of the internal tide in knight inlet, british columbia. *J. Phys. Oceanogr.*, 15(12):1652–1661.

Stacey, M. W. (2005). Review of the partition of tidal energy in five canadian fjords. *J. Coast. Res.*, 21(4 (214)):731–746.

Stacey, M. W. and Pond, S. (1992). A numerical model of the internal tide in Knight Inlet, British Columbia. *Atmos.-Ocean.*, 30(3):383–418.

Stammer, D., Ray, R. D., Andersen, O. B., Arbic, B. K., Bosch, W., Carrère, L., Cheng, Y., Chinn, D. S., Dushaw, B. D., Egbert, G. D., Erofeeva, S. Y., Fok, H. S., Green, J. A. M., Griffiths, S., King, M. A., Lapin, V., Lemoine, F. G., Luthcke, S. B., Lyard, F., Morison, J., Müller, M., Padman, L., Richman, J. G., Shriver, J. F., Shum, C. K., Taguchi, E., and Yi, Y. (2014). Accuracy assessment of global barotropic ocean tide models. *Reviews of Geophysics*, 52(3):243–282.

Stashchuk, N., Inall, M. E., and Vlasenko, V. (2007). Analysis of supercritical stratified tidal flow in a scottish fjord. *J. Phys. Oceanogr.*, 37:1793–1810.

Stashchuk, N. and Vlasenko, V. (2007). Numerical modelling of stratified tidal flow over a fjord sill. *Ocean Dyn.*, 57(4):325–338.

Stigebrandt, A. (1976). Vertical diffusion driven by internal waves in a sill fjord. *J. Phys. Oceanogr.*, 6(4):486–495.

Stigebrandt, A. (2012). Hydrodynamics and circulation of fjords. In Bengtsson, L., Herschy, R. W., and Fairbridge, R. W., editors, *Encyclopedia of Lakes and Reservoirs*, pages 327–344. Springer Netherlands, Dordrecht.

Stigebrandt, A. and Aure, J. (1989). Vertical mixing in basin waters of fjords. *J. Phys. Oceanogr.*, 19(7):917–926.

Sulzbach, R., Dobslaw, H., and Thomas, M. (2021). High-resolution numerical modeling of barotropic global ocean tides for satellite gravimetry. *J. Geophys. Res.*, 126(5).

Talley, L. (2013). Closure of the global overturning circulation through the indian, pacific, and southern oceans: Schematics and transports. *Oceanography*, 26(1):80–97.

Voet, G., Alford, M. H., MacKinnon, J. A., and Nash, J. D. (2020). Topographic form drag on tides and low-frequency flow: Observations of nonlinear lee waves over a tall submarine ridge near palau. *J. Phys. Oceanogr.*, 50(5):1489–1507.

Vouriot, C. V. M., Angeloudis, A., Kramer, S. C., and Piggott, M. D. (2018). Fate of large-scale vortices in idealized tidal lagoons. *Environ. Fluid Mech.*, 19(2):329–348.

Wang, D.-P. (2006). Tidally generated internal waves in partially mixed estuaries. *Cont. Shelf Res.*, 26(12–13):1469–1480.

Warner, S. J. and MacCready, P. (2014). The dynamics of pressure and form drag on a sloping headland: Internal waves versus eddies. *J. Geophys. Res.*, 119(3):1554–1571.

Warner, S. J., MacCready, P., Moum, J. N., and Nash, J. D. (2013). Measurement of tidal form drag using seafloor pressure sensors. *J. Phys. Oceanogr.*, 43(6):1150–1172.

Webb, A. J. and Pond, S. (1986). A modal decomposition of the internal tide in a deep, strongly stratified inlet: Knight inlet, british columbia. *J. Geophys. Res.*, 91(C8):9721–9738.

Wells, M. G. and van Heijst, G.-J. F. (2003). A model of tidal flushing of an estuary by dipole formation. *Dynamics of Atmospheres and Oceans*, 37(3):223–244.

Whalen, C. B., de Lavergne, C., Garabato, A. C. N., Klymak, J. M., MacKinnon, J. A., and Sheen, K. L. (2020). Internal wave-driven mixing: governing processes and consequences for climate. *Nature Reviews Earth & Environment*, 1(11):606–621.

Winters, K. B. and Armi, L. (2012). Hydraulic control of continuously stratified flow over an obstacle. *J. Fluid Mech.*, 700:502–513.

Winters, K. B. and Armi, L. (2013). The response of a continuously stratified fluid to an oscillating flow past an obstacle. *J. Fluid Mech.*, 727:83–118.

Wolanski, E., Asaeda, T., Tanaka, A., and Deleersnijder, E. (1996). Three-dimensional island wakes in the field, laboratory experiments and numerical models. *Continental Shelf Research*, 16(11):1437–1452.

Wolanski, E., Imberger, J., and Heron, M. L. (1984). Island wakes in shallow coastal waters. *J. Geophys. Res.*, 89(C6):10553–10569.

Wunsch, C. and Ferrari., R. (2004). Vertical mixing, energy, and the general circulation of the oceans. *Ann. Rev. Fluid Mech.*, 36(1):281–314.

Wynne-Cattanach, B. L., Alford, M. H., MacKinnon, J. A., and Voet, G. (2022). Measurements of turbulence generated by wake eddies near a steep headland. *J. Geophys. Res.*, 127(8).

Xing, J. and Davies, A. M. (2002). Processes influencing the non-linear interaction between inertial oscillations, near inertial internal waves and internal tides. *Geophys. Res. Lett.*, 29(5).

Zemskova, V. E. and Grisouard, N. (2021). Near-inertial dissipation due to stratified flow over abyssal topography. *J. Phys. Oceanogr.*

Zemskova, V. E., Musgrave, R. C., and Lerczak, J. A. (2024). Internal tides at the coast: energy flux of baroclinic tides propagating into the deep ocean in the presence of supercritical shelf topography. *J. Phys. Oceanogr.*